Inspiral, merger and ringdown of unequal mass black hole binaries: a multipolar analysis

Emanuele Berti*
McDonnell Center for the Space Sciences, Department of Physics, Washington University, Saint Louis, Missouri 63130, USA

Vitor Cardoso†
Department of Physics and Astronomy, The University of Mississippi, University, MS 38677-1848, USA ‡

José A. Gonzalez,§ Ulrich Sperhake,¶ Mark Hannam,** Sascha Husa,†† and Bernd Brügmann‡‡
Theoretical Physics Institute, University of Jena, Max-Wien-Platz 1, 07743, Jena, Germany
(Dated: March 9, 2007)

We study the inspiral, merger and ringdown of unequal mass black hole binaries by analyzing a catalogue of numerical simulations for seven different values of the mass ratio (from $q = M_2/M_1 = 1$ to $q = 4$). We compare numerical and Post-Newtonian results by projecting the waveforms onto spin-weighted spherical harmonics, characterized by angular indices $(l\,,m)$. We find that the Post-Newtonian equations predict remarkably well the relation between the wave amplitude and the orbital frequency for each $(l\,,m)$, and that the convergence of the Post-Newtonian series to the numerical results is non-monotonic. To leading order the total energy emitted in the merger phase scales like η^2 and the spin of the final black hole scales like η, where $\eta = q/(1+q)^2$ is the symmetric mass ratio. We study the multipolar distribution of the radiation, finding that odd-l multipoles are suppressed in the equal mass limit. Higher multipoles carry a larger fraction of the total energy as q increases. We introduce and compare three different definitions for the ringdown starting time. Applying linear estimation methods (the so-called Prony methods) to the ringdown phase, we find resolution-dependent time variations in the fitted parameters of the final black hole. By cross-correlating information from different multipoles we show that ringdown fits can be used to obtain precise estimates of the mass and spin of the final black hole, which are in remarkable agreement with energy and angular momentum balance calculations.

PACS numbers: 04.25.Dm, 04.25.Nx, 04.30.Db, 04.70.Bw

‡ Also at Centro de Física Computacional, Universidade de Coimbra, P-3004-516 Coimbra, Portugal
*Electronic address: berti@wugrav.wustl.edu
†Electronic address: vcardoso@phy.olemiss.edu
§Electronic address: jose.gonzalez@uni-jena.de
¶Electronic address: ulrich.sperhake@uni-jena.de
**Electronic address: mark.hannam@uni-jena.de
††Electronic address: sascha.husa@uni-jena.de
‡‡Electronic address: bernd.bruegmann@uni-jena.de

Contents

I. INTRODUCTION

More than thirty years after the first numerical simulations of binary black hole dynamics, the numerical relativity community is finally ready to compare binary black hole simulations with experimental data. Thanks to a series of recent breakthroughs, long term evolutions of inspiralling binary black holes that last for more than one orbit have been obtained with several independent codes, and accurate gravitational wave signals have been computed [1, 2, 3, 5, 6, 7, 8, 9, 10].

The use of numerical waveforms as templates for gravitational wave detection requires large-scale parameter studies, and correspondingly large computational resources. The main current technical problems in the field are the efficiency of the numerical simulations and the development of a "data analysis pipeline", connecting numerical simulations with analytical calculations of the early inspiral and late ringdown phases, and (eventually) with gravitational wave searches in actual detector data. To build a common language between the numerical relativity and data analysis communities we must develop a deeper understanding of the physical content of the simulations using analytical techniques, such as Post-Newtonian (PN) theory and black hole perturbation theory. A better analytical understanding of the simulations is important for many reasons:

(1) To determine which regions of the parameter space (mass, spin magnitude and inclination, orbital separation, eccentricity...) *must* be explored by numerical simulations, and which regions can be covered by (say) analytically-inspired interpolations of the numerical waveforms. This would obviously save a significant amount of computing time.

(2) To develop optimal strategies for the construction of detection templates, using a combination of numerical and analytical techniques.

(3) To understand details of the non-linear physics encoded in the strong-field merger gravitational waveforms, and extract as much science as possible from a detection.

In this paper we focus on point (3), and we try to develop a general framework to quantitatively compare analytical calculations of the inspiral and ringdown waveforms with the "full" waveforms produced by numerical simulations, extending from late inspiral through merger and ringdown.

Our work can be considered an extension of the recent analysis by Buonanno, Cook and Pretorius ([1], henceforth BCP). BCP studied simulations of non-spinning, equal mass black hole binaries starting out at three different initial separations. In this work we examine a larger set of simulations performed using the BAM code [2, 3] and the moving puncture method. We consider seven different mass ratios ($q \equiv M_2/M_1 \simeq 1$ to $q \simeq 4$ in steps of $\simeq 0.5$) with initial coordinate separation $D \simeq 7\,M$, roughly corresponding to ~ 2 orbits before merger. For each mass ratio, the simulations were carried out at three different resolutions. To explore the effect of initial separation on the physical parameters of the remnant, we also consider two runs at separation $D \simeq 8\,M$ (for $q = 2$ and $q = 3$), and one run at separation $D \simeq 10\,M$ (for $q = 1$). We typically use an extraction radius $r_{\rm ext} = 30M$, with the exception of the $q = 1$ run with $D \simeq 10\,M$, in which case we extract gravitational waves at $r_{\rm ext} = 30M,\ 40M$ and $50M$.

Section II contains details of our numerical setup. In Section II A we study in some detail a well-known issue with the extraction of gravitational waveforms from numerical simulations: the problem of fixing integration constants when we integrate the Weyl scalar Ψ_4 twice in time to obtain the gravitational wave amplitude h. Fixing the integration constants to zero produces a systematic drift in h and in its first time derivative. This drift is sometimes referred to in the literature as a "memory effect", but this is somewhat misleading. The so-called "memory effect" is really due to numerical errors, wrong initial conditions and limitations of wave extraction techniques, and it should *not* be confused with the Christodoulou memory, which is a true (if typically small) physical effect due to the non-linearity of general relativity [11]. We find that the extraction radius is critical to reduce the amplitude drift, and that resolution only seems to affect the drift for low-amplitude components of the wave.

In Section III we study the inspiral-merger transition. We start by projecting the 2.5PN gravitational wave amplitude for quasi-circular, non-spinning binaries [12, 13] onto spin-weighted spherical harmonics. In this way we obtain the spin-weighted spherical harmonic components of the Weyl scalar as PN series in the binary's orbital frequency: $\psi_{l\,,m} = \psi_{l\,,m}(M\Omega)$. We refer to this analytical expression of the gravitational wave amplitudes as the *Post-Newtonian Quasi-Circular* (PNQC) approximation (see Section III A for details, and Appendix A for a complete list of all the multipolar components).

The PNQC approximation can be used in two ways. First, given the orbital frequency evolution $\Omega(t)$, we can compute (an approximation to) the multipolar components $\psi_{l\,,m}$. Conversely, given the modulus of the wave amplitude $|\psi_{l\,,m}|(t)$, we can numerically invert the PN expansions to obtain a PNQC estimate of the orbital frequency: $\Omega \simeq \omega_{\rm PNQC}$. In Sections III B we compare $\omega_{\rm PNQC}$ with two alternative estimates of the orbital frequency, first introduced in BCP: ω_{Dm} (an estimate obtained from the gravitational wave frequency) and ω_c (computed from the punctures'

coordinate motion). Using these three different estimates of the orbital frequency, we study the convergence of the PNQC approximation. We find that, as in the point particle case [14], the convergence of the PN series is not monotonic. We also study the effect of resolution and wave extraction on the agreement between PNQC results and numerical results. We find that low resolution increases numerical noise in the frequencies and amplitudes at late times. A small extraction radius produces systematic errors at large separations, where gravitational wavelengths are longer, but it does not sensibly affect the ringdown phase.

In Section III C we study in detail the total radiated energy $E_{\rm tot}$ and the final angular momentum $j_{\rm fin}$ as functions of the mass ratio, providing fitting formulas for each of these quantities. We also compare the energy and angular momentum fluxes with their PNQC estimates, and we study (both analytically and numerically) the multipolar distribution of the radiation. To leading order, we find that $E_{\rm tot} \sim \eta^2$ and $j_{\rm fin} \sim \eta$, where $\eta \equiv q/(1+q)^2$ is the so-called symmetric mass ratio, and we provide fitting formulas for these quantities. As predicted by the PNQC approximation, odd-l multipoles of the radiation are suppressed in the equal mass limit. As the mass ratio increases, higher multipoles (with $l > 2$) carry a larger fraction of the total energy: for $q \gtrsim 2$, $l = 3$ typically carries $\sim 10\%$ of the total energy (see Table I below).

In Section IV we turn our attention to the merger-ringdown transition. During ringdown the waveform can be described as a superposition of complex exponentials, the quasinormal modes (QNMs). In [15] we argued that Prony methods (which are well-known in signal processing) are in many ways "optimal" methods to extract QNM frequencies from a numerical signal. After explaining our choice of the fitting window, in Section IV B we use Prony methods and standard, non-linear least-squares fits to look at the time dependence of the final black hole's parameters. We find resolution-dependent deviations in these parameters from the values predicted by linear black hole perturbation theory. These effects may be due to non-linearities and/or to rotational mode coupling, but at present we cannot exclude the possibility that they are, more trivially, an artifact of finite numerical resolution. In Section IV C we show that, by cross-correlating information from different multipolar components of the ringdown waves, we can find an empirical "best guess" for the optimal time to estimate the final black hole's mass and angular momentum. We argue that, because of the no-hair theorem, this best guess corresponds to the last time when the angular momenta (or masses) obtained by fitting the dominant multipoles agree with each other. In support of this argument, we also show that estimates of the mass and spin of the final black hole based on QNM fits are in remarkable agreement with wave extraction methods.

Black hole QNMs do not form a complete set, and for this reason it is not possible to define unambiguously the beginning of the ringdown phase. In Section IV D we consider three different definitions of the ringdown starting time, two of which have already appeared in the literature (but not in the context of binary black hole simulations). The first definition is based on looking for the time at which a QNM expansion provides the best fit to the actual numerical waveform, in the sense of a suitably defined norm [16]. Unfortunately, when applied to our numerical waveforms, this method is not particularly useful. The reason is that the norm is quite flat (and even worse, has some oscillations) over a wide range of starting times around the minimum. A second, more useful definition looks for the time maximizing the *energy content* of the QNM component of the waveform. For this reason, following Nollert [17], we call it the Energy Maximized Orthogonal Projection, or EMOP. We find that the "EMOP time" $t_{\rm EMOP}$ and the maximum fraction of energy carried by ringdown ($\simeq 42\%$) are remarkably independent of the mass ratio q. This is an indication that the ringdown waveform is in some sense "universal", in the sense that it does not depend too much on the details of the pre-merger phase. To our knowledge, the third definition of the ringdown starting time has not been introduced before. It uses a detection-based criterion, looking for the "effective energy" deposited in a matched filter.

In the conclusions we present a list of open problems and directions for future research.

To improve readability, some lengthy equations and technical material are presented in the Appendices.

Appendix A lists the spin-weighted spherical harmonic components of the Weyl scalar, up to and including 2.5PN terms in a PN expansion of the waveforms.

Appendix B provides fits for the energy, angular momentum and linear momentum radiated after the estimated time of formation of a common apparent horizon (CAH). Since the total energy radiated in a simulation depends on the initial separation of the binary, in this Appendix we also try to provide estimates for the energy, angular momentum and linear momentum radiated "after plunge". A problem here is that the Innermost Stable Circular Orbit (ISCO) is a controversial concept for comparable-mass binaries, and there is no unique way to define the beginning of the plunge phase. Given these intrinsic ambiguities, we estimate the starting time of the plunge, $t_{\rm ISCO}$, as the time when the orbital frequency Ω becomes larger than the ISCO frequency computed in PN theory (at 2PN or 3PN order, to bracket uncertainties). We also present a comparison of our results with PN estimates of the post-plunge radiation by Blanchet *et al.* [18].

Computational resources and resolution limitations reduce the accuracy of numerical simulations for large mass ratio. Unfortunately, many astrophysical black hole binaries could have $q = 10$ or larger (see eg. [19] and references therein). It is important to determine the maximum value of q that should be simulated in numerical relativity, or

equivalently, the smallest value of q for which black hole perturbation theory can be considered adequate for detection and/or parameter estimation. Appendix C collects some results from perturbation theory that may be useful in this context. We point out that, for large mass ratio, our numerical simulations seem to be in reasonable agreement with perturbative calculations of particles plunging with large angular momentum in a Schwarzschild black hole.

Finally, in Appendix D we introduce quantitative measures of the polarization state of the waveform. We show that the polarization of the wave (as viewed from the normal to the orbital plane) is circular for both inspiral and ringdown, with the exception of the unphysical portions of the wave: the initial data burst and the final, noise-dominated part of the ringdown waveform.

In all of this paper we adopt geometrical units ($c = G = 1$). Unless otherwise indicated, physical quantities are usually normalized to the total ADM mass of the system M.

TABLE I: Summary of the main results of this paper (see text). To convert from radiated momenta to kick velocities in km s^{-1}, the numbers in this Table must be multiplied by $c/10^4 \simeq 30$ km s^{-1}.

q	$j_{\rm fin}$	$j_{\rm QNM}$	$\frac{E_{\rm tot}}{M}$	$(\%l=2,3)$	$\frac{\Delta J_{\rm tot}}{M^2}$	$\frac{E_{\rm EMOP}}{M}$	$(\%l=2,3)$	$\frac{J_{\rm EMOP}}{M^2}$	$\frac{10^4 P_{\rm EMOP}}{M}$	$\frac{E_{\rm ISCO}}{M}$	$(\%l=2,3)$	$\frac{J_{\rm ISCO}}{M^2}$	$\frac{10^4 P_{\rm ISCO}}{M}$	$\frac{E_{\rm filter}}{M}$
1.0	0.689	0.684	0.0372	(96.3,0.4)	0.246	0.0185	(97.3,0.7)	0.0700	0	0.0266	(99.1,0.5)	0.1231	0	0.028
1.5	0.665	0.664	0.0340	(94.8,2.0)	0.229	0.0174	(91.9,2.1)	0.0676	2.32	0.0245	(97.1,2.4)	0.1165	2.05	0.026
2.0	0.626	0.626	0.0286	(91.8,4.6)	0.196	0.0142	(91.5,5.1)	0.0565	8.77	0.0208	(93.5,5.4)	0.0985	3.17	0.021
2.5	0.584	0.581	0.0238	(89.2,6.8)	0.167	0.0119	(92.4,7.6)	0.0480	9.42	0.0172	(91.1,8.0)	0.0850	3.68	0.018
3.0	0.543	0.544	0.0200	(86.8,8.7)	0.143	0.0103	(85.4,9.3)	0.0438	8.99	0.0146	(88.1,10.1)	0.0737	3.92	0.015
3.5	0.506	0.509	0.0170	(84.6,10.1)	0.124	0.0089	(84.2,9.6)	0.0387	8.29	0.0123	(86.2,11.8)	0.0645	3.88	0.012
4.0	0.474	0.478	0.0145	(83.2,11.3)	0.108	0.0078	(82.1,10.4)	0.0345	7.49	0.0106	(83.4,13.0)	0.0568	3.82	0.011

For reference, we find it useful to summarize some of our main results in Table I. There we list, for each mass ratio:

(1) the dimensionless angular momentum of the final black hole ($j = J/M^2$) as estimated from wave extraction methods ($j_{\rm fin}$) and from QNM fits ($j_{\rm QNM}$);

(2) the total energy and angular momentum radiated in each simulation ($E_{\rm tot}/M$, $J_{\rm tot}/M^2$);

(3) the energy, angular momentum and linear momentum radiated in ringdown, where the ringdown starting time is chosen according to the EMOP criterion ($E_{\rm EMOP}/M$, $J_{\rm EMOP}/M^2$, $P_{\rm EMOP}/M$);

(4) the energy, angular momentum and linear momentum radiated after plunge, where the plunge is defined by the location of the 3PN ISCO ($E_{\rm ISCO}/M$, $J_{\rm ISCO}/M^2$, $P_{\rm ISCO}/M$);

(5) the effective fraction of energy detected by a ringdown filter ($E_{\rm filter}/M$).

The Table also shows the fraction of energy being radiated in the two dominant multipoles ($l = 2,\ 3$).

II. NUMERICAL SETUP

The sequence of numerical simulations of unequal mass black-hole binaries studied in this work has been obtained with the BAM code [2] using the moving puncture method [5, 6]. Specifically, we study here a subset of the sequence used in Ref. [3] to determine the maximum recoil resulting from the inspiral of non-spinning black hole binaries. The BAM code has been described extensively in Ref. [2] and further details of the numerical simulations of the unequal mass binaries are given in Ref. [3]. Here we summarize the model parameters relevant for our present study.

A sequence of quasi-circular initial data of non-spinning black-hole binaries is determined by the initial coordinate separation D, the mass ratio q of the black holes, and the initial momenta P_i of each black hole. Approximate values of P_i appropriate for quasi-circular orbits were calculated using the 3PN-accurate expression given in Section VII of Ref. [2]. For most of the models we consider in this work, the initial coordinate separation is $D \simeq 7\,M$ (denoted by "D7"), where M is the Arnowitt-Deser-Misner (ADM) mass. The mass ratio is varied from $q \simeq 1.0$ to $q \simeq 4.0$ in steps of approximately 0.5. In order to assess the impact of larger initial separations on our results, we also construct models with larger initial separation: $D \simeq 10\,M$ for $q \simeq 1.0$, and $D \simeq 8\,M$ for $q \simeq 2.0$ and $q \simeq 3.0$. We will denote these models by D10 and D8, respectively. The complete set of models is summarized in Table II.

TABLE II: Summary of the main physical parameters for the series of simulations studied in this work. q denotes the mass ratio, D is the initial coordinate separation, and J the ADM angular momentum. We also list the simulation time at which the orbital frequency equals the orbital frequency at the 3PN Innermost Stable Circular Orbit or ISCO, $t^{\rm 3PN}_{\rm ISCO}$; an estimate of the time at which a CAH forms, $t_{\rm CAH}$; the time at which the energy flux has a maximum, $t_{\rm flux}$; and the time at which the modulus of the $l = m = 2$ mode has a peak, $t_{\rm peak}$. All quantities are normalized to the ADM mass M. The final column lists the number N of orbits until the estimated time of formation of the CAH.

q	D/M	J/M^2	$t^{\rm 3PN}_{\rm ISCO}/M$	$t_{\rm CAH}/M$	$t_{\rm flux}/M$	$t_{\rm peak}/M$	N
1.00	7.046	0.8845	211.9	215.0	231.8	234.0	1.94
1.49	7.044	0.8494	213.5	218.2	234.3	236.4	1.96
1.99	7.040	0.7870	211.6	217.5	233.6	235.4	1.93
2.48	7.036	0.7232	213.2	221.0	236.2	238.1	1.96
2.97	7.034	0.6649	213.2	223.2	237.8	239.8	1.98
3.46	7.030	0.6132	215.0	226.8	240.6	242.5	2.02
3.95	7.028	0.5679	216.7	230.5	243.0	244.8	2.06
1.00	10.104	0.9826	972.7	973.7	992.3	994.5	5.93
1.99	8.086	0.8214	438.0	443.9	459.2	461.6	3.44
2.97	8.038	0.6865	392.2	402.9	414.5	418.1	3.23

All models have been evolved in time using a resolution of $M_1/22.5$ near the punctures. The models starting from an initial separation $D = 7\,M$ have also been evolved using resolutions of $M_1/25.5$ and $M_1/29$. In the remainder of this work we will refer to these resolutions as low (LR), medium (MR) and high resolution (HR). Gravitational waves have been extracted in the form of the Newman-Penrose scalar Ψ_4. Unless specified otherwise, we use an extraction radius $r = 30\,M$. We decompose the resulting Ψ_4 into modes by projection onto spherical harmonics of spin-weight $s = -2$ (see Ref. [2] for conventions) according to

$$Mr\Psi_4 = Mr \sum_{l=2}^{\infty} \sum_{m=-l}^{l} {}_{-2}Y_{lm}(\theta\,,\phi)\,\psi_{l\,,m}\,. \tag{2.1}$$

In Fig. 1 we show examples of the resulting modes by plotting $|{\rm Re}(Mr\,\psi_{lm})|$, the modulus of the real part of the waveforms. Except for the spurious initial wave burst (visible up to about $t = 50\,M$) and for the final, noisy signal following the ringdown phase, the imaginary part of $\psi_{l\,,m}$ is related to the real part by a phase shift of $\pi/2$ (see Appendix D for a more detailed discussion of the polarization of the waveforms). The figures demonstrate that the $l = 2$, $|m| = 2$ modes dominate the gravitational wave emission in all simulations. Contributions due to higher order modes become increasingly significant, though, as the mass ratio is increased. In all of our models we find the strongest contributions of higher-l modes to result from $m = \pm l$. We further note the suppression of odd-l modes in the equal mass limit. For this reason, in the left panel of Fig. 1 we only show modes with $l = 2,\ 4$.

In Fig. 2 we plot the modulus $|Mr\,\psi_{lm}|$ of the amplitude of some of the dominant multipoles. Two features of this plot are worth stressing: (i) the $l = m = 4$ mode does not have a single, clear damping time in the ringdown phase (this is particularly evident for $q = 2.0$); (ii) the amplitude modulation visible in the inspiral phase is induced by some eccentricity in the initial data. This eccentricity seems to decrease during the evolution, but estimates of the eccentricity damping are beyond the scope of this paper.

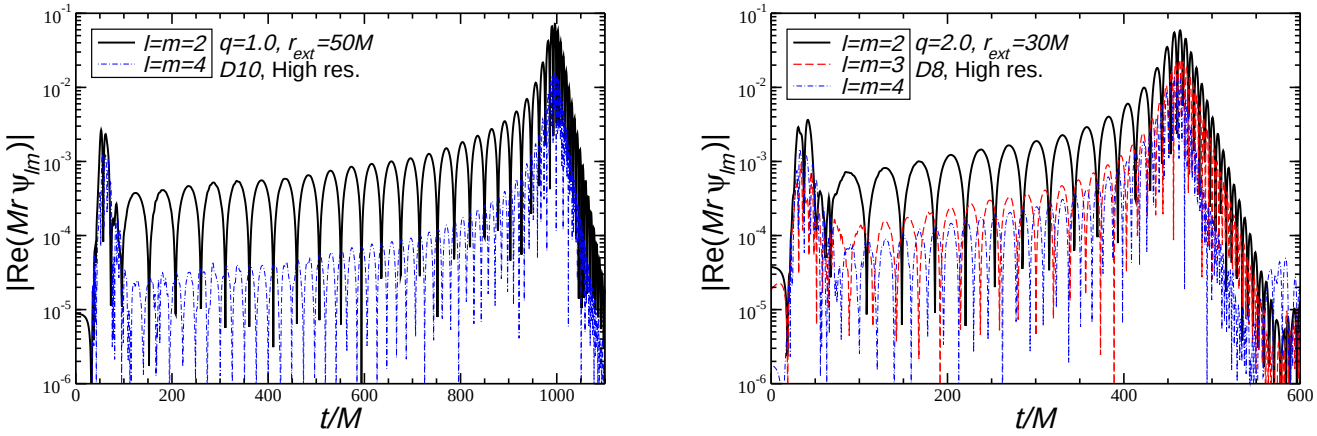

FIG. 1: $|\mathrm{Re}(Mr\,\psi_{lm})|$ for $q = 1.0$ (left) and $q = 2.0$ (right). For the equal mass ($q = 1.0$) binary the $l = m = 3$ component is strongly suppressed, and we do not show it.

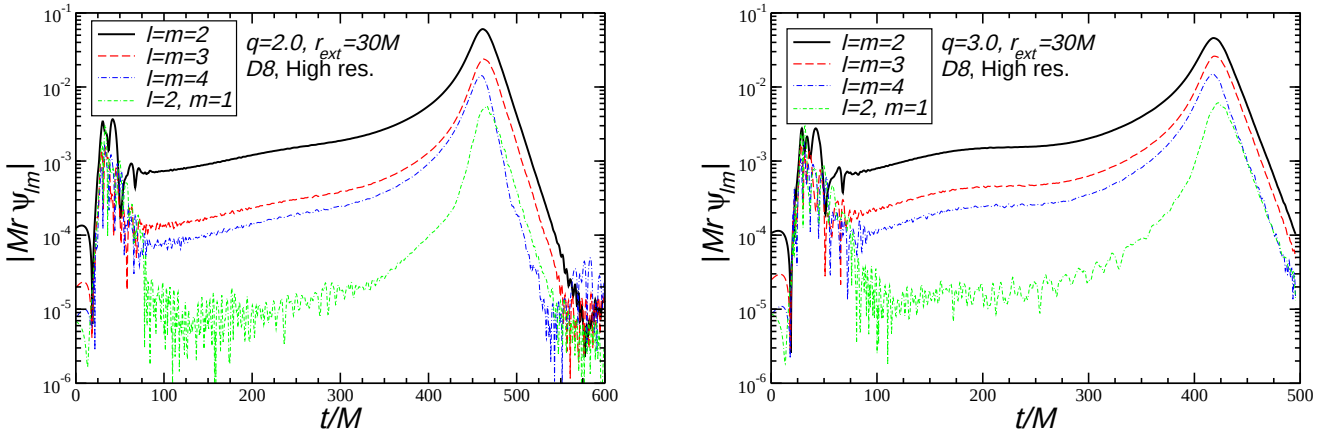

FIG. 2: $|Mr\,\psi_{lm}|$ for different mass ratios. Each plot shows only some of the dominant components: $l = m = 2,\ 3,\ 4$ and $(l = 2,\ m = 1)$. The initial burst of radiation is induced by the initial data, and the wiggles at late times are due to numerical noise.

The late-time, exponentially decaying portion of the waveforms is the ringdown phase. As the wave amplitude decreases, numerical noise gradually starts dominating the signal. In order to exclude this noisy part from the fitting of damped sinusoids in the modelling of the ringdown part, discussed in Section IV below, we introduce a cutoff time beyond which we no longer use the waveforms. The practical criterion to choose this late-time cutoff will be discussed in more detail in Section IV.

For part of our analysis, we find it helpful to have estimates of the merger time of the black-hole binary. The most reliable estimate would be the formation of a CAH. In order to reduce the computational cost, however, all simulations have been performed without using an apparent horizon finder, so that we need to rely on alternative estimates. In the case of equal masses, we follow Ref. [5] and use the lapse function α to estimate the black hole merger time as the time when the $\alpha = 0.3$ regions around each hole merge. Unfortunately, this criterion does not generalize straightforwardly to unequal mass binaries. For these cases, we instead locate the time when the ratio of

the radial and tangential speeds of the punctures is equal to 0.3, which corresponds roughly to the time when the black holes reach the "light ring" in the effective-one-body model [20]. This is discussed further in Section III below.

A. Memory effects in subdominant multipoles

The effect of a gravitational wave on a gravitational wave detector in the far field of the source is best described in terms of the transverse-tracefree part of the metric. The two polarization states, h_+ and $h_\times$, of the gravitational wave are related to the curvature, expressed in terms of the complex Newman-Penrose scalar Ψ_4, by

$$\Psi_4 = \ddot{h}_+ - i\ddot{h}_\times \,. \tag{2.2}$$

Here $h_+(t-z) = h^{TT}_{xx} = -h^{TT}_{yy}$, $h_\times(t-z) = h^{TT}_{xy} = h^{TT}_{yx}$ for a wave propagating in the z-direction. Note that different conventions (typically for the Newman-Penrose scalar) are used in the literature, correspondingly leading to different relations with h_+ and $h_\times$. Ref. [21], for example, has a factor 2 in their Eq. (5.3).

Given the Newman-Penrose scalar Ψ_4 for a particular mode, we thus have to integrate twice in time to obtain h_+ and $h_\times$ and, in consequence, fix two constants of integration, which correspond to the values and time derivatives of h_+ and $h_\times$ at the initial time as functions on the (celestial) sphere. Integrations in time over Ψ_4 are also required to compute the radiated energy, linear and angular momentum from the radiation content:

$$\frac{dE}{dt} = \lim_{r\to\infty}\left[\frac{r^2}{16\pi}\int_\Omega \left|\int_{-\infty}^{t}\Psi_4 d\tilde{t}\right|^2 d\Omega\right], \tag{2.3}$$

$$\frac{dP_i}{dt} = -\lim_{r\to\infty}\left[\frac{r^2}{16\pi}\int_\Omega \ell_i\left|\int_{-\infty}^{t}\Psi_4 d\tilde{t}\right|^2 d\Omega\right], \tag{2.4}$$

$$\frac{dJ_z}{dt} = -\lim_{r\to\infty}\left\{\frac{r^2}{16\pi}\mathrm{Re}\left[\int_\Omega\left(\partial_\phi\int_{-\infty}^{t}\Psi_4 d\tilde{t}\right)\left(\int_{-\infty}^{t}\int_{-\infty}^{\hat{t}}\overline{\Psi_4}d\tilde{t}d\hat{t}\right)d\Omega\right]\right\}, \tag{2.5}$$

where

$$\ell_i = (-\sin\theta\cos\phi,\ -\sin\theta\sin\phi,\ -\cos\theta)\,. \tag{2.6}$$

The definitions above are based on time integrals which start in the infinite past (at retarded time $t=-\infty$), and thus capture the complete gravitational wave signal. Starting the time integrations at $t=-\infty$ corresponds to the limit of infinite extraction radius on the initial time slice — the slice would then extend all the way to spatial infinity, no part of the waveform would be lost, and it would take an infinite time for the waves to reach the extraction sphere. With our current setup of the numerical codes this situation cannot be handled, and we work with finite extraction radii. The constants of integration would then correspond to the signal that has been lost. In order to accurately compute from the Newman-Penrose scalar the radiated energy and momenta and the gravitational wave strain required by data analysts, it is thus necessary to understand the influence of these constants of integration, and ideally, how to choose them correctly[1].

Naively setting the constants to zero typically leads to a non-zero value and slope of h_+ and $h_\times$ after the passage of the wave. This effect will in general have contributions from the signal that has been lost due to a finite extraction radius, from numerical error, and from the inherent ambiguities of the extraction procedure at finite radius. Furthermore, a time independent gravitational wave *memory* effect is also possible and has been described in the literature [11, 13]. Apart from the effect due to an improper setting of the constants of integration, the other effects will accumulate over time, which may allow some discrimination.

A time dependent h_+ or $h_\times$ after the passage of the waves implies continued geodesic deviation for an assembly of test-particles and a continued flux of energy. A time independent strain would correspond to the effect of a gravitational wave *memory*, which has been described in the literature [11, 13] (see also [23]). While the time independent phenomenon is physically expected (although it should be small), the time-dependent drift phenomenon appears to be counter-intuitive and we expect h_+ and $h_\times$ to settle down into a stationary state at late times. All unphysical effects in the non-zero value and slope of h_+ and $h_\times$ after the passage of the wave should converge away

[1] Koppitz *et al.* recently argued that the choice of integration constants may be important for an accurate calculation of the recoil velocity of the final black hole [22].

with resolution and increasing extraction radius. A rigorous convergence test could attempt to identify a remaining physical gravitational wave memory effect (indepent of time after the passing of the wave). Consistency with the physical situation requires that the slope of h_+ and $h_\times$ after the passage of the wave converge away with resolution and increasing extraction radius.

TABLE III: Average slope of the $l = 2$, $m = 2$ component of h_+ for $q = 1$ and run D10, obtained from linear regression.

q	run	$h_{\rm punc}$	$r_{\rm ex}$	$10^5 a_1^+$	$r_{\rm ex}^4 a_1^+$	$10^5 a_1^\times$	$r_{\rm ex}^2 a_1^\times$
1.0	D10	high	30	7.11	57.6	3.67	0.033
1.0	D10	high	40	2.24	57.3	2.37	0.038
1.0	D10	high	50	0.91	56.9	1.42	0.036
1.0	D10	med	30	7.12	57.7	3.67	0.033
1.0	D10	med	40	2.27	58.1	2.38	0.038
1.0	D10	med	50	0.94	58.8	1.42	0.036
1.0	D10	low	30	7.09	57.4	3.68	0.033
1.0	D10	low	40	2.26	57.9	2.38	0.038
1.0	D10	low	50	0.94	58.8	1.42	0.036
2.0	D8	low	20	1.35	2.16	5.57	0.022
2.0	D8	low	25	0.56	2.19	4.57	0.029
2.0	D8	low	30	0.27	2.19	3.20	0.029
3.0	D8	low	20	0.86	1.38	3.33	0.013
3.0	D8	low	25	0.36	1.41	2.83	0.018
3.0	D8	low	30	0.17	1.38	2.00	0.018

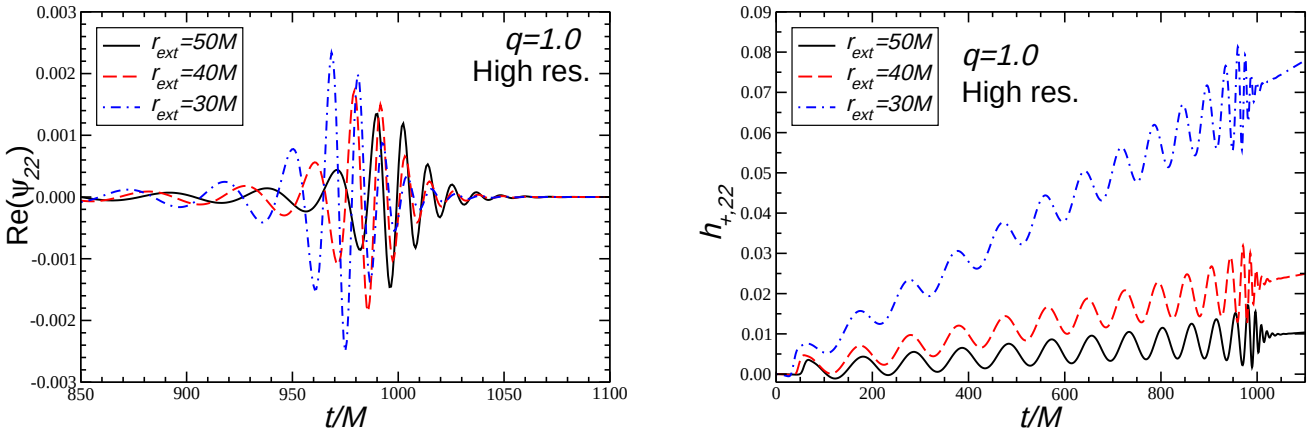

FIG. 3: Effect of changing the extraction radius on the "memory effect" when we do not apply corrections to the integration constants. These plots refer to the dominant multipole ($l = m = 2$) of run D10 with $q = 1.0$.

We study this effect in more detail by considering the D10 run with $q = 1.0$. In Fig. 3 we plot the resulting $l = 2$, $m = 2$ contribution for h_+ obtained at different extraction radii. The figure demonstrates two important features of this memory effect. First, the linear growth starts right at the beginning of the simulation, indicating that the memory effect is indeed essentially due to a non-vanishing constant of integration, or that possibly it is accumulated already in the early stages of the wave pulse (including the artificial burst of radiation). Second, the slope decreases significantly if we use larger extraction radii.

We next apply a least-squares fit of a linear function $f(t) = a_0 + a_1 t$ to h_+ and $h_\times$ resulting from the simulations of models $q = 1.0$, D10; $q = 2.0$, D8; and $q = 3.0$, D8. The resulting slopes are labelled as a_1^+ and $a_1^\times$ respectively in Table III. The table demonstrates in the case of the model with $q = 1.0$, D10 that the coefficients are essentially independent of the grid resolution. Columns 5 to 7 of the table indicate, however, that their dependence on the extraction radius can be rather well approximated by power laws: $a_1^+ \sim r_{\rm ex}^{-4}$, and $a_1^\times \sim r_{\rm ex}^{-2}$. This discrepancy between the + and $\times$

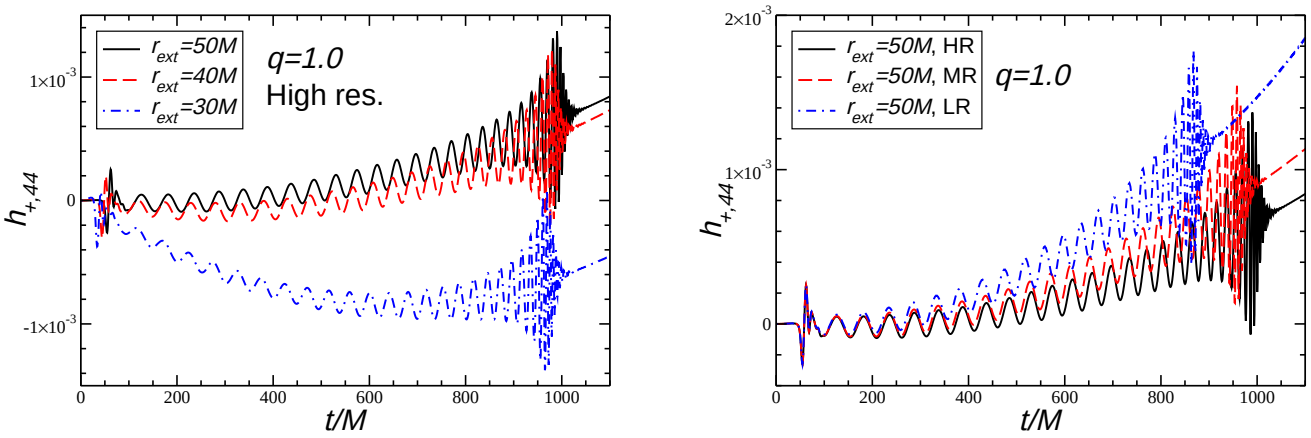

FIG. 4: Effect of changing the extraction radius on the "memory effect" when we do not apply corrections to the integration constants. These plots refer to a small amplitude mode ($l = m = 4$) of run D10 with $q = 1.0$. The left panel shows the effect of changing the extraction radius at fixed resolution. In the right panel, we change the resolution at fixed extraction radius.

polarization modes is rather surprising, because the circular polarization of the waves implies that they differ merely by a phase shift of $\pi/2$. The key observation in this context is that this simple relation between h_+ and $h_\times$ applies to the inspiral waveform but *not* to the spurious initial wave burst. This is explicitly shown in Appendix D. We thus conclude that the slope is a consequence of the omitted early wave signal (the constant of integration) or the initial wave burst. We emphasize, however, that the decreasing impact of the initial data pulse at larger radii is not due to it being dissipated away by numerical viscosity, which would have manifested itself in a resolution dependence of the slope.

The picture is somewhat more complicated in the case of the $l = 4$, $m = 4$ mode plotted in Fig. 4, where we do not only see a significant dependence of the memory effect on resolution, but also a non-linear trend of h_+, suggesting contributions from the ambiguities of wave extraction or numerical error. Consistent with the issue being due to the ambiguities of the wave extraction algorithm, we observe a significant decrease in the memory effect at larger extraction radius. In contrast to the $l = 2$, $m = 2$ case, we did not find a simple systematic dependence of the coefficients on extraction radius and resolution.

We conclude this Section with a discussion of alternative choices for the integration constants. For each polarization and each mode in the spectral decompositions we work with (to take care of the angular dependence of these constants of integration) we can fix the integration constants by demanding that the time derivative of $h_{+/\times}$ vanishes at late times. This can be achieved by matching to a ringdown signal, or more heuristically by subtracting the time average or time dependent polynomials, such as those obtained by the fitting processes mentioned above. The second constant of integration, which may have a contribution from a *physical* memory effect, is typically very small, and can be set to zero for many practical purposes if the wave extraction radius is not too small. From our observations, we conclude that using a sufficiently large extraction radius is certainly a highly recommended way of reducing spurious memory effects.

III. THE INSPIRAL-MERGER TRANSITION

The parameters chosen in Section II for the initial data do not give perfect quasi-circular (non-eccentric) orbits. This problem has been discussed in various papers [1, 10, 24, 25]. A simple way to visualize the residual eccentricity of the binary's orbit is to compare the punctures' motion with predictions for circular, Newtonian orbits. At leading order, the quadrupole formula predicts that the orbital radius should evolve according to [26]:

$$v_r = \dot{r} = -\frac{64}{5}\frac{\eta M^3}{r^3}\,, \tag{3.1}$$

where $\eta = M_1 M_2/M^2 = q/(1+q)^2$ is the symmetric mass ratio. From the relation between the orbital radius r and the (Keplerian) orbital frequency Ω, $M = \Omega^2 r^3$, we get the ratio of radial and tangential velocities in unequal mass, circular orbit binaries:

$$\frac{v_r}{v_t} = \left(\frac{\dot{r}}{\Omega r}\right) = -\frac{64}{5}\eta (M\Omega)^{5/3}\,. \tag{3.2}$$

This formula is of course a rough approximation, being based on the quadrupole formula and assuming a Keplerian orbit [1]. In Fig. 5 we show the ratio of radial and tangential velocities v_r/v_t obtained from the punctures' motion and from the Newtonian quadrupole prediction. Curves labeled "Newtonian" are obtained by replacing the punctures' orbital frequency $\Omega = \omega_c$ (see Section III B 1 below for details of the definition) in Eq. (3.2). Curves obtained from the actual puncture orbital motion clearly oscillate around the Newtonian circular value, mainly because of the non-zero orbital eccentricity. A similar effect was observed in Fig. 6 of BCP.

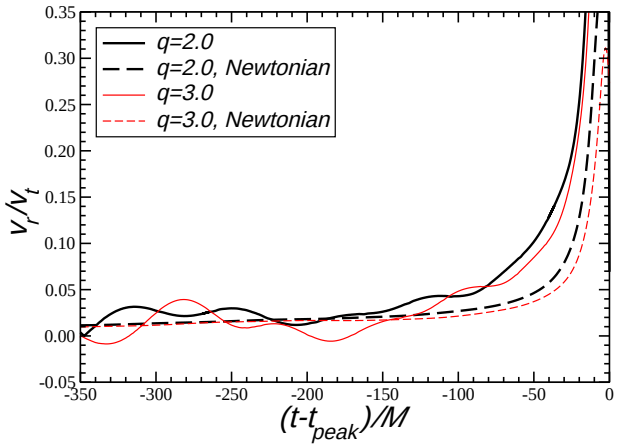

FIG. 5: Ratio of radial and tangential velocities for D8 runs and for two values of the mass ratio ($q = 2.0$ and $q = 3.0$).

At early times in the evolution, say $(t - t_{\rm peak}) \lesssim -100M$, the ratio $|v_r/v_t| \lesssim 0.05$, and the orbit is (to a reasonably good approximation) quasi-circular. At later times v_r/v_t grows, as the motion turns from inspiral to plunge. Given the computational cost of implementing an apparent horizon finder during the evolution, we use the following rough criterion to locate the formation of the apparent horizon. In the effective-one-body model [20], the ratio between radial and tangential velocities is $v_r/v_t \sim 0.3$ (so that the motion is strongly "plunging") at the light ring $r = 3M$. Since the light ring should be close to the location where a CAH forms, we simply *define* the time of formation of a CAH $t_{\rm CAH}$ as the point where the ratio v_r/v_t, as computed from the punctures' orbital motion, becomes larger than 0.3 (see also the related discussion around Table II). Fig. 5 shows that v_r/v_t rises very steeply in this region, so we expect the error introduced by our rough approximation to be at most of order a few M.

A. The Post-Newtonian quasi-circular approximation for the inspiral phase

In this work we will perform extensive comparisons of numerical waveforms with the PN approximation. For this purpose it is useful to decompose the Weyl scalar Ψ_4 in spin-weighted spherical harmonic components according

to Eq. (2.1). The $\psi_{l\,,m}$'s can be obtained by taking two time derivatives of the PN gravitational waveforms $h_{+\,,\times}$ according to Eq. (2.2), and then computing

$$Mr\,\psi_{l\,,m} = Mr\int d\Omega\,{}_{-2}Y^{*}_{l\,,m}(\theta\,,\phi)\Psi_4 \equiv Mr\int d\Omega\,{}_{-2}Y^{*}_{l\,,m}(\theta\,,\phi)\left(\ddot{h}_+ - i\ddot{h}_\times\right)\,. \tag{3.3}$$

The azimuthal dependence of the PN waveforms has the functional form $\phi - \left(\int \Omega dt - 2M\Omega\ln\Omega/\Omega_0\right)$ [12]. Thus, the expansion of the *waveform* $h \equiv h_+ - ih_\times$ in spin-weighted spherical harmonics has an explicit time dependence of the form $\exp[-im(\int \Omega dt - 2M\Omega\ln\Omega/\Omega_0)]$. For instance, using the same convention on spin-weighted spherical harmonics as in Ref. [2], we get the following result for the $l = m = 2$ component of the waveform:

$$\begin{aligned} Mr\,(h_+ - ih_\times)_{2\,,2} &= 8\sqrt{\frac{\pi}{5}}\eta(M\Omega)^{2/3}\left[1 + \frac{55\eta - 107}{42}(M\Omega)^{2/3} + 2\pi(M\Omega) - \frac{2173 + 7483\eta - 2047\eta^2}{1512}(M\Omega)^{4/3}\right. \\ &+ \left.\left(\frac{-107 + 34\eta}{21}\pi + \frac{56}{5}i\eta\right)(M\Omega)^{5/3}\right]e^{-im(\int \Omega dt - 2M\Omega\ln\Omega/\Omega_0)}\,. \end{aligned} \tag{3.4}$$

Here Ω_0 is an arbitrary constant [12] and the orbital angular velocity Ω is a time dependent quantity, the 3.5PN expansion of which can be found (for example) in [27].

As stated earlier, to compute the projection of Ψ_4 onto spin-weighted spherical harmonics we must take the second time derivative of expressions like Eq. (3.4) above. Noticing that the logarithmic term in the phase is of 4PN order [12], we will simply neglect it when performing the derivative[2]. One can then show that, up to 2.5PN order,

$$\psi_{l\,,m} = -m^2\Omega^2(h_+ - ih_\times)_{l\,,m}\,, \tag{3.5}$$

the only exception to this rule being the 2.5PN contribution to the amplitude of the $l = m = 2$ component.

In our calculation of the amplitudes we discard terms of order $\mathcal{O}(M\Omega)^{14/3}$ (i.e. we compute all terms in a 2.5PN expansion of the gravitational wave amplitude, as given in [13]). We only list the positive-m components of the dominant multipoles, since negative-m components are obtained by using the symmetry property

$$\psi_{l\,,-m} = (-1)^l\psi^{*}_{l\,,m}\,. \tag{3.6}$$

The small mass ratio limit of these results was obtained by Poisson and by Tagoshi and Sasaki [28]. For comparable mass ratios, we find that the amplitudes of the dominant components are:

$$\begin{aligned} Mr\,\psi_{2\,,2}e^{i\tilde{\phi}} &= 32\sqrt{\frac{\pi}{5}}\eta(M\Omega)^{8/3}\left[1 + \frac{55\eta - 107}{42}(M\Omega)^{2/3} + 2\pi(M\Omega) - \frac{2173 + 7483\eta - 2047\eta^2}{1512}(M\Omega)^{4/3}\right. \\ &+ \left.\left(\frac{-107 + 34\eta}{21}\pi + \frac{168}{5}i\eta\right)(M\Omega)^{5/3}\right]\,, \end{aligned} \tag{3.7a}$$

$$\begin{aligned} Mr\,\psi_{3\,,3}e^{i\tilde{\phi}} &= -27\sqrt{\frac{6\pi}{7}}\eta\frac{\delta M}{M}(M\Omega)^3\left[1 - (4 - 2\eta)(M\Omega)^{2/3} + \left[3\pi + i\left(\frac{21}{5} - 6\ln(3/2)\right)\right]M\Omega\right. \\ &+ \left.\left(\frac{123}{110} - \frac{1838}{165}\eta + \frac{887}{330}\eta^2\right)(M\Omega)^{4/3}\right]\,, \end{aligned} \tag{3.7b}$$

$$\begin{aligned} Mr\,\psi_{4\,,4}e^{i\tilde{\phi}} &= \frac{1024}{9}\sqrt{\frac{\pi}{7}}\eta(M\Omega)^{10/3}\left\{(1 - 3\eta) - \frac{1779 - 6365\eta + 2625\eta^2}{330}(M\Omega)^{2/3}\right. \\ &+ \left.\left[4\pi + i\left(\frac{42}{5} - 8\ln(2)\right) - \eta\left(12\pi + i\left(\frac{1193}{40} - 24\ln(2)\right)\right)\right](M\Omega)\right\}\,, \end{aligned} \tag{3.7c}$$

$$\begin{aligned} Mr\,\psi_{2\,,1}e^{i\tilde{\phi}} &= -\frac{8}{3}\sqrt{\frac{\pi}{5}}\eta\frac{\delta M}{M}(M\Omega)^3\left[1 + \frac{20\eta - 17}{28}(M\Omega)^{2/3} + \frac{2\pi + i(1 + \ln 16)}{2}M\Omega\right. \\ &+ \left.\left(-\frac{43}{126} - \frac{509}{126}\eta + \frac{79}{168}\eta^2\right)(M\Omega)^{4/3}\right]\,, \end{aligned} \tag{3.7d}$$

[2] This is consistent with the PN order considered here. While it would be preferable to keep the logarithmic term, it introduces an extra unknown constant which we chose not to worry about in the present work.

where η is the symmetric mass ratio and we defined the phase $\tilde{\phi}$ as

$$e^{i\tilde{\phi}} \equiv e^{im(\int \Omega dt - 2M\Omega \ln \Omega/\Omega_0)} \,. \tag{3.8}$$

The complete expressions of all multipolar components are listed, for reference, in Appendix A. The leading order term in (3.7a) is nothing but the quadrupole approximation: see eg. Eq. (24) of BCP. As predictable from symmetry arguments the odd-m multipoles, being proportional to $\delta M/M$, are suppressed in the equal mass case. To recover the spin-weighted expansion of the waveform $h_+ - ih_\times$ one only has to divide these expressions by $-m^2\Omega^2$. The only exception to this rule is the 2.5PN term of the $l = m = 2$ component: the $168i\eta/5$ term in ψ changes to $56i\eta/5$ when computing the waveform, see Eq. (3.4) above.

Terms with $l > 2$ and higher-order PN corrections provide a strong consistency check on both the PN expansion and the numerical results. First, they tell us if the PN approximation is a good approximation for higher multipolar components of the radiation ($l > 2$). Secondly, they can be used to check convergence of the PN expansion for any $(l\,,m)$. If the series is convergent, for example, going beyond the so-called "restricted PN approximation" (i.e., including higher powers of $(M\Omega)^{1/3}$ in the expansion for $\psi_{2\,,2}$) should yield better agreement with the amplitude predicted by numerical simulations.

Notice also that multipoles which are *formally* of higher PN order are not necessarily subdominant. For instance, $\psi_{2\,,1}$ is of order $(M\Omega)^3$. Based on power counting, this term should be comparable to $\psi_{3\,,3}$ and larger than $\psi_{4\,,4}$. However the amplitude of these terms is proportional to $(8/3)\sqrt{\pi/5} \simeq 2.11$ for $(l = 2,\ m = 1)$, $27\sqrt{6\pi/7} \simeq 44.31$ for $(l = 3,\ m = 3)$ and $(1024/9)\sqrt{\pi/7} \simeq 76.22$ for $(l = 4,\ m = 4)$, respectively. At the maximum orbital frequency we are interested in (the ISCO frequency, which is of order $M\Omega = M\Omega_{\rm ISCO} \simeq 0.1$), the $(2\,,1)$ amplitude is much smaller than the $(4\,,4)$ amplitude: $\psi_{2\,,1} \simeq 0.06\,(\delta M/M)\,\psi_{4\,,4}$. For this reason, in the following we will limit consideration to terms with $l = m = 2,\ 3,\ 4$. Figure 2 shows that the dominance of these terms is quantitatively confirmed by numerical simulations of the inspiral-merger transition.

B. Estimates of the binary's orbital frequency from numerical simulations

In the following of this paper we estimate the orbital frequency Ω of a binary at any given time by three different methods, that we list below.

(1) *Orbital frequency from the gravitational wave frequency:* $\Omega \simeq \omega_{Dm}$

This estimate of Ω is based on the observation that the gravitational wave frequency in a mode characterized by azimuthal number m is $\omega_{\rm GW} = m\Omega$. In practice, the calculation can be carried out in two equivalent ways:

(i) Decompose each mode into a real amplitude and a real phase, $\psi_{l\,,m} = \mathcal{A}_{l\,,m}\exp(i\phi_{l\,,m})$. Then compute:

$$\omega_{Dm} = \frac{1}{m}\frac{d\phi_{l\,,m}}{dt} \,. \tag{3.9}$$

(ii) Alternatively, observe that if some frequency dominates the Fourier expansion of a signal, this frequency can be estimated by computing

$$\omega_{Dm} = -\frac{1}{m}{\rm Im}\left[\frac{\dot{\psi}_{l\,,m}}{\psi_{l\,,m}}\right] \,. \tag{3.10}$$

The latter method was used also in BCP, and it relies on the (implicit) assumption that the modulus of the complex mode amplitudes $\psi_{l\,,m}$ changes slowly compared with their phase. However, we verified that methods (i) and (ii) yield results which are basically indistinguishable from each other. In the following, when we refer to ω_{Dm} we always compute Eq. (3.10) by finite differencing. In any case, we verified for all modes that using Eq. (3.9) would not produce appreciable differences.

(2) *Orbital frequency from the coordinate orbital motion of the punctures:* $\Omega \simeq \omega_c$

The idea here is to convert each puncture's motion in the $(x\,,y)$ plane into polar coordinates $(r\,,\phi)$, then compute $\frac{d\phi}{dt}$. There are two problems with this estimate of the orbital frequency. The first is that this definition obviously depends on the choice of coordinates, and we expect it to get worse as we get closer to merger. In our particular set of coordinates, the puncture motion agrees better with other estimates of the orbital frequency for large mass

ratio, when the system becomes more similar to a test particle moving in Schwarzschild. The second problem is that, to compare the puncture coordinate frequencies against the other two, we need to take into account the finite time it takes for the waves to reach the extraction sphere. We simply estimate this propagation time to be $\Delta t \simeq r_{\rm ext}$, but since the propagation speed may differ from unity and waves are not emitted from the origin, this introduces a (small) additional uncertainty in the comparison.

(3) *Orbital frequency from the Post-Newtonian Quasi-Circular approximation:* $\Omega \simeq \omega_{\rm PNQC}$

BCP made the remarkable observation that, even very close to merger, the $l = |m| = 2$ modes of the inspiral waveform can be well approximated by the standard quadrupole formula for a Newtonian binary in circular orbit. They computed the leading-order term in Eq. (3.7a):

$$M r \psi_{2\,,\pm 2} = 32\sqrt{\frac{\pi}{5}}\eta (M\Omega)^{8/3} e^{\mp 2i(\phi(t)-\phi_0)}\,, \tag{3.11}$$

where $\phi(t)$ is the accumulated phase of the orbit, which (ignoring logarithmic terms) is

$$\phi(t) = \int_0^t \Omega(t')\, dt'\,, \tag{3.12}$$

and pointed out that this simple *Newtonian Quasi-Circular* (NQC) approximation can be used in two ways. First, given the orbital frequency evolution $\Omega(t)$ we can compute (an approximation to) the wave amplitude. Conversely, given the modulus of the wave amplitude, we can estimate the orbital frequency $\Omega = \omega_{\rm NQC}$ by inverting the modulus of Eq. (3.11), and check whether $\omega_{\rm NQC}$ agrees with the estimates ω_{Dm} (computed from the gravitational wave frequency) and ω_c (computed from the punctures' coordinate motion).

We will show below that using Eqs. (3.7a)–(3.7d) and, more generally, the expression listed in Appendix A, their observation can be extended to all multipolar components of the radiation. Our approximation improves on the simple NQC estimate in that we include all PN terms in the expansion up to 2.5PN, but it still assumes that the orbits are quasi-circular. For this reason, we call it a *Post-Newtonian Quasi-Circular* (PNQC) estimate of the frequency.

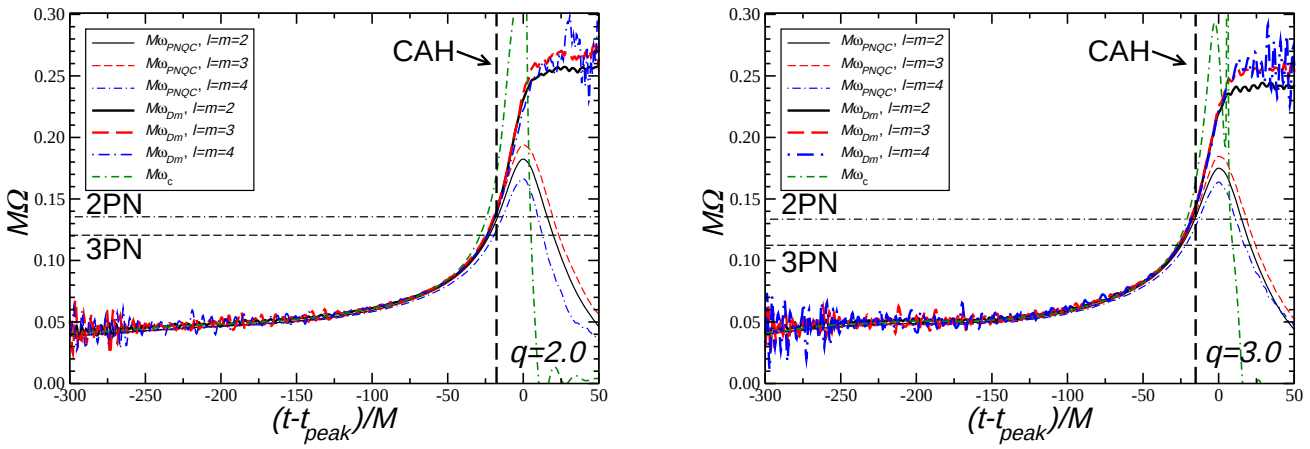

FIG. 6: Orbital frequencies from the puncture motion ($\Omega = \omega_c$), from the gravitational wave frequency ($\Omega = \omega_{Dm}$) and from the PNQC approximation ($\Omega = \omega_{\rm PNQC}$). Here $\omega_{\rm PNQC}$ is computed by inverting Eqs. (3.7a), (3.7b) and (3.7c), and keeping only the leading order. Times are measured starting from $t_{\rm peak}$, the peak of the $l = m = 2$ mode amplitude for the given mass ratio (see Table II). Horizontal lines mark 2PN and 3PN estimates of the ISCO frequency (as listed in Tables X and XI); the vertical dashed line marks (an estimate of) the CAH formation. The plots refer to runs D8 and two different mass ratios ($q = 2.0$ on the left, and $q = 3.0$ on the right).

The three different estimates are shown in Fig. 6, to be compared with Fig. 7 in BCP. For this plot we choose run D8 (since the inspiral part lasts longer) and we compare two values of the mass ratio: $q = 2.0$ and $q = 3.0$.

After the final black hole's formation (roughly, for $t > t_{\rm CAH}$) the system is no longer a binary, and therefore different estimates of the orbital frequency disagree with each other. The most physically meaningful quantity after merger is the gravitational wave frequency ω_{Dm}. This frequency levels off to a constant, which is roughly proportional to the fundamental $l = m$ quasinormal frequency of the final black hole (see Section IV for a detailed analysis of the merger-ringdown transition).

The puncture coordinate frequency ω_c is a reliable estimate at early times and large separations, whereas ω_{Dm} is initially noisy, being contaminated by spurious initial data radiation or noise from boundary reflections. However, the puncture coordinates provide a bad estimate of the orbital frequency already $\sim 30M$ before the peak of the radiation. In this sense, when we are close to merger our coordinates are not as good as the generalized harmonic coordinates used in BCP. Coordinate choices having such a big impact, some care is required if we want to attach physical meaning to quantities like ω_c. For example, BCP use the "decoupling point" where ω_c separates from ω_{Dm} to mark the beginning of the merger phase. With our particular choice of coordinates this decoupling point would occur much earlier, clearly invalidating the estimate. We argue that comparing ω_{Dm} and (our best PN guess for) $\omega_{\rm PNQC}$ should provide a coordinate-independent, more reliable estimate of the decoupling point.

In Fig. 6 the PNQC frequency $\omega_{\rm PNQC}$ is computed by inverting Eqs. (3.7) and keeping only the leading order. This simple leading-order approximation is in excellent agreement with the other estimates (ω_c and ω_{Dm}) until $\sim 20M$ before the radiation peak. At this point the orbit transitions from inspiral to plunge, and we cannot expect the PN inspiral calculation to provide the correct orbital frequency anymore.

We expect the transition from inspiral to plunge to happen, roughly, when the binary's orbital frequency crosses the ISCO frequency. To estimate the ISCO we look for extrema of the 2PN and 3PN Taylor expansions of the binding energy (see Appendix B for numerical values of $\Omega_{\rm ISCO}$, and Section IIIA of Ref. [29] for a discussion of this and alternative methods of estimating the ISCO). The corresponding estimates are marked by horizontal lines in Fig. 6. Around the transition region, $\omega_{\rm PNQC}$ (which is computed *assuming* that the motion is a slow, quasi-circular inspiral) should deviate more and more from ω_c and ω_{Dm}.

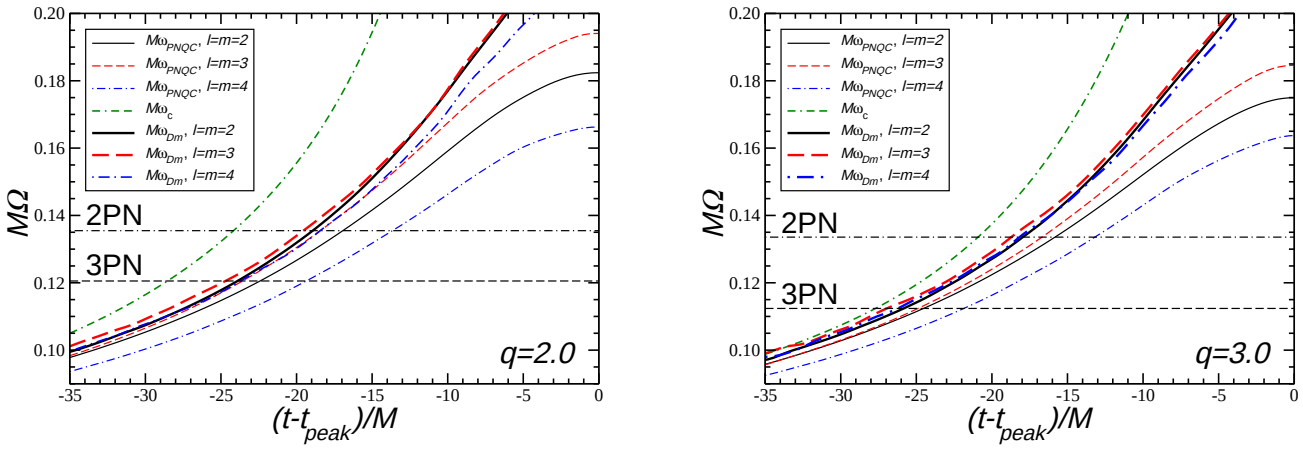

FIG. 7: Orbital frequencies from the puncture motion ($\Omega = \omega_c$), from the gravitational wave frequency ($\Omega = \omega_{Dm}$) and from the PNQC approximation ($\Omega = \omega_{\rm PNQC}$) in the region around the ISCO. Here $\omega_{\rm PNQC}$ is computed inverting Eqs. (3.7a), (3.7b) and (3.7c), and keeping only the leading order.

This statement is made more quantitative in Fig. 7, where we zoom in around the ISCO region. Thick lines (the actual gravitational wave frequencies of the system in a multipole with $l = m$, divided by m) and thin lines (the PNQC estimates) are almost parallel to each other before the ISCO, and they deviate significantly as the orbit crosses the ISCO. The pre-ISCO agreement is better, and the post-ISCO deviation larger, for the $q = 3.0$ binary than for the $q = 2.0$ binary. This is in agreement with the physical expectation that, as the binary's masses become comparable, the very notion of an ISCO becomes less and less significant: roughly speaking, the system cannot be described anymore by the simple-minded picture of a "small" particle orbiting a larger black hole.

An interesting question is if the agreement between the PNQC frequency $\omega_{\rm PNQC}$ and other estimates of the orbital frequency, namely ω_c and ω_{Dm}, improves if we include additional terms in Eqs. (3.7). In other words, can we use different estimates of the PNQC orbital frequency $\omega_{\rm PNQC}$ to estimate the convergence rate of the PN approximation?

Conversely, if we substitute ω_{Dm} into Eqs. (3.7) to compute some PN approximation to the amplitude, does the agreement with the modulus of the numerical amplitude $|Mr\,\psi_{l\,,m}|$ get better as we increase the PN order? We address these issues below.

1. *Convergence of the Post-Newtonian quasi-circular approximation*

In Fig. 8 we show a simple "visual" convergence test of the PN approximation. We substitute ω_{Dm} into Eqs. (3.7a) and (3.7b) and we compute successive PN approximations to the wave amplitude as functions of time; then we compare the results with the modulus of the actual numerical amplitude $|Mr\,\psi_{l\,,m}|$.

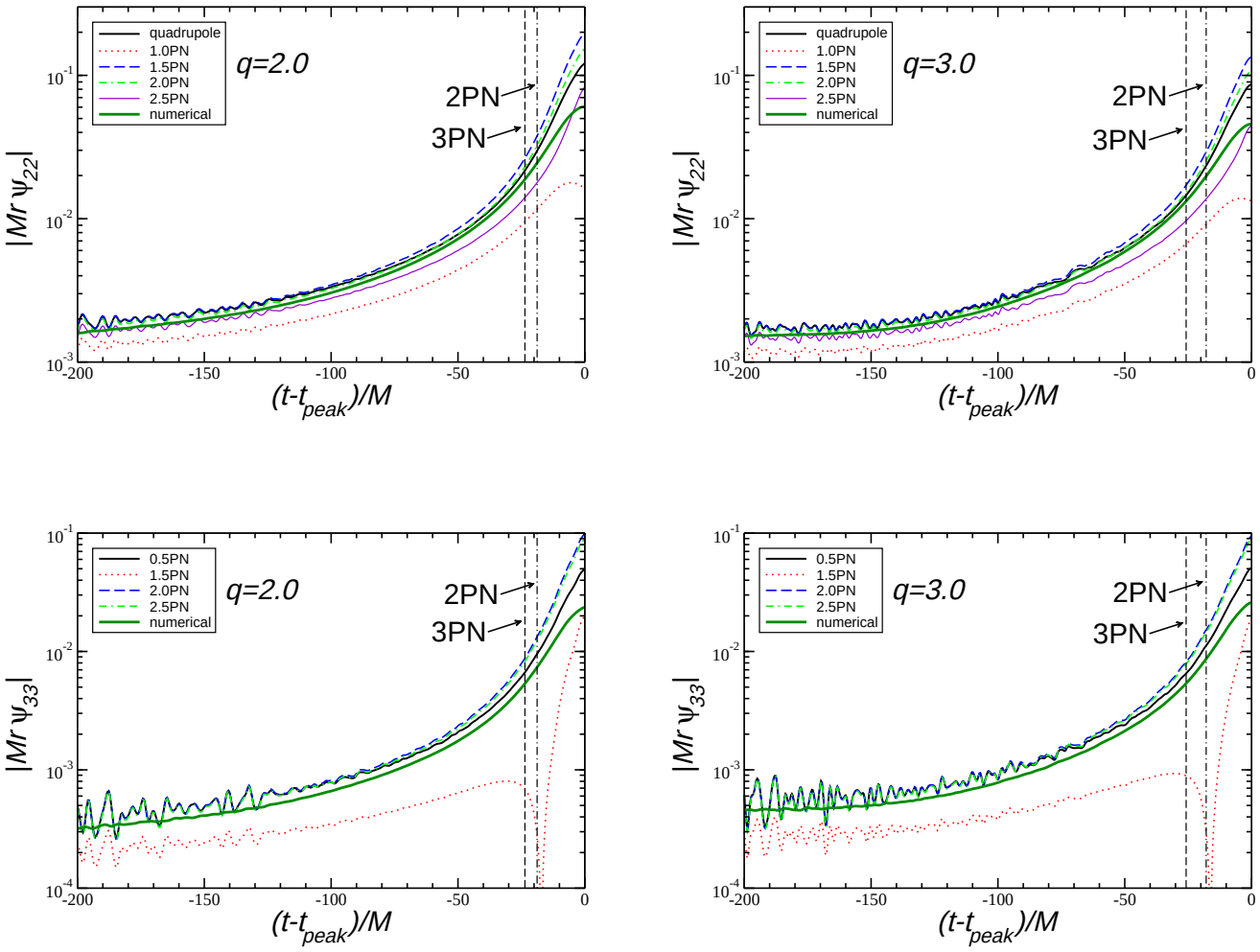

FIG. 8: Amplitudes obtained by substituting ω_{Dm} into the PNQC equations are compared with the numerical amplitude. All plots refer to run D8. Figures on the left refer to $q = 2.0$, those on the right to $q = 3.0$. The top row shows amplitudes for $l = m = 2$, the bottom row for $l = m = 3$. Vertical lines mark 2PN and 3PN estimates of the ISCO.

At early times we clearly see oscillations in the PN estimates of the amplitude, that damp away as the binary evolves. These oscillations are due to the fact that ω_{D2} is very noisy near the beginning of the simulation (compare the early portion of Fig. 6), and they would not be present if we used as a reference ω_c, which is much smoother at early

times[3]. The first PN correction is seen to deviate significantly from all other PN approximations. This is a general feature of PN calculations. The poor convergence properties of the PN approximation have long been known in the point-particle limit [14], where exact results can be obtained by simply integrating the Zerilli equation. Fortunately, in our case higher-order PN expansions (of order higher than 1PN for $l = m = 2$) are reasonably consistent with each other. Our best guess at the "true" solution (i.e., the 2.5PN approximation) has the smallest error at relatively large separations, but it does not seem to be very good close to merger.

A comparison of the PNQC orbital frequencies computed at different PN orders is also instructive. Let us assume that, within the accuracy of our numerical simulations, ω_{Dm} is a good representation of the "true" orbital frequency of the binary[4]. If by increasing the PN order we find that $\omega_{\rm PNQC}$ gets closer and closer to ω_{Dm}, this would provide an indication that the PN expansion is converging to the actual solution of the full, nonlinear problem.

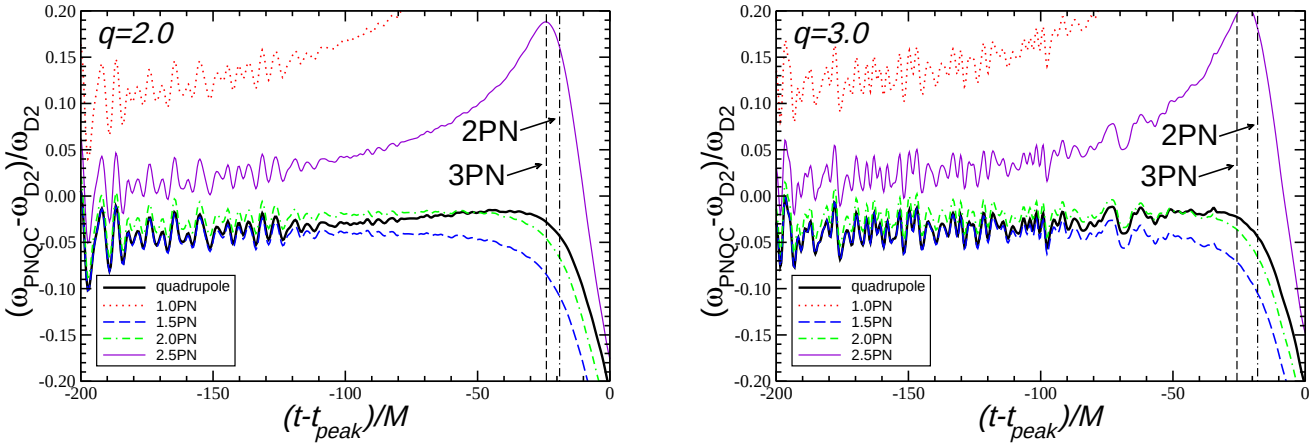

FIG. 9: Relative deviation between the orbital frequency obtained from the PNQC inspiral formulae and the "true" frequency of the signal ω_{D2}. Plots refer to run D8 and $q = 2.0$ (left), $q = 3.0$ (right).

Fig. 9 shows the relative deviation between $\omega_{\rm PNQC}$, as computed by keeping more and more terms in Eqs. (3.7), and the supposedly more accurate orbital frequency ω_{D2}. Once again, at early-times we see oscillations in the relative deviation, that damp away as the binary evolves. The magnitude of the relative deviation $|(\omega_{\rm PNQC} - \omega_{D2})/\omega_{D2}|$ can be taken as an indicator of the accuracy of the PN approximation. These plots confirm, from a slightly different perspective, the non-monotonic convergence of the PN series. After the transition from inspiral to plunge (very roughly corresponding to the vertical lines, marking the estimated location of the ISCO at 2PN and 3PN) the PNQC frequency, which is only valid for the inspiral phase, clearly decouples from ω_{D2}, and the relative error becomes much larger. Perhaps in the future, as the accuracy of numerical simulations increases, it will be possible to use the change in slope of $|(\omega_{\rm PNQC} - \omega_{D2})/\omega_{D2}|$ to monitor the occurrence of an orbital instability (the "plunge phase") in full general relativity.

We already pointed out that our assumed "exact" orbital frequency, ω_{D2}, is in practice affected by various sources of numerical error: finite-differencing errors, the finite extraction radius and the initial data burst all introduce uncertainties. To bracket these uncertainties, in Fig. 10 we choose one of our longest runs (D10 for $q = 1.0$) and we study the effect of resolution and extraction radius on $|(\omega_{\rm PNQC} - \omega_{D2})/\omega_{D2}|$. Two remarkable features emerge from this plot. First of all, at lower resolution the "wiggles" induced by initial data are still visible at later times. The second effect is perhaps the most important for matching numerical waveforms to the PN approximation, and

[3] The reason why we do *not* choose ω_c as a baseline for comparison is that this frequency significantly deviates from the others close to merger, where the comparison between PN theory and numerical simulations is most interesting.

[4] In practice, of course, this is only true in an approximate sense. For example, in the early inspiral ω_{Dm} is heavily contaminated by the initial data burst and boundary reflection noise; finite differencing effects will introduce errors in the calculation of ω_{Dm} given the computed waveform; and finally, the waveform itself is obtained at finite extraction radius, introducing additional uncertainties. What we are really assuming is that, taken together, all of these effects are smaller than the errors introduced by the PN approximation to general relativity.

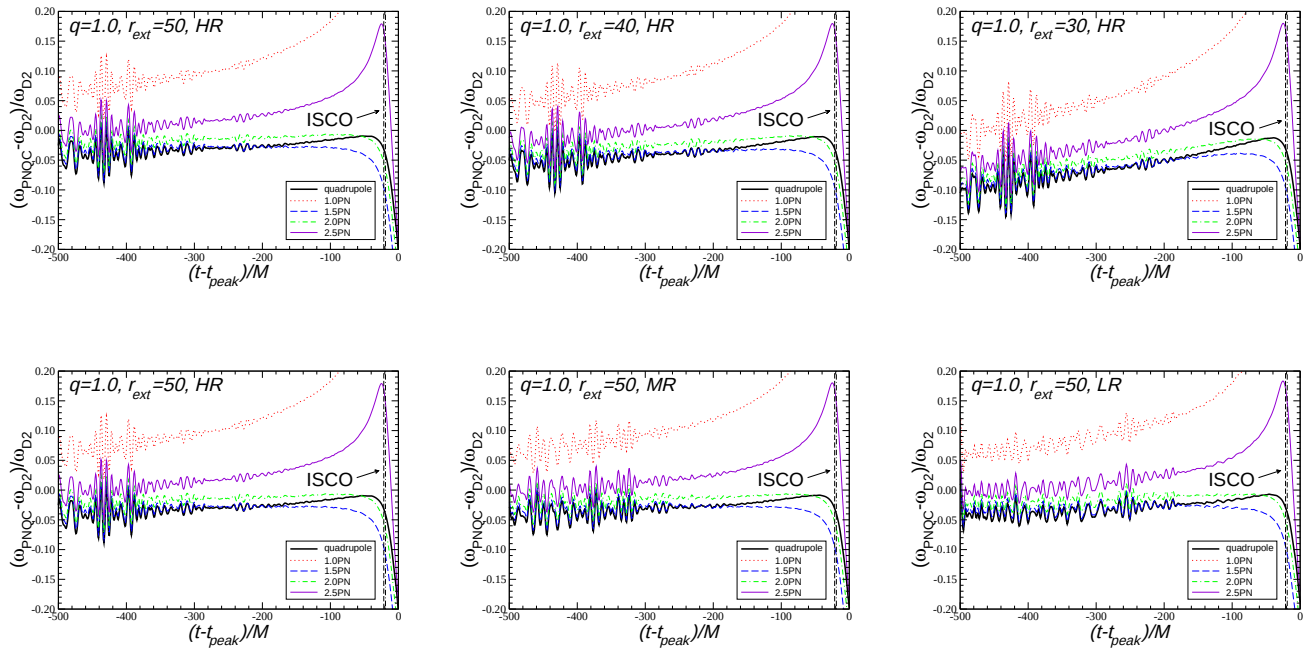

FIG. 10: The effect of changing extraction radius (top) and resolution (bottom) on the errors. These plots refer to mass ratio $q = 1.0$, run D10. The extraction radii ($r_{\rm ext} = 30,\ 40$ and 50) and resolutions (HR, MR, LR stands for high, medium and low resolution, respectively) are indicated in the inset.

for building template banks for gravitational wave detection. We see that *small extraction radii produce a systematic bias (i.e., a larger deviation of* $\omega_{\rm PNQC}$ *from* ω_{Dm}*) at large orbital separations.* This effect is easily understandable: the typical wavelength in the "early" inspiral part is of order $\lambda \sim 100M$, which is actually *larger* than the typical extraction radii used in the present simulations. Such small extraction radii inevitably produce a bias in the waveform. We observed a similar, and probably related problem in the context of what we called the memory effect (Section II A).

C. Radiated energy and angular momentum

1. *Total radiated energy*

The total radiated energy computed from wave-extraction methods, and the energy radiated into each multipole l, are listed in Table IV and plotted in Fig. 11. For reference we list our results with four significant digits, but only the first two digits should be reliable. A rough estimate of the errors can be obtained by comparing results at high and low resolution. This comparison can be found in Table V below, where we also list the radiated energies and the final angular momenta computed using QNM fits.

Table IV and Fig. 11 clearly illustrate that the relative contribution of higher multipoles becomes more relevant as the mass ratio increases. As expected from symmetry considerations (and from the calculations in Appendix A), odd values of l are suppressed as the mass ratio $q \to 1$. The dominant components for all mass ratios are $(l,\ m) = (2,\ 2),\ (3,\ 3),\ (4,\ 4)$. We often observe a non-negligible contribution (partly due to spurious initial data radiation) also in $(l,\ m) = (2,\ 1),\ (2,\ 0),\ (4,\ 0),\ (5,\ 5)$. The initial data radiation burst can be eliminated by starting the integration of the energy flux after the initial burst has passed. In Table IV we decided, somewhat arbitrarily, to start the integration at $t = 75M$. Changes in the starting time have a marginal impact on the results: at the level of 0.1% for the $(2\,,2)$ modes, and of about a few per cent for the weakest modes (which have higher errors anyway).

In practical applications it may be useful to have some fitting formulas for the total energy radiated and for the contribution of different multipoles. Since the energy is proportional to $|\dot{\Psi}_4|^2$, and the $l = m = 2$ component $\psi_{2\,,2} \sim \eta$ dominates the radiation, we expect the total radiated energy to be roughly proportional to η^2 (recall that

TABLE IV: Total energy radiated in merger simulations of unequal mass black holes, and percentage of energy in the different multipoles (normalized to the total energy radiated in $l = 2, \ldots, 5$). The numbers refer to high-resolution D7 runs. For $q = 2.0$ the $l = m = 4$ component is slightly suppressed (this is because more energy is going into higher multipoles, eg. $l = m = 5$). In parentheses we list numbers obtained eliminating the initial data burst (in practice, we remove all data for $t < t_0 = 75M$).

q	$\Delta E_{\rm tot}/M(\%)$	$l=2$	$l=3$	$l=4$	$l=5$
1.0	3.718	98.02	0.43	1.521	0.03
	(3.651)	(98.08)	(0.37)	(1.526)	(0.02)
1.5	3.403	96.43	2.07	1.384	0.12
	(3.340)	(96.51)	(2.01)	(1.369)	(0.11)
2.0	2.858	93.62	4.70	1.426	0.26
	(2.802)	(93.73)	(4.65)	(1.388)	(0.24)
2.5	2.383	90.87	6.99	1.730	0.40
	(2.334)	(91.00)	(6.96)	(1.679)	(0.36)
3.0	2.000	88.55	8.88	2.036	0.54
	(1.958)	(88.68)	(8.85)	(1.975)	(0.49)
3.5	1.695	86.56	10.37	2.393	0.68
	(1.659)	(86.70)	(10.36)	(2.326)	(0.61)
4.0	1.451	84.84	11.57	2.770	0.81
	(1.419)	(84.99)	(11.56)	(2.700)	(0.75)

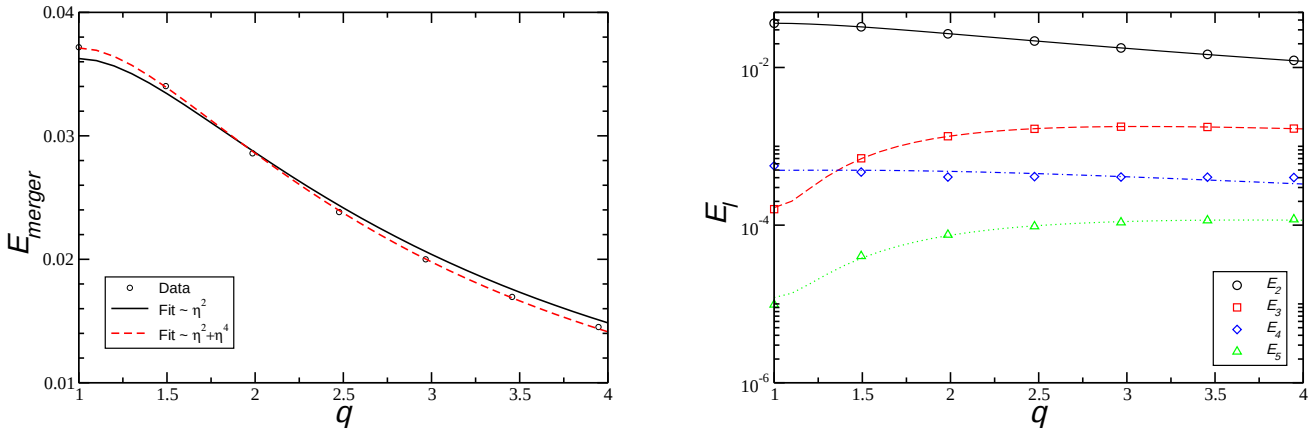

FIG. 11: Left: total energy $E_{\rm tot}$ radiated in the merger (including the initial data burst) fitted by Eq. (3.13) and Eq. (3.14), respectively. Right: numerical data for the energy E_l emitted into each multipole l are compared with the fitting functions (3.15). Notice the suppression of odd multipoles as the mass ratio $q \to 1$.

the symmetric mass ratio $\eta = q/(1+q)^2$ tends to $1/4$ in the equal mass limit). Indeed, it turns out that the total radiated energy *in the merger* $E_{\rm tot}$ is fitted extremely well (deviations from the data being $\lesssim 4\%$) by the function

$$\frac{\Delta E_{\rm tot}}{M} = 0.036262 \left[\frac{4q}{(1+q)^2}\right]^2 . \tag{3.13}$$

Fitting by a higher-order function, eg.

$$\frac{\Delta E_{\rm tot}}{M} = 0.032661 \left[\frac{4q}{(1+q)^2}\right]^2 + 0.004458 \left[\frac{4q}{(1+q)^2}\right]^4 , \tag{3.14}$$

marginally improves the quality of the fit, bringing the agreement with the data to the level of $\sim 1\%$ (see the left panel of Fig. 11).

The different multipolar components are slightly harder to fit. Since again we expect the energy in each component to be proportional to the square of the amplitudes, the even components with $l = m$ should be proportional to

$\left[4q/(1+q)^2\right]^2$, and the odd components should scale with $\left[q(q-1)/(1+q)^3\right]^2$. After some experimentation with including higher-order corrections in η, we found that the following functions provide a satisfactory fit of the data:

$$E_l = c_1 \left[\frac{4q}{(1+q)^2}\right]^2 + c_2 \left[\frac{4q}{(1+q)^2}\right]^4 , \qquad (l \text{ even}) , \tag{3.15a}$$

$$E_l = d_1 + \left[\frac{q(q-1)}{(1+q)^3}\right]^2 \left(d_2 + d_3 \left[\frac{4q}{(1+q)^2}\right]^2 \right) , \qquad (l \text{ odd}) . \tag{3.15b}$$

In principle d_1 should be zero, but due to the initial burst of radiation it is not, and including a small but non-zero d_1 significantly improves the quality of the fits for odd l. For $l = 2$, we find the best-fit coefficients to be $(c_1 = 0.024231\,, c_2 = 0.012163)$; for $l = 4$, they are $(c_1 = 0.0010294\,, c_2 = -0.0005328)$. For $l = 3$ we find $(d_1 = 0.00017\,, d_2 = 0.10509\,, d_3 = 0.13990)$, and for $l = 5$ $(d_1 = 0.000012\,, d_2 = 0.011020\,, d_3 = 0.000463)$. Numerical data for different multipolar contributions and the corresponding fitting functions are shown in the right panel of Fig. 11.

2. *Final angular momentum*

A good fit to the final angular momentum, for small mass ratios, was found in Ref. [3]:

$$j \sim 0.089 + 2.4 \frac{q}{(1+q)^2} . \tag{3.16}$$

In this paper we compute the final angular momentum in two ways. One estimate, that we denote by $j_{\rm fin}$, is obtained by subtracting the total radiated angular momentum (as computed by wave extraction) from the total angular momentum at the beginning of the simulation. A second estimate is based on QNM fits, and will be described in detail in Section IV below. In the two cases we found that a very good fit (accurate to within $\sim 1\%$) is given by

$$j_{\rm QNM} \simeq 3.352 \frac{q}{(1+q)^2} - 2.461 \frac{q^2}{(1+q)^4} , \tag{3.17a}$$

$$j_{\rm fin} \simeq 3.272 \frac{q}{(1+q)^2} - 2.075 \frac{q^2}{(1+q)^4} . \tag{3.17b}$$

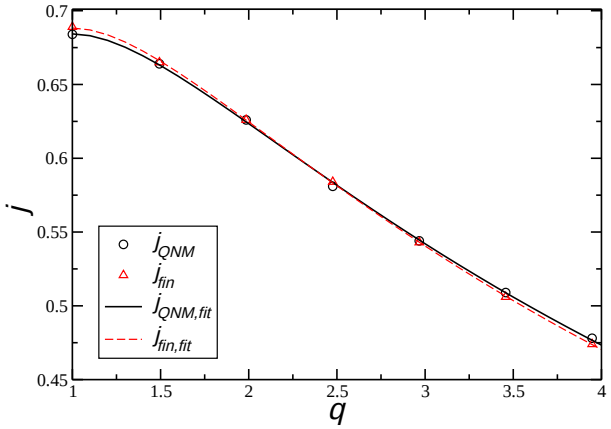

FIG. 12: Angular momentum estimated from a QNM fit and from wave extraction, and corresponding fits.

The quality of these fits, and the extremely good agreement between the two different estimates of the final angular momentum, is illustrated in Fig. 12. The actual data can be found in Table V below. In that Table we also list

results obtained by fitting low resolution simulations, to give an idea of the errors involved in our angular momentum estimates. We expect the estimates to be accurate within about $\sim 1\%$ for $q > 3$, errors being even smaller as $q \to 1$.

The functional form of Eq. (3.17) can be justified by a simple physical argument. Consider an extreme-mass ratio binary with the smaller body orbiting near the ISCO. The orbital angular momentum at the ISCO, in the small mass ratio limit and for non-spinning bodies, is given by

$$L_{\rm ISCO} = 2\sqrt{3} M_1 M_2 \,. \tag{3.18}$$

In Appendix B we show that the numerical results for the angular momentum radiated after the ISCO are well fitted by Eq. (B1), that we reproduce here:

$$\frac{\Delta J_{\rm ISCO}}{M^2} \approx 2.029 \frac{q^2}{(1+q)^4} \,. \tag{3.19}$$

Therefore the angular momentum of the final hole should be well described by

$$j \approx 2\sqrt{3}\frac{q}{(1+q)^2} - 2.029\frac{q^2}{(1+q)^4} = 3.464\frac{q}{(1+q)^2} - 2.029\frac{q^2}{(1+q)^4} \,, \tag{3.20}$$

which is remarkably close to the best fits (3.17).

3. *Energy and angular momentum fluxes*

The purpose of this Section is to compare analytical PN estimates of the energy and angular momentum flux for a quasi-circular, unequal mass inspiral against the corresponding numerical calculations. To begin with, we summarize how to compute these quantities in PN theory and in numerical relativity.

The gravitational wave energy flux emitted by a binary moving along an adiabatic sequence of circular orbits is currently known analytically through 3.5PN order for non-spinning BHs in circular orbits [27]. It reads

$$\begin{aligned} F_{\rm E}^{\rm PNQC} &= \frac{32}{5}\eta^2 (M\Omega)^{10/3}\Bigg\{1 + \left(-\frac{1247}{336} - \frac{35}{12}\eta\right)(M\,\Omega)^{2/3} + 4\pi (M\,\Omega) \\ &+ \left(-\frac{44711}{9072} + \frac{9271}{504}\eta + \frac{65}{18}\eta^2\right)(M\,\Omega)^{4/3} + \left(-\frac{8191}{672} - \frac{583}{24}\eta\right)\pi (m\,\Omega)^{5/3} \\ &+ \left(\frac{6643739519}{69854400} + \frac{16}{3}\pi^2 - \frac{1712}{105}\gamma_E - \frac{856}{105}\ln(16\,(M\,\Omega))\right. \\ &+ \left.\left[-\frac{134543}{7776} + \frac{41}{48}\pi^2\right]\eta - \frac{94403}{3024}\eta^2 - \frac{775}{324}\eta^3\right)(M\,\Omega)^2 \\ &+ \left(-\frac{16285}{504} + \frac{214745}{1728}\eta + \frac{193385}{3024}\eta^2\right)\pi (M\,\Omega)^{7/3}\Bigg\} \,, \end{aligned} \tag{3.21}$$

where γ_E is Euler's number and η denotes, as usual, the symmetric mass ratio. The numerical energy flux can be obtained from the mode amplitudes $Mr\,\psi_{l\,,m}(t)$ as

$$F_{\rm E} = \frac{dE}{dt} = \sum_{l=2}^{\infty} F_{{\rm E}\,,l} = \sum_{l=2}^{\infty}\sum_{m=-l}^{l} F_{{\rm E}\,,lm} = \frac{1}{16\pi}\sum_{l\,,m} |D_{l\,,m}(t)|^2, \tag{3.22}$$

where $D_{l\,,m}(t)$ is a dimensionless first time integral of $\psi_{lm}(t)$ defined by

$$D_{l\,,m}(t) \equiv \frac{1}{M}\int_0^t dt' Mr\,\psi_{l\,,m}(t') \,. \tag{3.23}$$

Each term in the sum (3.22) represents the multipolar contribution of a different mode. A PN estimate for the flux in each $(l\,,m)$ mode can be obtained by using the expansion of Ψ_4 in spin-weighted spherical harmonics. Using the same approximation discussed in Section III A, namely neglecting the logarithmic term in the phase, we get the folllowing PN estimate for the $(l\,,m)$ component of the energy flux:

$$F_{{\rm E}\,,lm}^{\rm PNQC} = \frac{dE_{l\,,m}}{dt} = \frac{1}{16\pi m^2\Omega^2}|Mr\,\psi_{l\,,m}|^2 \,, \tag{3.24}$$

where we use the best available PN expansions of $Mr\,\psi_{l\,,m}$, as listed in Appendix A. Again, the 2.5PN term in the $l=m=2$ waveform requires modification. To the level of accuracy of our results, this modification is irrelevant.

For quasi-circular orbits, the PN angular momentum flux is simply

$$F_{\rm J}^{\rm PNQC}=\frac{1}{\Omega}F_{\rm E}^{\rm PNQC}\,. \tag{3.25}$$

The numerical angular momentum flux $F_{\rm J}$ can be computed using Eq. (2.5).

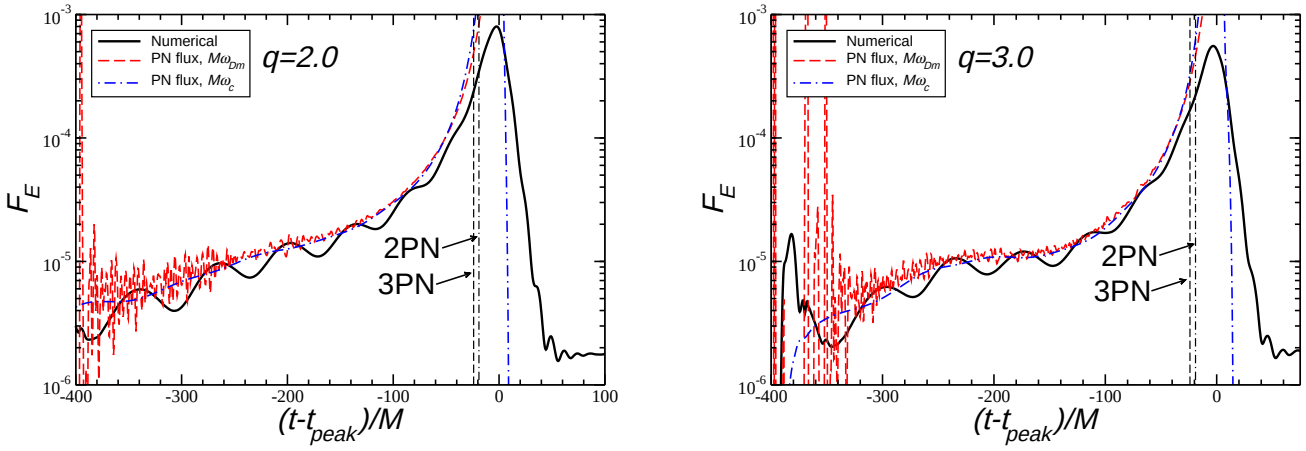

FIG. 13: Total energy flux computed numerically and using Eq. (3.21), using two different estimates of the orbital frequency (ω_{Dm} and ω_c). The plots refer to run D8. On the left we show results for $q=2.0$, on the right for $q=3.0$.

In Fig. 13 we show the total energy flux, as computed numerically, and we compare it with the PNQC energy flux obtained by substituting two different estimates of the orbital frequency, ω_{Dm} and ω_c, into Eq. (3.24). Some features of this plot should be quite familiar from the discussion in Section III B. First of all, because of the (small) orbital eccentricity, the numerical flux oscillates around a "mean" value given by the PNQC estimate. The PNQC and numerical fluxes start deviating quite clearly $\sim 20-40M$ before the ISCO, and the agreement between the two gets slightly better for larger mass ratio. A remarkable feature of the numerical flux is that it does *not* reduce to zero after the exponentially decaying ringdown phase. We believe this to be, at least in part[5], an artifact of the memory effect discussed in Section II A.

The relative contribution of higher-l multipoles to the flux increases with mass ratio, and it also increases as we get close to merger. To leading order in a PNQC expansion we can show that the ratio of the dominant multipolar components of the flux as a function of frequency (or alternatively, as a function of time to coalescence) is given by

$$\frac{F_{E,33}}{F_{E,22}}\simeq\frac{40}{21}\left(\frac{27}{32}\right)^2\left(\frac{\delta M}{M}\right)^2(M\Omega)^{2/3}\simeq\frac{10}{21}\left(\frac{27}{32}\right)^2\left(\frac{\delta M}{M}\right)^2\left(\frac{5}{\eta}\right)^{1/4}(t_c-t)^{-1/4}\,, \tag{3.26a}$$

$$\frac{F_{E,44}}{F_{E,22}}\simeq\frac{1280}{567}(1-3\eta)^2(M\Omega)^{4/3}\simeq\frac{80}{567}(1-3\eta)^2\left(\frac{5}{\eta}\right)^{1/2}(t_c-t)^{-1/2}\,, \tag{3.26b}$$

where t_c is the coalescence time.

In Fig. 14 we show the ratio of the *integrated* energy flux in different multipolar components as a function of time. This plot confirms that the relative contribution of higher multipoles increases for large mass ratio, and (for given mass ratio) it increases as we get close to merger.

Finally, in Fig. 15 we compare the numerical angular momentum flux with the PNQC prediction. The oscillations in the numerical flux seem to be a general feature: they can also be seen in Fig. 27 of BCP, where they are attributed

[5] Some contribution to the non-zero flux at late times may come from numerical noise.

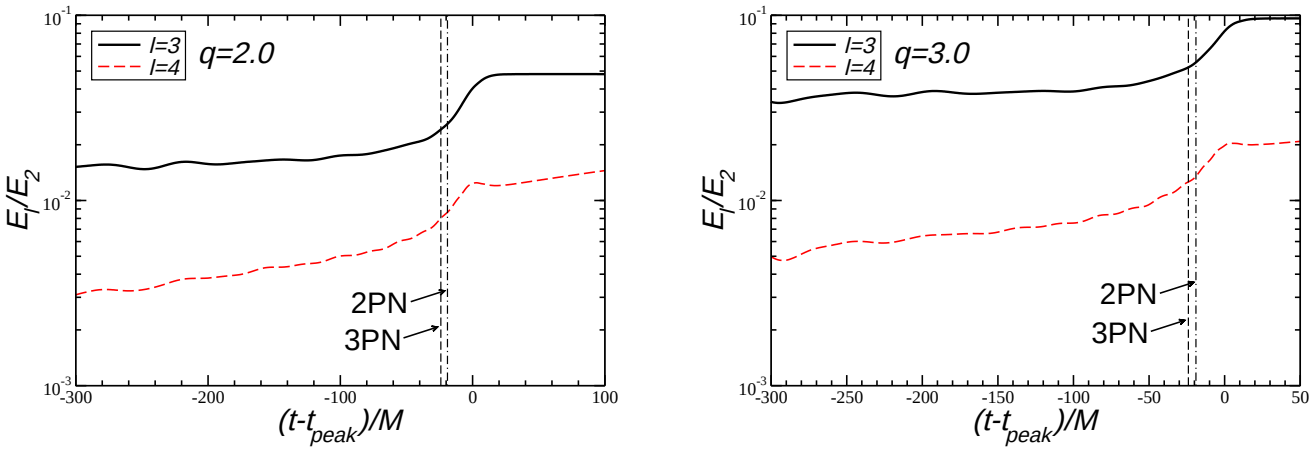

FIG. 14: Relative contribution of different multipolar components to the integrated energy flux as a function of time. The plots refer to run D8. On the left we show results for $q = 2.0$, on the right for $q = 3.0$.

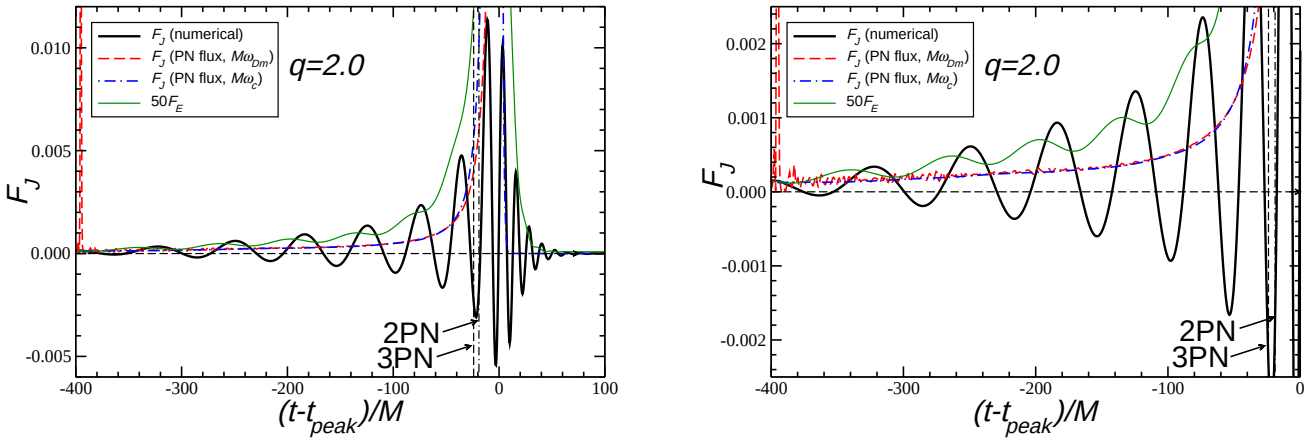

FIG. 15: Total angular momentum flux computed numerically (solid line) and substituting two different estimates of the orbital frequency, ω_{Dm} and ω_c, into Eq. (3.25). We overplot the energy flux (multiplied by 50) for $q = 2.0$ and run D8, to show that zero-crossings of the angular momentum flux correspond (roughly) to local extrema of the energy flux.

in part to improper initial conditions in the time integrals required to obtain the flux from Ψ_4. Our results confirm that, as remarked by BCP, Eq. (3.25) seems to hold *on average* throughout the whole inspiral (possibly with larger deviations close to merger). In addition we point out an interesting correlation between the energy and angular momentum fluxes. In Fig. 15, besides the angular momentum flux, we also plot the *energy* flux $F_{\rm E}$ (multiplied by 50 for scale). The plots clearly show that oscillations in $F_{\rm J}$ have (roughly) the same period as oscillations in $F_{\rm E}$. Perhaps this could be evidence that the observed oscillations are somehow related with the orbital eccentricity, minima and maxima corresponding to periastron and apoastron. A detailed study of this correlation is beyond the scope of this paper.

IV. THE MERGER-RINGDOWN TRANSITION

The goal of this Section is to study the ringdown phase, and to explore the properties of the final black hole formed after merger. We will compare different fitting methods to extract information from the ringdown waveforms. As discussed in [15], such a comparison can help us resolve real physical effects (such as, for example, time variations of the ringdown frequencies) from systematic parameter estimation errors due to the variance and bias of each particular fitting algorithm. In particular, here we consider two classes of fitting algorithms: the matrix pencil (MP) and Kumaresan-Tufts (KT) methods, which are modern variants of the so-called Prony linear-estimation algorithms for damped exponentials in noise [30, 31]; and a standard non-linear least-squares technique, the Levenberg-Marquardt (LM) algorithm [32].

In [15] we pointed out that Prony methods have a number of advantages with respect to standard non-linear least-squares techniques: (i) They do not require an *initial guess* of the fitting parameters; (ii) They provide us with a simple, efficient way to estimate QNM frequencies for the *overtones*, and even to estimate how many overtones are present in the signal; (iii) They are explicitly designed to deal with *complex signals*, so they should be most useful for "generic" waveforms, such as those produced by unequal mass, spinning, precessing black hole binaries. If the polarization is not circular, the plus and cross polarizations of the gravitational radiation (or equivalently, the real and imaginary parts of Ψ_4) will carry independent information, and fitting them simultaneously becomes a necessity; (iv) Statistical properties of Prony-based methods in the presence of noise (such as their variance and bias) are well studied and under control. When compared with the LM algorithm, Prony methods seems to have comparable variance but slightly smaller bias.

Our approach to the ringdown waveform is quite different in spirit from the fitting procedure adopted by BCP. They choose the real (or, alternatively, the imaginary) part of Ψ_4, a procedure which discards half the information in cases of non-trivial polarization. They fit $\mathrm{Re}(\psi_{l\,,m})$, or alternatively $\mathrm{Im}(\psi_{l\,,m})$, by a four-parameter function of the form

$$\mathrm{Re}(\psi^{\mathrm{fit}}_{l\,,m}) = \mathrm{Re}\left\{\sum_n \mathcal{A}_{lmn} e^{-i[\hat{\omega}_{lmn}(j,\ M_{\mathrm{fin}})(t-t_{\mathrm{peak}})+\phi_{lmn}]}\right\}, \tag{4.1}$$

where $\hat{\omega}_{lmn}(j,\ M_{\mathrm{fin}})$ denotes a complex QNM frequency. The final black hole's mass and spin $(j\,, M_{\mathrm{fin}})$ are taken as the independent fitting parameters, and the different QNM frequencies $\hat{\omega}_{lmn}$ are obtained, for given $(j,\ M_{\mathrm{fin}})$, either by using fitting relations or by interpolating numerical tables [33].

Adding overtones provides a good fit of the strong-field phase by effectively *increasing* the number of fitting parameters (mode amplitudes $\mathcal{A}_{lmn}$ and phases ϕ_{lmn} of the overtones). This idea is perfectly consistent with QNM expansions in the context of linear black hole perturbation theory. An obvious drawback of the idea is that it *assumes* the validity of linear perturbation theory to extend the QNM fit before the peak of the radiation. Another potential problem is that, by using many fitting parameters, we can always get very good agreement with the numerical waveforms, but we do not necessarily get a better physical description of QNM excitation. Furthermore, since the procedure assumes that the waveform can be expanded as a sum over overtones for the given *spherical* (rather than *spheroidal*) harmonic indices $(l,\ m)$, it may be oblivious (by construction) to rotational mode-coupling and non-linearities. Both effects should be present in the initial portion of the ringdown waveform, because rotational mode-coupling is induced by expanding the radiation in the "wrong" set of angular functions [16] and because nonlinearities should be sizeable immediately after merger, producing mode coupling [34, 35].

In order to explore the possibility of rotational or non-linear mode coupling, here we adopt a different fitting strategy. By sliding a time window (chosen according to the criteria described below) through the signal, we try to extract the time dependence of QNM frequencies as accurately as possible. Prony methods allow us to fit the full waveform at once, not only its real (or imaginary) part. For simplicity, in this paper we do not attempt to include overtones in the fit, but we only assess the accuracy of fits of the fundamental QNM. In [15] we have shown that the QNM frequency and damping time evolve quite rapidly right after merger. This evolution could be interpreted as a bias in the fitted frequencies induced by the omission of higher overtones; or, alternatively, it could mean that the mass and angular momentum of the newly formed, dynamical black hole spacetime really are *evolving* on timescales much smaller than the QNM timescales, producing an effective redshift in the QNM frequencies [35].

A. Choice of the fitting window

Independently of the chosen fitting method, there is some arbitrariness in choosing the time interval $[t_0,\ t_f]$ to perform the fit. A well-known problem with the merger-ringdown transition is that we do not know *a priori* when the ringdown starts [1, 16, 36]. This problem is discussed at length in Section IV D below. Ideally, the starting time for

the fit t_0 should be determined by a compromise between the following requirements: (i) t_0 should be small enough to include the largest possible number of data points: in particular, we do not want to miss the large amplitude, strong-field part of the waveform after merger; (ii) t_0 should be large enough that we do not include parts of the waveform which are *not* well described by a superposition of complex exponentials: the inclusion of inspiral and merger in the ringdown waveform would produce a bias in the QNM frequencies.

A judicious choice of t_f is also necessary. Usually we would like the time window to be as large as possible, but Fig. 1 and Fig. 2 clearly show that the low amplitude, late-time signal is usually dominated by numerical noise (mainly caused by reflection from the boundaries). This noise can reduce the quality of the fit, especially for the subdominant components with $l > 2$ and for large values of t_0. A practical criterion for the choice of t_f is suggested by a look at Fig. 2. If the ringdown waveform were not affected by noise from boundary reflections, $|Mr\,\psi_{l\,,m}|$ should decay linearly on the logarithmic scale of the plots[6]. At low signal amplitudes, we see boundary noise-induced wiggles superimposed to this linear decay. The first occurrence of these wiggles is a good indicator of the time t_f at which numerical results cannot be trusted anymore. To test the robustness of fitting results to late-time numerical noise, while at the same time keeping the largest number of data points in the waveform, we decided to use two different "cutoff criteria":

1) "Relative" cutoff: remove from the waveforms all data for times $t > t_f = t_{\rm rel}$, where $t_{\rm rel}$ is the time when the amplitude of each multipolar component $|Mr\,\psi_{l\,,m}|$ becomes less than some factor $\psi_{\rm cutoff}$ times the peak amplitude $|\psi_{l\,,m}(t_{\rm peak})|$ (values of $t_{\rm peak}$ for $l = m = 2$ are listed in Table II):

$$\frac{|Mr\,\psi_{l\,,m}(t_{\rm rel})|}{|Mr\,\psi_{l\,,m}(t_{\rm peak})|} < \psi_{\rm cutoff}\,. \tag{4.2}$$

2) "Absolute" cutoff: remove from the fit all data with $t > t_f = t_{\rm abs}$, where $t_{\rm abs}$ is the time at which the *absolute* value of the amplitude $|Mr\,\psi_{l\,,m}| < \psi_{\rm cutoff}/10$.

The choice of the cutoff amplitude is somewhat arbitrary. We chose $\psi_{\rm cutoff} = 10^{-3}$ for low resolution, and $\psi_{\rm cutoff} = 10^{-4}$ for high resolution.

For each chosen t_f, we compare the different fitting routines as we let t_0 vary in the range $[t_{\rm peak},\ t_f]$. By monitoring the convergence of the QNM frequencies to some "asymptotic" value as $t_0 \to \infty$, we can tell if the black hole settles down to a stationary Kerr state, or if, on the contrary, non-linearities and mode coupling are always present. Notice that as t_0 grows the signal amplitude decreases exponentially, and we effectively reduce the signal-to-noise ratio (SNR) in our fitting window. Robust fitting methods should give reasonable results even for large values of t_0 (that is, modest values of the SNR).

B. From ringdown frequencies to black hole parameters

In [15] we fitted the frequency ω and quality factor[7] Q of the $l = m = 2$ fundamental mode of the newly-formed black hole as a function of t_0. The results show that the QNM frequencies evolve quite rapidly in the first $10M - 20M$ after merger: see in particular the bottom panels of Fig. 7 in [15], where a rapid decrease of $Q(t_0)$ is clearly visible for simulation times $240 \lesssim t_0/M \lesssim 260M$. Assuming linear perturbation theory to be valid, the real and imaginary parts of each QNM frequency are unique functions of the mass $M_{\rm fin}$ and of the (dimensionless) angular momentum $j = J/M_{\rm fin}^2$ of the final black hole: say, $M_{\rm fin}\omega_{lmn} = f_{lmn}(j)$, $M_{\rm fin}\alpha_{lmn} = M_{\rm fin}/\tau_{lmn} = g_{lmn}(j)$ [33]. The quality factor of the oscillations Q_{lmn}, being dimensionless, must be a function of j only. A numerical calculation shows that for the dominant modes ($l = m = 2,\ 3,\ 4$) this function is monotonic and invertible (see eg. Fig. 5 in Ref. [33]). Therefore we can easily invert $Q_{lmn}(j)$ to compute $j(t_0)$, either by using fitting relations or by interpolating QNM tables.

The results of this inversion for the fundamental $l = m = 2$ mode of the black hole formed as a result of inspirals with $q = 1.5$ and $q = 3.0$ are shown in Fig. 16. As the origin of the time axis we choose the time $t_{\rm peak}$ at which the $l = m = 2$ amplitude has a maximum (see Table II). Solid lines refer to the "absolute" truncation criterion, and dashed lines to the "relative" truncation criterion (see Section IV A). On the scale of these plots, different

---

[6] With larger resolution and longer running times, eventually the exponential decay should turn into the well known power-law tail induced by backscattering of the radiation off the spacetime curvature [37]. In the simulations we consider, noise produced by boundary effects is large enough that this effect is not visible.

[7] We recall that the quality factor $Q \equiv |\omega/(2\alpha)|$, where $\alpha = 1/\tau$ is the imaginary part of the QNM frequency, i.e. the inverse of the damping time.

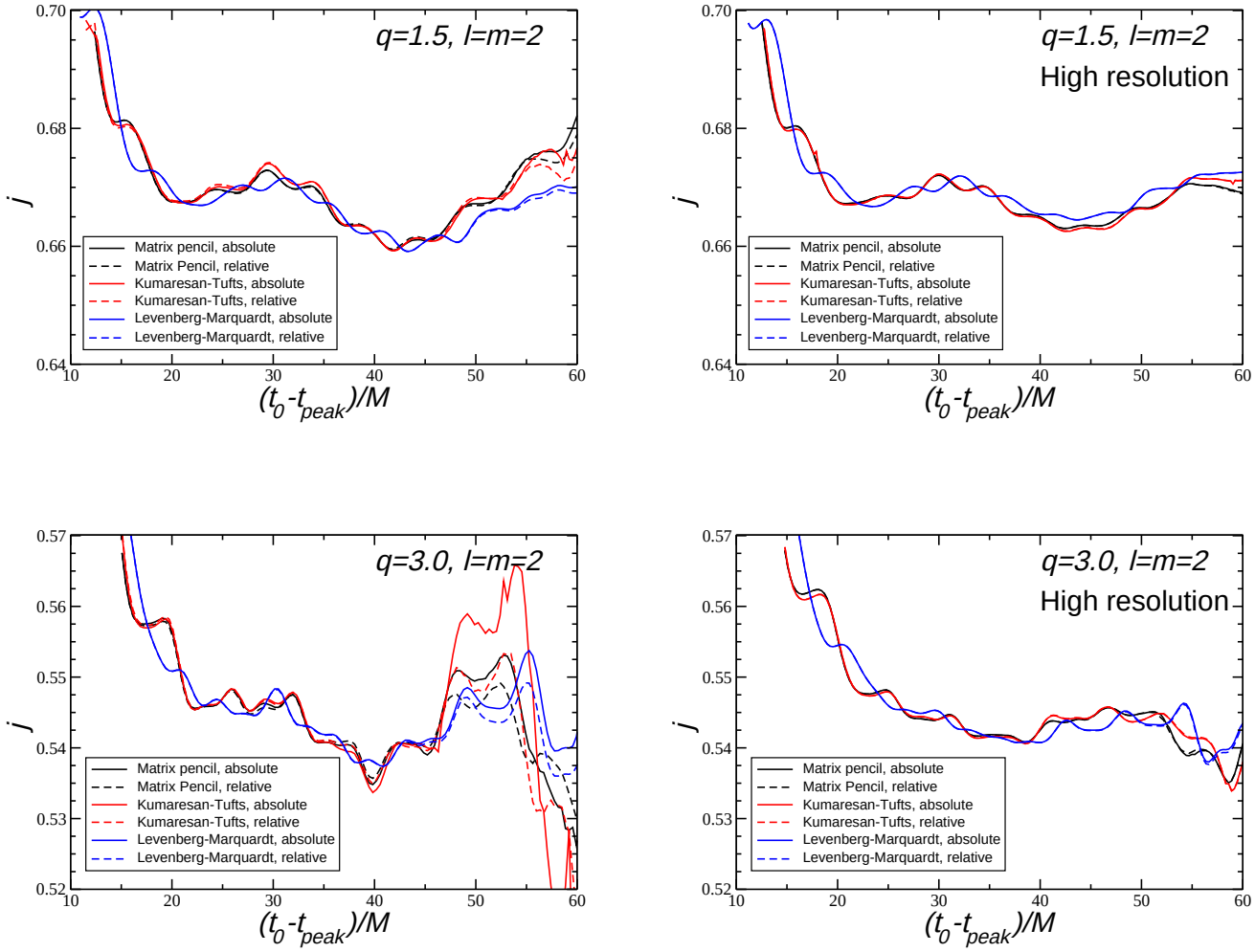

FIG. 16: Estimate of the angular momentum from a fit of the $l = m = 2$ waveform using different methods. Top panels refer to a merger with $q = 1.5$, bottom panels to a merger with $q = 3.0$. Results on the left were obtained from low-resolution D7 runs, and those on the right from high-resolution D7 runs.

truncation criteria affect the estimated parameters only for low-resolution simulations and at relatively late starting times ($t_0/M \gtrsim 50$), when the signal amplitude becomes comparable to numerical noise. Not surprisingly, there is remarkable agreement between KT and MP methods. The main difference when we use the non-linear least-squares LM method is a *systematic time-shift in the angular momentum*: the blue lines would be in excellent agreement with the prediction from Prony methods if shifted backwards in time by $\Delta t_0 \sim 2 - 3M$. This time shift can easily be understood. In the non-linear least squares fit we are ignoring the imaginary part of the waveform. Since the real and imaginary parts of the waveforms are essentially time-shifted copies of each other, this produces a constant dephasing in the predicted physical parameters of the final black hole.

In the absence of numerical errors and mode coupling $j(t_0)$ should monotonically decrease, approaching a constant as $t_0 \to \infty$. Fig. 16 clearly shows that this is not the case. All fitting routines consistently predict non-trivial time variations (roughly of order a percent) in j. Increasing the resolution reduces the amplitude of these variations, and produces a flattening of $j(t_0)$ for $40 \lesssim t_0/M \lesssim 60$. The angular momentum increase that can be seen for $q = 1.5$ and $(t_0 - t_{\rm peak}) \gtrsim 45M$, and the oscillations in j for $q = 3.0$ in the same time range, are clearly artifacts of insufficient resolution. We tried to perform a Richardson extrapolation of the results assuming second-order and fourth-order convergence, to determine if angular momentum oscillations (which could be a sign of "new" physics) disappear in the limit of infinite resolution. Our results are shown in Fig. 17. They are compatible with the possibility that oscillations

disappear in the limit of infinite resolution, but more simulations and better control of the errors are required to reach a firm conclusion.

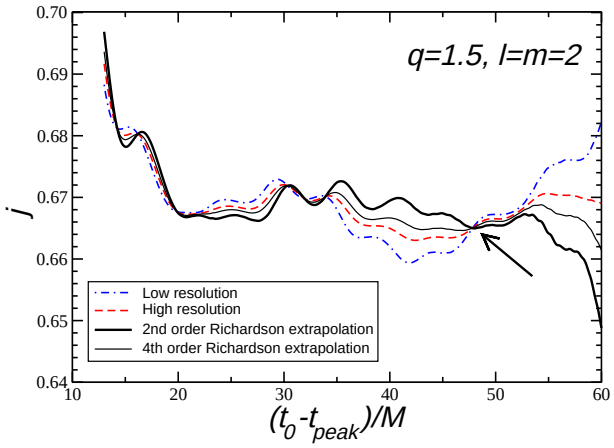

FIG. 17: Richardson extrapolation of the estimated angular momentum for $l = m = 2$ and $q = 1.5$, assuming second-order (thick line) and fourth-order (thin line) convergence.

Fig. 16 clearly illustrates that resolution plays a role in the accuracy with which we can estimate black hole parameters from ringdown fits, especially at late times, when the signal is very weak and affected by numerical noise (likely caused by reflections off refinement and outer boundaries). Fortunately, changing the extraction radius does *not* affect the quality of the fits. We checked this by fitting the $l = m = 2$ and $l = m = 4$ modes for equal mass ($q = 1$), large separation (D10) binary mergers with different extraction radii $r_{\rm ext} = 30,\ 40$ and 50. The functional form of $j(t_0)$ is exactly the same at different extraction radii. Changing $r_{\rm ext}$ only produces a trivial shift of the time axis by $\Delta t_0 \simeq \Delta r_{\rm ext}$, due to the finite propagation speed of the waves.

Estimates of the angular momentum as a function of t_0, obtained by fitting the dominant mode ($l = m = 2$) for different values of q, are shown in Fig. 18. The angular momentum is constant within about $\sim 1\%$, but the quality of the estimates rapidly degrades with mass ratio. Even with high-resolution runs, the estimated angular momenta have errors $\sim 10\%$ for $q \gtrsim 3$. In the next Section we will show that improved estimates are possible if we *cross-correlate* information from different multipoles of the radiation, making use of the no-hair theorem of general relativity.

C. Cross-correlating information from different multipoles to determine the black hole parameters

We already pointed out that the quality factor of each QNM Q_{lmn}, being dimensionless, must be a function of j only; and for the dominant modes ($l = m = 2,\ 3,\ 4$) this function is monotonically increasing, so we can easily invert $Q_{lmn}(j)$ to compute $j(t_0)$ by using fitting relations or by interpolating QNM tables [33]. If linear perturbation theory were an *exact* description of the final black hole's dynamics, the value of the angular momentum obtained from different QNMs – that is, from different values of $(l,\ m,\ n)$ – should be the same for all modes and all values of t_0. In practice this is only approximately true. First of all, non-linear effects should be present close to merger, so that linear perturbation theory provides only an approximation to the "true" oscillation frequencies (if the definition of QNMs makes sense at all in the non-linear regime). Secondly, rotational mode mixing, induced by the use of spin-weighted spherical harmonics with some given given $(l\,, m)$ rather than spin-weighted *spheroidal* harmonics, will produce additional QNM frequencies[8] with different l's and the same m. Finally, numerical error and the omission of overtones will inevitably produce some bias in the estimation of the frequencies, whatever fitting routine we use to extract them.

[8] Mode mixing was actually observed by BCP: when fitting the $l = 3$, $m = 2$ waveform they also found the $l = m = 2$ QNM frequency. However, they did not explain the appearance of the additional mode as rotational coupling: see the discussion around Eq. (44) in BCP. More details on rotational mode mixing are given in Fig. 7 and Eq. (23) of [16].

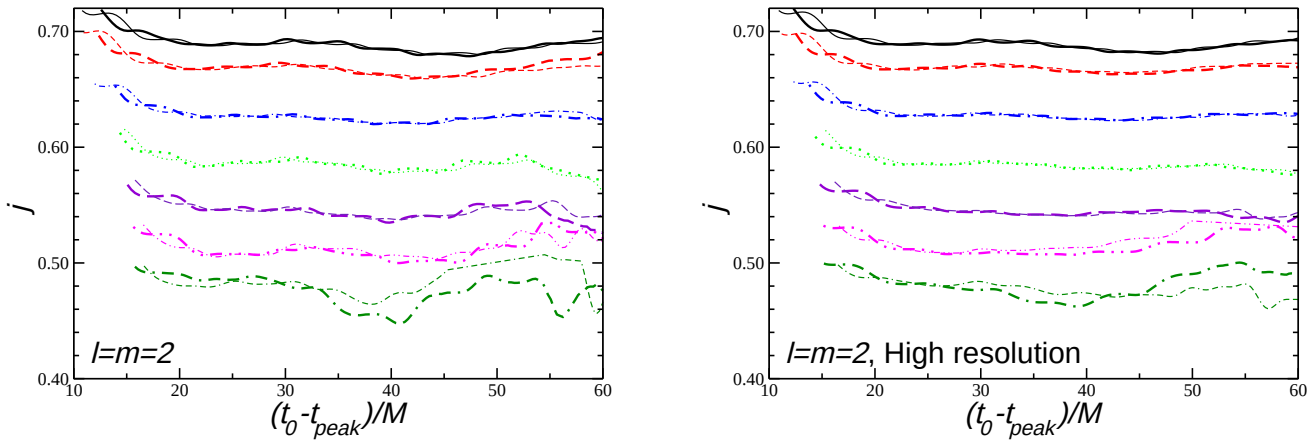

FIG. 18: Angular momentum estimated applying the MP method (thick lines) and the LM method (thin lines) to the $l = m = 2$ waveforms. Lines from top to bottom refer to different mass ratios: $q = 1.0,\ 1.5,\ 2.0,\ 2.5,\ 3.0,\ 3.5,\ 4.0$.

All of these effects should be reasonably small, especially at late times, since linear perturbation theory can be expected to be a good approximation once the final black hole is "reasonably close" to a Kerr state (where "reasonably close" is here a loosely defined concept that can be made more precise, for example, through the use of quantities such as the "speciality index" S [38]). Conversely, if we estimate angular momenta by fitting different multipolar components of the radiation, we can determine when perturbation theory is a good description of the system by looking for points (or intervals) in time when the angular momenta obtained from different fits agree with each other.

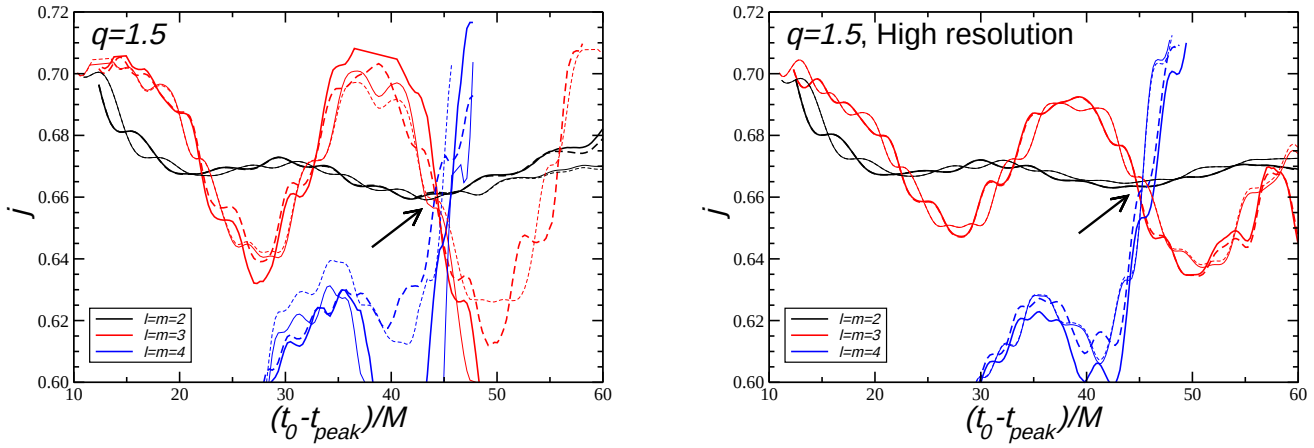

FIG. 19: Consistency in the radiated angular momentum, as predicted by different multipoles, for a $q = 1.5$, D7 run. Thick lines use the MP method, thin lines use the LM method. Solid lines are obtained by removing all points for which the absolute amplitude drops below 10^{-4}, and dashed lines by removing all points for which the relative amplitude drops below 10^{-3} the peak value. The choice of fitting method and truncation criterion has negligible influence on the results. Arrows mark the last point in time when the fit can still be considered reliable, *and* different multipoles agree with linear perturbation theory of Kerr black holes.

In Fig. 19 we plot the angular momenta estimated by fitting the dominant multipolar components of the radiation emitted in a $q = 1.5$, D7 merger. Angular momenta from $l = m = 2$ and $l = m = 3$ are generally in good agreement,

but they display oscillations around some mean value. The magnitude of the oscillations is larger for $l = 3$, and it also gets larger for coarse resolutions. However, there are discrete points in time when the angular momenta predicted by different multipolar components agree with each other.

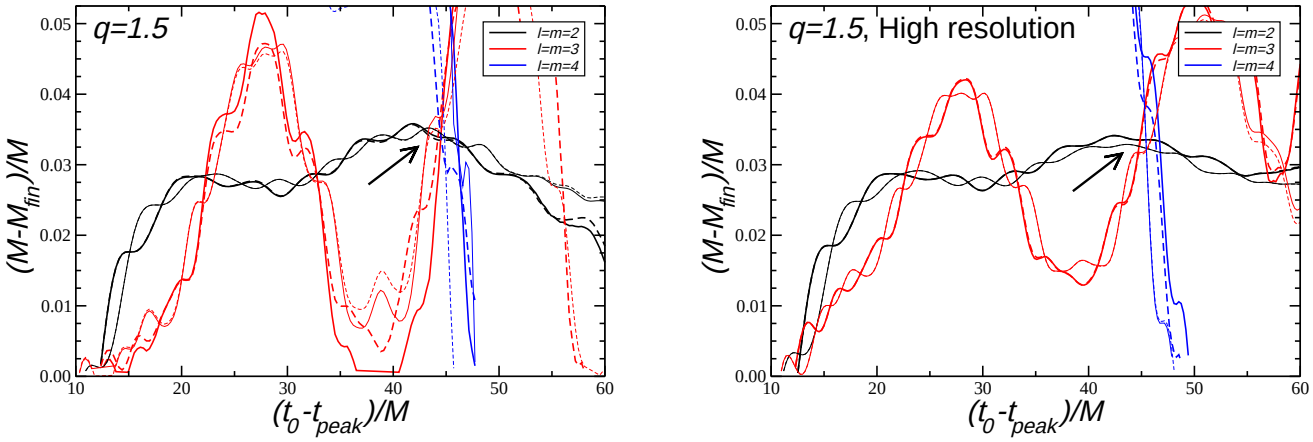

FIG. 20: Consistency in the energy radiated, as predicted by different multipoles, for a $q = 1.5$, D7 run. Linestyles are the same as in Fig. 19.

In Fig. 20 we use QNM fits of different multipoles to extract the final black hole mass $M_{\rm fin}$. From $M_{\rm fin}$ we can estimate the radiated energy as a function of t_0 by computing $(M - M_{\rm fin})/M$. The plots provide a remarkable consistency check of the results in Fig. 19: whenever results from numerical relativity are in agreement with linear black hole perturbation theory for the angular momentum, *they are also in agreement for the radiated energy*. In other words: when angular momenta from $l = m = 2$ and $l = m = 3$ agree, also the masses do. In our opinion this result is non-trivial, and it lends support to choosing this "perturbation theory time" (marked by arrows in the plots) as our best guess to estimate the final black hole's parameters.

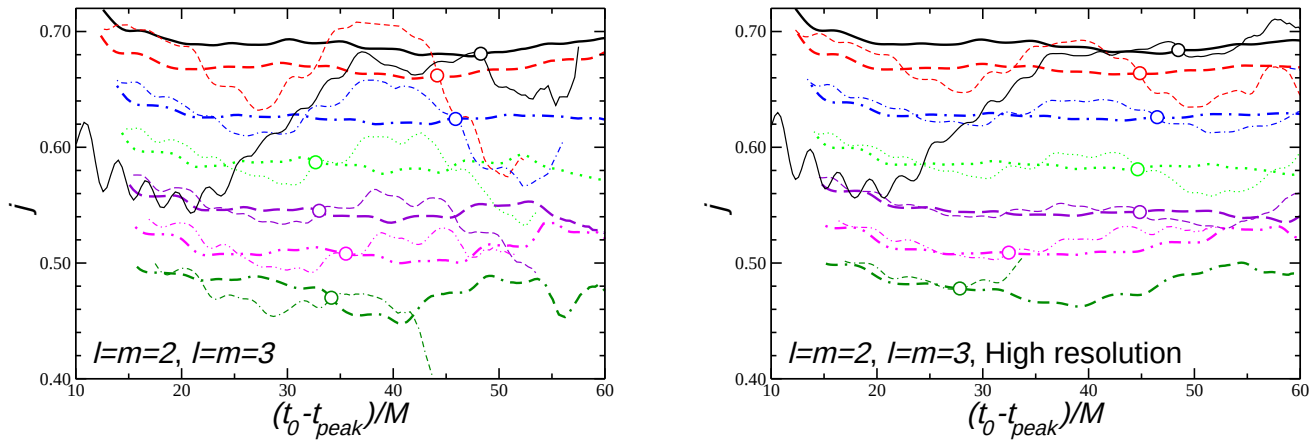

FIG. 21: Angular momentum estimated applying the method to $l = m = 2$ waveforms (thick lines) and to $l = m = 3$ ($l = m = 4$ in the case $q = 1.0$) waveforms (thin lines). Hollow circles mark the "perturbation theory time" for each mass ratio (see text). From top to bottom, different linestyles refer to $q = 1.0,\ 1.5,\ 2.0,\ 2.5,\ 3.0,\ 3.5$ and 4.0, respectively.

In Fig. 21 we compare the performance of our two "best" fitting methods (MP and LM) in estimating angular momenta for different mass ratios: $q = 1.0,\ 1.5,\ 2.0,\ 2.5,\ 3.0,\ 3.5,\ 4.0$. Deviations between the two methods can

be significant, especially for large mass ratio, when the numerical simulations are less reliable. For $q = 4.0$ and low resolution, the LM method shows periodic variations in j that are not visible using the MP method. This could be an effect of the larger bias in frequency of the LM method, as compared with the MP method. Once again, increasing the resolution produces a flattening of all curves, the effect being more pronounced for large mass ratios. Remarkably, we find that the angular momenta and masses predicted from fitting different multipolar components agree at a well-specified time *for all mass ratios*.

TABLE V: Energy radiated $\Delta E_{\rm QNM}/M$ and final dimensionless angular momentum $j_{\rm QNM}$ as computed by a QNM fit of high-resolution D7 runs. We use the "absolute" cutoff criterion for the fits. Results are presented using two fitting methods: MP and LM (the latter results are in parentheses). For ease of comparison, we also give the energy radiated as computed by wave extraction techniques. We denote by $t_{\rm PT}$ the "perturbation theory time" when the $l = m = 2$ and $l = m = 3$ predictions for mass and angular momentum are in agreement (values in parenthesis refer to low resolution runs). For comparison we also show estimates of the radiated energy $\Delta E_{\rm tot}/M$ and of the final angular momentum $j_{\rm fin}$ obtained by subtracting the radiated energy and angular momentum from the initial ADM mass and angular momentum.

q	$\Delta E_{\rm tot}/M(\%)$		$\Delta E_{\rm QNM}/M(\%)$		$j_{\rm fin}$		$j_{\rm QNM}$		$t_{\rm PT}/M$
	HR	LR	HR	LR	HR	LR	HR	LR	
1.0	3.718	3.673	3.73	3.90	0.688	0.689	0.684	0.680	282.5
			(3.65)	(3.88)			(0.684)	(0.681)	(284.0)
1.5	3.403	3.382	3.35	3.35	0.665	0.665	0.664	0.662	281.2
			(3.23)	(3.50)			(0.665)	(0.660)	(281.8)
2.0	2.858	2.822	2.69	2.77	0.626	0.628	0.626	0.623	281.9
			(2.66)	(2.63)			(0.626)	(0.625)	(284.5)
2.5	2.383	2.350	2.43	2.07	0.583	0.585	0.581	0.587	282.7
			(2.36)	(2.12)			(0.581)	(0.586)	(284.0)
3.0	2.000	1.977	1.97	1.97	0.543	0.544	0.544	0.544	284.6
			(2.06)	(2.07)			(0.543)	(0.545)	(285.8)
3.5	1.695	1.672	1.63	1.67	0.506	0.508	0.509	0.508	275.0
			(1.47)	(1.46)			(0.512)	(0.512)	(278.2)
4.0	1.451	1.429	1.3	1.93	0.473	0.478	0.478	0.469	272.6
			(1.5)	(1.14)			(0.473)	(0.481)	(290.0)

When different multipolar orders are consistent with a single, linearly perturbed Kerr black hole, numerical waveforms exactly match the perturbative predictions. The latest of these points in time is our "best guess" to estimate the parameters of the final black hole, since by then the background dynamical spacetime is as close as possible to a stationary Kerr solution. In Table V we list the final angular momenta and radiated energy extracted from a QNM fit at this "optimal" time, comparing results against the corresponding estimates from wave extraction techniques. The agreement is extremely good, and it only gets slightly worse for relatively large mass ratios ($q \gtrsim 3.0$). For each value of q, deviations between wave extraction methods and QNM fits can be expected to provide a good error estimate on the final angular momentum and on the radiated energy.

D. Criteria to determine the ringdown starting time

There are important motivations to try and define the ringdown starting time and to isolate, in a non-ambiguous way, the energy radiated in the ringdown phase. For instance, from a detection-based point of view, the SNR of a ringdown signal scales with the square root of the energy in the signal [33, 39]. To define the energy in ringdown waves we must somehow define the ringdown starting time. Being able to define the ringdown starting time is also important when comparing numerical simulations with PN estimates of the energy, angular and linear momentum. In fact, it has been suggested that the discrepancy between PN estimates and numerical results for black hole recoil is due to neglecting the ringdown in the former [3]. To check the validity of this statement we must, again, define the starting time of the ringdown phase.

Unfortunately, early studies in quasinormal ringing have established that there is no such thing as "the" ringdown starting time (see eg. [36] and references therein). In fact, the waveform can *never* be exactly described as a pure superposition of damped sinusoids: it is always contaminated by noise or by other contributions (eg. prompt response or tails). This is essentially a consequence of the incompleteness of QNMs. However, from a practical viewpoint the signal *is* indeed dominated by ringdown at some stage, and this is the reason why we can use ringdown waves to estimate black hole parameters [33]. The time span of the ringdown phase can be defined in different ways, depending on context. In the following we will discuss and implement three possible alternatives, two of which have already been proposed in the past [16, 17].

1. A least-squares approach

A natural way to determine the QNM content of a given signal would be to perform a non-linear fit of the data to an exponentially decaying sinusoid. Here the unknown parameters are usually found in a least-squares sense, by minimizing some functional of the form $\sum_{t=t_i}\left(h(t)-h^{qnm}(t,\{\lambda\})\right)^2$. In our specific case h would be the numerical data, sampled at instants $t=t_i$, and $h^{qnm}(t,\{\lambda\})$ is the model waveform (an exponentially damped sinusoid).

The model depends on a set of unknown parameters $\{\lambda\}$ over which the functional should be minimized. It is of course very tempting to treat the starting time as one of those parameters. This is a possible way to determine the ringdown starting time, and it served as the basis for the proposal in [16]. There it was shown that the quality of a QNM fit can be monitored by using some suitably defined norm. In particular, Ref. [16] proposed to use

$$||N||(\tau_0)=\frac{\int_{\tau_0}^{t_f}|\psi_{l\,,m}(t)-\psi_{\rm fit}^{l\,,m}|dt}{\int_{\tau_0}^{t_f}|\psi_{l\,,m}(t)|dt}\,, \tag{4.3}$$

where $\psi_{\rm fit}^{l\,,m}$ has been defined in Eq. (4.1). Clearly $||N||\to 0$ when the fit is very close to the numerical waveform. The idea is that the norm should have a local minimum when the "trial" starting time τ_0 tends to the "true" starting time, $\tau_0\to t_0$.

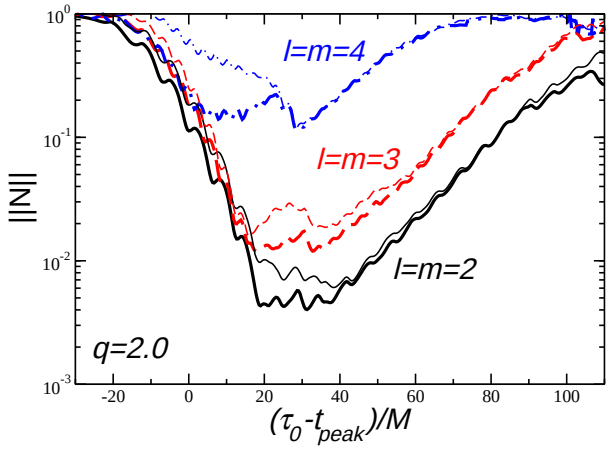

FIG. 22: Norm (4.3) as a function of the trial starting time for the dominant components $(l,\ m)=(2,\ 2),\ (3,\ 3),\ (4,\ 4)$ in a merger with $q=2.0$ (we consider a D7 run here). Thick lines are obtained by fitting the frequency each time we change τ_0. Thin lines use the following fixed values for the QNM frequency: $M\omega_R=0.51677$, $M\omega_I=0.08586$ for $l=m=2$, $M\omega_R=0.82210$, $M\omega_I=0.08571$ for $l=m=3$, $M\omega_R=1.12152$, $M\omega_I=0.08577$ for $l=m=4$.

This idea works well for the classical perturbation theory problem of Gaussian pulses scattered off a Kerr background [16], but unfortunately it does not provide a very clear answer when tested on binary black hole merger waveforms. The norm $||N||(\tau_0)$ for a binary with $q=2.0$ is shown in Fig. 22, where it is computed in two slightly different ways. The simplest way treats the QNM frequencies as known: their values can be obtained once and for all by using Prony methods or non-linear fits [15], and kept fixed as we change τ_0. The second method achieves a marginal reduction of the norm by fitting for the QNM frequency at each starting time τ_0.

From Fig. 22 we see that the norm has some of the desired properties. First of all, it grows as the quality of the QNM fit degrades: for example, it is larger for the subdominant $(l,\ m)$ components. In addition the norm grows, as it should, when we try to extend the fit to encompass the merger region, i.e. when $(\tau_0-t_{\rm peak})\lesssim 10$.

We find that the functional (4.3) has a minimum for most, but not all of the waveforms. Even when it does have a minimum (as in the case of Fig. 22) this minimum is very broad. In addition the norm oscillates with a period which is basically the QNM period, and it has a series of local minima and maxima. The broad minimum and the oscillations make it very hard to locate the starting time. Of course, the functional (4.3) is by no means the only possibility. We experimented with some alternative functional forms of the norm, but with no success. On a positive note, the situation seems to improve when the waveform is computed at large extraction radii [40].

2. Nollert's Energy Maximized Orthogonal Projection (EMOP)

A physically motivated notion of ringdown starting time time was introduced by Nollert [17]. He realized that the problems with defining the starting time arise immediately at the onset: QNMs are not complete and not orthogonal with respect to any inner product, so a quantification of the energy (and therefore of the starting time) going into each mode, using standard "basis expansion" methods, is difficult (if not impossible). The lack of orthogonality can be circumvented by formally defining an orthogonal decomposition of the waveform into the contribution of one (or more) QNMs, and some orthogonal remainder [17]:

$$h = h_{\parallel} + h_{\perp}\,. \tag{4.4}$$

Here, $h_{\parallel}$ and $h_{\perp}$ are the part of h parallel and perpendicular, respectively, to a given QNM or a finite number p of QNMs. We therefore write

$$h_{\parallel} = \sum_{i=1}^{p} a_{\parallel}^{(i)} h_{\rm QNM}^{(i)}\,, \tag{4.5}$$

where

$$h_{\rm QNM}^{(i)} = \begin{cases} 0 & \text{if } t < t_0 \\ e^{-\omega_i t}\sin\left(\omega_r t + \phi\right) & \text{if } t > t_0\,. \end{cases} \tag{4.6}$$

is the QNM, assumed to start at some time t_0. The decomposition is achieved using a standard orthogonal projection

$$\langle h_{\parallel}, h_{\perp}\rangle = 0\,, \tag{4.7}$$

where the inner product, following arguments by Nollert [17], is defined in an energy-oriented way:

$$\langle \Psi, \Phi\rangle = \int \dot{\Psi}^{*}\dot{\Phi} dt\,. \tag{4.8}$$

One can show that the energy "parallel to the QNM component of the signal" is given by

$$E_{\parallel} = \left|\int \dot{h}_{\rm QNM}^{(i)*}\dot{h} dt\right|^2 \left[\int \dot{h}_{\rm QNM}^{(i)*}\dot{h}_{\rm QNM}^{(i)} dt\right]^{-1}\,. \tag{4.9}$$

It is now meaningful to talk about (say) "the fraction of energy going into the first QNM". This fraction obviously depends on the starting time t_0 in Eq. (4.6). Nollert observes that the ratio of the energy "parallel to the QNM component" to the total energy in the signal, $E_{\parallel}/E_{\rm tot}$, has a maximum as a function of t_0. We can define the ringdown starting time as the time t_0 corresponding to this *Energy Maximized Orthogonal Projection* (EMOP). In other words, according to Nollert's criterion, the ringdown starting time $t_0 = t_{\rm EMOP}$ is chosen by looking for[9]

$$\max_{t_0\,,\phi}\frac{E_{\parallel}}{E_{\rm tot}} = \max_{t_0\,,\phi}\left(\left|\int \dot{h}_{\rm QNM}^{(i)*}\dot{h} dt\right|^2 \left[\int \dot{h}_{\rm QNM}^{(i)*}\dot{h}_{\rm QNM}^{(i)} dt\right]^{-1} \times \left[\int \dot{h}^{*}\dot{h} dt\right]^{-1}\right) \tag{4.10}$$

The previous integral is evaluated separately for each polarization component. To avoid memory effects, when we integrate Ψ_4 we fix the integration constant so that $\dot{h} = 0$ at the end of the simulation. We denote by $E_{\rm EMOP}$ the maximized energy parallel to the QNM component of the signal:

$$E_{\rm EMOP} \equiv E_{\parallel}(t_0 = t_{\rm EMOP})\,. \tag{4.11}$$

Using Prony methods or non-linear fits [15] we first determine the QNM frequency and the damping time (for simplicity we consider a single QNM). Then we compute $t_{\rm EMOP}$ and $E_{\rm EMOP}$ by maximizing (4.10) over both t_0 and ϕ.

---

[9] Another conceivable definition would not use the total energy in the waveform $E_{\rm tot}$, but the energy in the waveform for $t > t_0$. It turns out that this quantity does not have a well-defined maximum. It is also possible to use a variable frequency in (4.10), in which case one could possibly obtain a larger maximum. This method would be equivalent to matched filtering, which is discussed below.

TABLE VI: Data for EMOP, for $l = 2$. Numbers separated by a comma correspond to the + and × polarizations, respectively. The fraction of the total energy in the $l = 2$ mode is about 42% for all mass ratios. We find that, independently of mass ratio, the value of $t_{\rm EMOP}$ for a given polarization is generally at a fixed position relative to the maximum of the waveform's amplitude $t_{\rm peak}$. We measure this relative difference by $\Delta t_{\rm EMOP} \equiv t_{\rm peak} - t_{\rm EMOP}$, which turns out to be roughly independent of q.

q	run	$\frac{E_{\rm EMOP}}{E_T}$	$\frac{\langle t_{\rm EMOP}\rangle}{M}$	$\frac{\Delta t_{\rm EMOP}}{M}$	$\frac{\langle \Delta t_{\rm EMOP}\rangle}{M}$	$\frac{10^2 E_{\rm EMOP}}{M}$	$\frac{\langle 10^2 E_{\rm EMOP}\rangle}{M}$
1.0	D7	0.41, 0.42	225.5	10.0, 7.0	8.5	1.9, 1.7	1.8
1.5	D7	0.41, 0.43	227.2	10.8, 7.4	9.1	1.8, 1.5	1.6
2.0	D7	0.42, 0.42	227.0	9.9, 6.9	8.4	1.4, 1.2	1.3
2.5	D7	0.41, 0.43	229.2	10.6, 7.1	8.8	1.2, 0.98	1.1
3.0	D7	0.41, 0.43	230.2	11.2, 7.8	9.5	0.95, 0.82	0.88
3.5	D7	0.40, 0.43	232.0	12.5, 8.5	10.5	0.80, 0.69	0.75
4.0	D7	0.39, 0.42	233.5	13.3, 9.3	11.3	0.68, 0.59	0.64
2.0	D8	0.40, 0.41	453.0	10.6, 6.6	8.6	1.4, 1.2	1.3
3.0	D8	0.40, 0.41	408.8	11.0, 7.6	9.3	0.95, 0.81	0.88

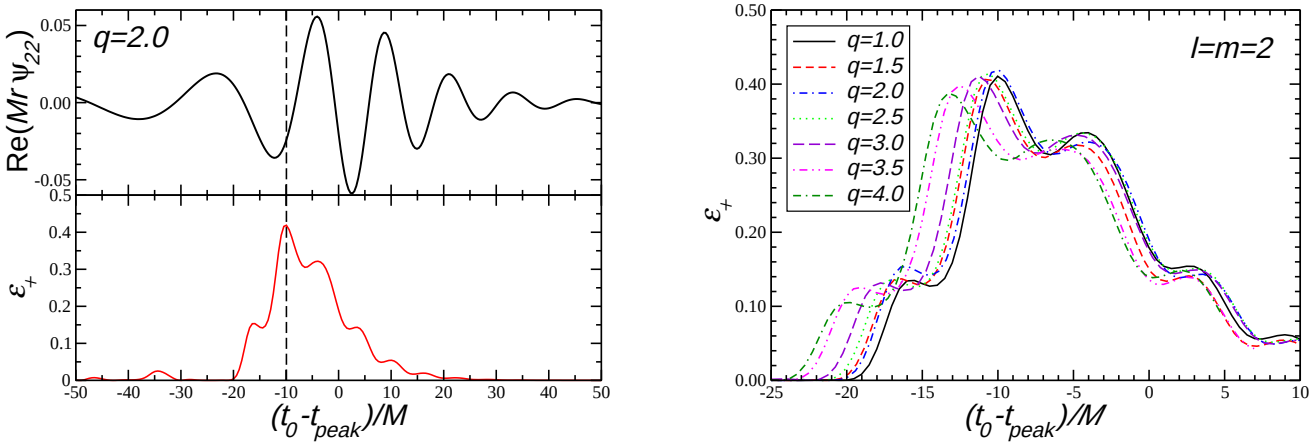

FIG. 23: EMOP for $l = 2$ computed using run D7 (and high resolution). In the left panel we overplot ϵ_+ and the actual waveform, marking $t_{\rm EMOP}$ by a vertical dashed line. In the right panel we show that results are quite insensitive to q: each line corresponds to a different mass ratio, and linestyles are the same as in Fig. 21.

Our results for $l = m = 2$ and run D7 are presented in Table VI and Fig. 23. In the plots, $\epsilon_{+,\times}$ is the fraction of energy radiated at $t > t_0$ in each of the two polarization components, normalized to the total energy radiated in the simulation, and computed for the value of the phase maximizing the EMOP. The first thing to notice is that there is a sharp maximum of the fractional energy going into ringdown. As seen from Fig. 23, $\sim 42\%$ of the total energy in the $l = 2$ merger waveform goes into ringdown. The results differ (very) slightly depending on the chosen polarization state.

In Table VI we measure the ringdown starting time $t_{\rm EMOP}$ relative to the peak in $|Mr\psi_{22}|$, i.e., we compute $\Delta t_{\rm EMOP} \equiv t_{\rm peak} - t_{\rm EMOP}$. We see that $\Delta t_{\rm EMOP}$ is basically constant for all mass ratios *and for all runs*, corresponding to different initial separation of the binary. This is an important convergence test on the results. Notice also that $t_{\rm EMOP}$ is located *before* the peak location.

EMOP times for the two polarizations are displaced by about $3M$ for run D7. To define a unique ringdown starting time we take the average of both polarizations (in Table VI, an average over the two polarizations is denoted by angular brackets). Using this average starting time we can define an energy radiated in ringdown, also shown in Table VI. We find the following formula to be a good fit for the energy in the $l = 2$ mode:

$$\frac{E_{\rm EMOP}}{M} = 0.271 \frac{q^2}{(1+q)^4}\,, \quad l = 2\,. \tag{4.12}$$

Results for $l = 3$ follow the same pattern (see Table VII). The average $\langle t_{\rm EMOP}\rangle$ for $l = 3$ is located about $6M - 7M$

TABLE VII: EMOP data for $l = 3$. In this Table, by "peak" we mean the peak in the amplitude of the $l = 3$ mode. Numbers separated by a comma correspond to the + and × polarizations, respectively. The fraction of the total energy in the $l = 3$ mode is about 44% for all mass ratios.

q	run	$\frac{E_{\rm EMOP}}{E_T}$	$\frac{\langle t_{\rm EMOP}\rangle}{M}$	$\frac{\Delta t_{\rm EMOP}}{M}$	$\frac{\langle \Delta t_{\rm EMOP}\rangle}{M}$	$\frac{10^4 E_{\rm EMOP}}{M}$	$\frac{\langle 10^4 E_{\rm EMOP}\rangle}{M}$
1.5	D7	0.44, 0.45	233.0	4.4, 6.4	5.4	3.5, 3.9	3.7
2.0	D7	0.45, 0.45	230.5	7.4, 5.4	6.4	7.7, 6.9	7.3
2.5	D7	0.44, 0.45	232.5	8.2, 6.2	7.2	9.6, 8.6	9.1
3.0	D7	0.44, 0.45	234.0	8.4, 6.4	7.4	10, 9.1	9.6
3.5	D7	0.43, 0.45	238.2	4.8, 7.3	6.0	7.8, 9.2	8.5
4.0	D7	0.43, 0.45	240.2	4.8, 7.3	6.0	7.5, 8.8	8.1
2.0	D8	0.44, 0.45	456.5	7.1, 5.1	6.1	7.6, 6.8	7.2
3.0	D8	0.45, 0.44	412.7	4.8, 7.3	6.1	8.8, 10	9.4

after the average $\langle t_{\rm EMOP}\rangle$ for $l = 2$. The following formula provides a good fit for the energy in the $l = 3$ mode:

$$\frac{E_{\rm EMOP}}{M} = 0.104\frac{q^2(q-1)^2}{(1+q)^6}\,, \quad l = 3\,. \tag{4.13}$$

If we take $t_{\rm EMOP}$ for $l = 2$ as the fiducial ringdown starting time, we can compute the energy, angular and linear momentum radiated during the ringdown phase (as described by the EMOP). The results of this calculation are listed in Table I, and fitting formulas are provided in Appendix B (see in particular Table XII).

3. A detection-based approach: energy deposited in matched filters

As we already stated QNMs do not form a complete set, so the signal will always comprise quasinormal ringing plus some other component (such as prompt response or tails). However, in most practical applications we are only interested in some "fairly good approximation" to the ringdown waveform. The notion of "fairly good" must be defined according to the specific context.

A possible definition, based on theoretical considerations, was introduced in the previous Section. Here we propose an alternative, practical definition of the ringdown phase from a detection perspective. Detection of ringdown waves is likely to be achieved through matched filtering [33, 39]. The technique works by cross-correlating the detector's output against a set of theoretical templates. It can be shown that the maximum SNR is achieved when the template is equal in form to the detector's output (hence the name matched filtering). Matched filtering is the method of choice to search for ringdown waves: it is quasi-optimal and inexpensive, in the sense that it achieves the maximum SNR with a relatively small number of templates or filters.

Now, for the purpose of a matched filtering detection, the ringdown definition *must* be related to the use of ringdown templates. The relevant question is therefore: what is the maximum SNR attainable through the use of a filter which is a pure damped sinusoid? By definition, given the numerical waveform $h(t)$, the SNR ρ is

$$\rho = \max_{\{\lambda\},t_0} \frac{(T(\{\lambda\},t_0)|h)}{\sqrt{(T(\{\lambda\},t_0)|T(\{\lambda\},t_0)}}\,, \quad (h_1|h_2) \equiv 2\int_0^\infty \frac{h_1^*(f)h_2(f) + h_1(f)h_2^*(f)}{S_h(f)}\,, \tag{4.14}$$

where the template $T(\{\lambda\},t_0)$ is

$$T(\{\lambda\},t_0) = \begin{cases} e^{-\omega_i^T(t-t_0)}\sin(\omega_r^T t + \phi^T)\,, & \text{if } t \geq t_0\,, \\ 0 & \text{if } t < t_0\,. \end{cases} \tag{4.15}$$

$S_h(f)$ is the noise spectral density of the detector and $\{\lambda\}$ is a set of parameters characterizing the templates. The procedure is now simple: we "slide" this template backwards (starting at large t_0 and decreasing it progressively) across the numerical waveforms, and determine the maximum of the convolution (4.14). A good initial guess for the template parameters $(\omega_i^T, \omega_r^T, \phi^T)$ can be obtained with Prony methods [15].

As expected t_0 will depend on the observer, i.e., on the detector being used, through the noise spectral density $S_h(f)$. In practice, however, the dependence on the detector is usually very weak, since in general the largest contribution to the convolution integral is near the resonant frequency ω_r. Thus, for all practical purposes, the detectors behave as if the noise were white: the spectral density $S_h(f)$ can be approximated as constant and moved out of the integral. This assumption also allows one to sidestep the computation of the Fourier transform of the waveforms: by Parseval's

theorem, the frequency integral can be turned into a time integral. A more complete analysis, taking into account the full structure of the detector's noise, is in preparation.

A possible notion of effective ringdown starting time $t_{\rm MF}$ according to a matched filter, which is useful to make contact with previous SNR calculations [33], can be given simply as follows[10]. Define the effective starting time $t_{\rm MF}$ as the instant for which

$$\rho = \sqrt{(h_{t_{\rm MF}}|h_{t_{\rm MF}})}\,, \qquad h_{t_{\rm MF}} \equiv \begin{cases} T(\{\lambda\},t) & \text{if } t \geq t_{\rm MF}\,, \\ 0 & \text{if } t < t_{\rm MF}\,, \end{cases} \tag{4.16}$$

where ρ is computed from Eq. (4.14). Notice that, in general, $t_{\rm MF}$ does *not* coincide with the instant at which the convolution between the signal and the template has a maximum. By using Eq. (4.16) the SNR can be expressed in terms of energy in the actual signal. This is a common approach in engineering, introduced in the context of gravitational wave detection by Flanagan and Hughes [39] (see also [33]).

TABLE VIII: Estimated, polarization-averaged effective starting times t_{MF} and energy radiated in ringdown from a matched-filter detection perspective, as functions of mass ratio. The listed energies should be taken as rough estimates with a 10% uncertainty, depending on the number of filters one is willing (and able) to use. We list also $\Delta t_{\rm MF}$, which is the "effective" starting time as measure from the peak of the $l = m = 2$ waveform: $\Delta t_{\rm MF} \equiv t_{\rm peak} - t_{\rm MF}$.

q	$\langle t_{\rm MF}/M\rangle$	$\langle \Delta t_{\rm MF}/M\rangle$	$\langle E_{\rm MF}/M\rangle$
1.0	207	27.0	0.028
1.5	208	28.4	0.026
2.0	209	26.4	0.021
2.5	209	29.1	0.018
3.0	210	29.8	0.015
3.5	211	31.5	0.012
4.0	212	32.8	0.011

The detection-based criterion, when applied to the merger waveforms considered in this paper, yields the results shown in Table VIII. From the above discussion, it is clear that the values we list for the energy radiated during ringdown are effective energies measured by the detector. These correspond to the values used in data analysis (see for instance [33]). From the Table we see that the effective energy radiated in ringdown for an equal mass merger is $\sim 3\%$, in very good agreement with the "guesstimate" by Flanagan and Hughes [39], which has often been used in the literature to compute SNRs and measurement errors. We also note that this value is much larger than the energy estimated by the EMOP, typically twice as large. This happens because the filter is looking for the maximum correlation, usually implying that the best-match parameters (ω_r and ω_i) will differ significantly from the true signal parameters.

Also notice that different polarizations yield slightly different energies and starting times. For instance, for equal mass mergers, we get $t_{\rm MF} \sim 205$ and $t_{\rm MF} \sim 208$ for the plus and cross polarizations, respectively. If we average over polarization states, this yields an effective radiated energy of $\sim 2.8\%$, with an uncertainty of less than 10%. Given that the SNR scales with the square root of the energy, this uncertainty is not important.

We also point out that the amount of energy depends on the parameter space to be searched. In principle, the correlation (4.14) is to be maximized over all possible values of $\omega_r\,, \omega_i$. In practice however, this would lead to an infinite number of filters, so we must choose reasonable cutoffs. For instance, in black hole ringdown searches one looks for modes with a quality factor typically smaller than ~ 20. It may be possible to increase the SNR and the amount of effective energy in ringdown by enlarging the parameter search (this would also allow us to search for ringdown modes of other objects, such as neutron stars or boson stars). A discussion of these issues will be presented elsewhere.

To conclude this Section, we point out that a fit of the total effective energy radiated in ringdown, according to a matched filtering criterion, is:

$$\frac{\Delta E_{\rm MF}}{M} \approx 0.44 \frac{q^2}{(1+q)^4}\,. \tag{4.17}$$

[10] Nollert's "theoretical" definition, explained in the previous Section, is not too dissimilar from a "detection-oriented" definition. Indeed, expression (139) in [17] can be interpreted as the fitting factor between actual waveforms and ringdown templates (for white noise). If we take the ringdown frequencies as unknown parameters and choose them to maximize the EMOP (4.10), the results we get are very close to the present matched-filtering criterion.

V. CONCLUSIONS AND OUTLOOK

The present study of binary black hole waveforms is, in many ways, only preliminary. The following is a partial list of important open problems.

Using "hybrid" waveforms in data analysis

The present study explored the physical properties of numerical waveforms and their relation with analytical methods. Our focus has been on providing analytical insight into the structure of the waveforms. For this reason, we deliberately avoided problems at the interface between numerical relativity and data analysis (see Ref. [41] for some steps in this direction). We strongly believe that an analytical understanding of the numerical simulations will be useful, or even *necessary*, to bridge the gap between the (daunting) numerical task of generating waveforms, and the injection of these waveforms into a data analysis pipeline.

The PNQC approximation studied in this paper provides a concrete example. We showed that the physical content of any given simulation can be reproduced quite accurately by substituting the orbital frequency Ω in the dominant waveform amplitudes, Eqs. (3.7). These "hybrid" PNQC waveforms can be used to create simple but accurate templates, and to interpolate between numerical waveforms with different physical parameters.

Despite the recent progress in numerical relativity, simulations are still computationally expensive. Hybrid template families could be injected in LIGO, or used in connection with LISA simulators in future rounds of the Mock LISA Data Challenges [42]. Semianalytical waveforms may significantly reduce the number of simulations needed for detection and parameter estimation, and they should be particularly useful when spins are included in the model.

Removing spurious eccentricity and including additional physical parameters

Our study clearly shows that the simulations have some small, but non-negligible, eccentricity. The eccentricity shows up as a typical modulation of all physical quantities of interest: the punctures' orbital velocity (Fig. 5), the binary's orbital frequency (Fig. 6), the energy and angular momentum fluxes (Figs. 13 and Fig. 15), and so on. Measuring this spurious eccentricity, and possibly removing it by fine-tuning initial data, is an important open problem [10, 24, 25]. Incidentally, the study of *truly* eccentric binaries could be relevant for massive black hole binaries to be observed by LISA [19].

In the present study we completely neglect spins. There is mounting evidence, based for example on recent studies of binary black hole recoil, that spins will have a dramatic effect on the inspiral-merger-ringdown transition. An extension of our study to spinning, precessing black hole binaries is urgently needed.

Stitching numerical and analytical waveforms

For reasons of space, we decided not to address the important problem of comparing the PN phase evolution with the numerical phase evolution. This problem is central to connect the early inspiral phase with the merger phase, and it is a topic of active investigation. Since numerical evolutions show signs of eccentricity, comparisons of the phase evolution may benefit from the inclusion of eccentricity in the PN models as well.

Another active research field concerns the problem of "stitching" PN and numerical waveforms. For the purpose of this stitching, do we need the full PN waveforms, or does the restricted PN approximation (including PN corrections in the phase, but not in the amplitude) work well enough? Does the number of cycles to be simulated numerically depend on the mass ratio and other physical parameters (eg. the spins)? We plan to return to these problems in the future.

Bridging the gap with black hole perturbation theory

Computational resources and resolution limitations reduce the accuracy of numerical simulations as the mass ratio q gets larger. Unfortunately, many astrophysical black hole binaries could have $q = 10$ or larger (see eg. [19] and references therein). It is important to determine the maximum value of q that *should* be simulated in numerical relativity, or equivalently, the smallest value of q for which black hole perturbation theory can be considered adequate for detection and/or parameter estimation. In Appendix C we collect some results that may be useful in this context.

Astrophysics and gravitational wave detection

The most interesting applications of our results should be in astrophysics and gravitational wave detection. For example, the multipolar analysis of the radiation performed in this paper can be used to determine the cosmological distance at which we can test the no-hair theorem with LISA, LIGO or Virgo. Future extensions of this analysis to spinning binaries could also predict the parameter range (mass ratio, spin magnitudes and directions) in which the recoil velocity is astrophysically relevant, and the probability for these regions of the parameter space to be populated in astrophysical scenarios.

Acknowledgments

We are particularly grateful to El-Hadi Djermoune for providing us with MATLAB codes implementing the matrix pencil and Kumaresan-Tufts algorithms. We thank Clifford Will for constant encouragement, and for computing the PN estimates of energy, angular momentum and linear momentum radiated after plunge shown in Figs. 24 and 25. We also thank John Baker, Luc Blanchet, Alessandra Buonanno, Jaime Cardoso, Greg Cook, Pablo Laguna, Deirdre Shoemaker and Manuel Tiglio for useful discussions. V. C. acknowledges financial support from CNPq - Conselho Nacional de Desenvolvimento Científico e Tecnológico through grant number 453463/2006-1. J. G. and U. S. acknowledge support from the ILIAS network. This work was supported in part by DFG grant SFB/Transregio 7 "Gravitational Wave Astronomy", by the National Science Foundation under grant number PHY 03-53180, and by NASA under grant number NNG06GI60 to Washington University. Numerical computations were performed at HLRS Stuttgart and LRZ Munich.

APPENDIX A: MULTIPOLAR DECOMPOSITION OF THE POST-NEWTONIAN WAVEFORMS

Here we list the spin-weighted spherical harmonic components of a PN expansion of the Weyl scalar Ψ_4. For $l = 2$ we have:

$$\begin{aligned} Mr\,\psi_{2\,,2}e^{i\tilde{\phi}} &= 32\sqrt{\frac{\pi}{5}}\eta(M\Omega)^{8/3}\left[1+\frac{55\eta-107}{42}(M\Omega)^{2/3}+2\pi(M\Omega)-\frac{2173+7483\eta-2047\eta^2}{1512}(M\Omega)^{4/3}\right. \\ &+ \left.\left(\frac{-107+34\eta}{21}\pi+\frac{168}{5}i\eta\right)(M\Omega)^{5/3}\right], \qquad \text{(A1a)} \\ Mr\,\psi_{2\,,1}e^{i\tilde{\phi}} &= -\frac{8}{3}\sqrt{\frac{\pi}{5}}\eta\frac{\delta M}{M}(M\Omega)^{3}\left[1+\frac{20\eta-17}{28}(M\Omega)^{2/3}+\frac{2\pi+i(1+\ln 16)}{2}M\Omega\right. \\ &+ \left.\left(-\frac{43}{126}-\frac{509}{126}\eta+\frac{79}{168}\eta^2\right)(M\Omega)^{4/3}\right]. \qquad \text{(A1b)} \end{aligned}$$

For $l = 3$:

$$\begin{aligned} Mr\,\psi_{3\,,3}e^{i\tilde{\phi}} &= -27\sqrt{\frac{6\pi}{7}}\eta\frac{\delta M}{M}(M\Omega)^{3}\left[1-(4-2\eta)(M\Omega)^{2/3}+\left[3\pi+i\left(\frac{21}{5}-6\ln(3/2)\right)\right]M\Omega\right. \\ &+ \left.\left(\frac{123}{110}-\frac{1838}{165}\eta+\frac{887}{330}\eta^2\right)(M\Omega)^{4/3}\right], \qquad \text{(A2a)} \\ Mr\,\psi_{3\,,2}e^{i\tilde{\phi}} &= \frac{32}{3}\sqrt{\frac{\pi}{7}}\eta(M\Omega)^{10/3}\left[(1-3\eta)-\frac{193-725\eta+365\eta^2}{90}(M\Omega)^{2/3}\right. \\ &+ \left.\left(3i+2\pi-\frac{6\eta}{5}(5\pi+11i)\right)M\Omega\right], \qquad \text{(A2b)} \\ Mr\,\psi_{3\,,1}e^{i\tilde{\phi}} &= -\frac{2}{3}\sqrt{\frac{\pi}{70}}\eta\frac{\delta M}{M}(M\Omega)^{3}\left[1-\frac{2(\eta+4)}{3}(M\Omega)^{2/3}+\frac{5\pi+i(7+10\ln 2)}{5}M\Omega\right. \\ &+ \left.\left(\frac{607}{198}-\frac{136}{99}\eta-\frac{247}{198}\eta^2\right)(M\Omega)^{4/3}\right], \qquad \text{(A2c)} \end{aligned}$$

For $l=4$:

$$Mr\,\psi_{4\,,4}e^{i\tilde{\phi}} = \frac{1024}{9}\sqrt{\frac{\pi}{7}}\eta(M\Omega)^{10/3}\left\{(1-3\eta)-\frac{1779-6365\eta+2625\eta^2}{330}(M\Omega)^{2/3}\right.$$
$$\left.+\left[4\pi+i\left(\frac{42}{5}-8\ln(2)\right)-\eta\left(12\pi+i\left(\frac{1193}{40}-24\ln(2)\right)\right)\right](M\Omega)\right\}, \tag{A3a}$$

$$Mr\,\psi_{4\,,3}e^{i\tilde{\phi}} = -\frac{162}{5}\sqrt{\frac{\pi}{14}}\eta\frac{\delta M}{M}(M\Omega)^{11/3}\left[(1-2\eta)+\left(-\frac{39}{11}+\frac{1267}{132}\eta-\frac{131}{33}\eta^2\right)(M\Omega)^{2/3}\right], \tag{A3b}$$

$$Mr\,\psi_{4\,,2}e^{i\tilde{\phi}} = \frac{32}{63}\sqrt{\pi}\eta(M\Omega)^{10/3}\left[(1-3\eta)-\frac{1311-4025\eta+285\eta^2}{330}(M\Omega)^{2/3}\right.$$
$$\left.+\left(\frac{21}{5}(1-4i\eta)+2\pi(1-3\eta)\right)M\Omega\right], \tag{A3c}$$

$$Mr\,\psi_{4\,,1}e^{i\tilde{\phi}} = -\frac{\sqrt{2\pi}}{105}\eta\frac{\delta M}{M}(M\Omega)^{11/3}\left[(1-2\eta)+\left(-\frac{101}{33}+\frac{337}{44}\eta-\frac{88}{33}\eta^2\right)(M\Omega)^{2/3}\right], \tag{A3d}$$

For $l=5$:

$$Mr\,\psi_{5\,,5}e^{i\tilde{\phi}} = -\frac{3125}{12}\sqrt{\frac{5\pi}{66}}\eta\frac{\delta M}{M}(M\Omega)^{11/3}\left[(1-2\eta)+\left(-\frac{263}{39}+\frac{688}{39}\eta-\frac{256}{39}\eta^2\right)(M\Omega)^{2/3}\right], \tag{A4a}$$

$$Mr\,\psi_{5\,,4}e^{i\tilde{\phi}} = \frac{4096}{45}\sqrt{\frac{\pi}{33}}\eta\left(1-5\eta+5\eta^2\right)(M\Omega)^4, \tag{A4b}$$

$$Mr\,\psi_{5\,,3}e^{i\tilde{\phi}} = -\frac{81}{20}\sqrt{\frac{3\pi}{22}}\eta\frac{\delta M}{M}(M\Omega)^{11/3}\left[(1-2\eta)+\left(-\frac{69}{13}-\frac{8\eta}{39}(11\eta-58)\right)(M\Omega)^{2/3}\right], \tag{A4c}$$

$$Mr\,\psi_{5\,,2}e^{i\tilde{\phi}} = \frac{64}{135}\sqrt{\frac{\pi}{11}}\eta\left(1-5\eta+5\eta^2\right)(M\Omega)^4, \tag{A4d}$$

$$Mr\,\psi_{5\,,1}e^{i\tilde{\phi}} = -\frac{1}{180}\sqrt{\frac{\pi}{77}}\eta\frac{\delta M}{M}(M\Omega)^{11/3}\left[(1-2\eta)+\left(-\frac{179}{39}-\frac{4}{39}\eta(\eta-88)\right)(M\Omega)^{2/3}\right], \tag{A4e}$$

For $l=6$:

$$Mr\,\psi_{6\,,6}e^{i\tilde{\phi}} = \frac{15552}{5}\sqrt{\frac{\pi}{715}}\eta\left(1-5\eta+5\eta^2\right)(M\Omega)^4, \tag{A5a}$$

$$Mr\,\psi_{6\,,5}e^{i\tilde{\phi}} = -\frac{15625}{63}\sqrt{\frac{5\pi}{429}}\eta(1-\eta)(1-3\eta)\frac{\delta M}{M}(M\Omega)^{13/3}, \tag{A5b}$$

$$Mr\,\psi_{6\,,4}e^{i\tilde{\phi}} = \frac{16384}{495}\sqrt{\frac{2\pi}{195}}\eta\left(1-5\eta+5\eta^2\right)(M\Omega)^4, \tag{A5c}$$

$$Mr\,\psi_{6\,,3}e^{i\tilde{\phi}} = -\frac{729}{385}\sqrt{\frac{\pi}{13}}\eta(1-\eta)(1-3\eta)\frac{\delta M}{M}(M\Omega)^{13/3}, \tag{A5d}$$

$$Mr\,\psi_{6\,,2}e^{i\tilde{\phi}} = \frac{64}{1485}\sqrt{\frac{\pi}{13}}\eta\left(1-5\eta+5\eta^2\right)(M\Omega)^4, \tag{A5e}$$

$$Mr\,\psi_{6\,,1}e^{i\tilde{\phi}} = -\frac{1}{2079}\sqrt{\frac{2\pi}{65}}\eta(1-\eta)(1-3\eta)\frac{\delta M}{M}(M\Omega)^{13/3}, \tag{A5f}$$

For $l=7$:

$$Mr\,\psi_{7\,,7}e^{i\tilde{\phi}} = -\frac{823543}{180}\sqrt{\frac{7\pi}{4290}}\eta(1-\eta)(1-3\eta)\frac{\delta M}{M}(M\Omega)^{13/3}, \tag{A6a}$$

$$Mr\,\psi_{7\,,5}e^{i\tilde{\phi}} = -\frac{78125}{3276}\sqrt{\frac{5\pi}{66}}\eta(1-\eta)(1-3\eta)\frac{\delta M}{M}(M\Omega)^{13/3}, \tag{A6b}$$

$$Mr\,\psi_{7\,,3}e^{i\tilde{\phi}} = -\frac{2187}{20020}\sqrt{\frac{3\pi}{10}}\eta(1-\eta)(1-3\eta)\frac{\delta M}{M}(M\Omega)^{13/3}, \tag{A6c}$$

$$Mr\,\psi_{7\,,1}e^{i\tilde{\phi}} = -\frac{1}{108108}\sqrt{\frac{\pi}{10}}\eta(1-\eta)(1-3\eta)\frac{\delta M}{M}(M\Omega)^{13/3}, \tag{A6d}$$

The angle θ here is defined as $\pi + i$, where i is the inclination angle in Blanchet et al [12]. We recall that

$$e^{i\tilde{\phi}} \equiv e^{im(\int \Omega dt - 2M\Omega \ln \Omega/\Omega_0)} \,, \tag{A7}$$

and therefore the phase $\tilde{\phi}$ is defined up to an additive term mc, with c a constant factor. By fixing the constant to be $c = 3\pi/2$ we recover, in the limit $\eta \to 0$, Poisson's results from perturbation theory.

The spin-weighted spherical harmonic components of $h_+ \,, h_\times$ can be obtained from the corresponding components of Ψ_4, Eqs. (A1a)-(A6d), as

$$(h_+ - i h_\times)_{l\,,m} = -\frac{1}{m^2\Omega^2}\psi_{l\,,m} \,. \tag{A8}$$

The resulting expressions do include the logarithmic corrections to the phase. They are valid up to 2.5PN, with the only exception of the $l = m = 2$ component, which is given in Eq. (3.4).

APPENDIX B: ESTIMATES OF THE POST-PLUNGE ENERGY, ANGULAR MOMENTUM AND LINEAR MOMENTUM

In this Section we give estimates of the energy, angular momentum and linear momentum radiated in the last phases of a binary black hole inspiral.

TABLE IX: Energy, angular momentum and linear momentum emitted after the estimated time of CAH formation, as listed in Table II. The CAH formation time is measured relative to the peak of the $l = m = 2$ waveform: $\Delta t_{\rm CAH} \equiv (t_{\rm peak} - t_{\rm CAH})/M$.

q	run	$\Delta t_{\rm CAH}/M$	$E_{\rm CAH}/M$	$J_{\rm CAH}/M^2$	$E_{\rm CAH}M/J_{\rm CAH}$	$10^4 P_{x\,,\rm CAH}/M$	$10^4 P_{y\,,\rm CAH}/M$	$10^4 P_{\rm CAH}/M$
1.0	D7	19.0	0.0259	0.1261	4.869	0	0	0
1.5	D7	18.2	0.0232	0.1193	5.142	-2.56	-0.28	2.58
2.0	D7	17.9	0.0193	0.1004	5.202	-3.98	-0.15	3.98
2.5	D7	17.1	0.0156	0.0852	5.462	-5.01	-0.20	5.01
3.0	D7	16.6	0.0128	0.0716	5.594	-5.38	-0.53	5.41
3.5	D7	15.7	0.0105	0.0580	5.524	-5.62	-1.34	5.78
4.0	D7	14.3	0.0086	0.0442	5.139	-5.78	-2.30	6.22
2.0	D8	17.7	0.0192	0.1055	5.495	4.15	-0.23	4.16
3.0	D8	15.2	0.0125	0.0493	3.944	0.28	-5.90	5.91

Table IX lists the energy, angular momentum and linear momentum radiated after the time of CAH formation, estimated as the point where the ratio of the radial and tangential puncture velocities $v_r/v_t > 0.3$ (see Section III).

Given the uncertainties in our estimate of the CAH formation we also consider another useful (if somewhat conventional) indicator of the regime of validity of PN expansions: the Innermost Stable Circular Orbit (ISCO). The ISCO is defined by the condition that the energy function of the two-body system $\mathcal{E}$, which is a function of the orbital frequency Ω, has a minimum: $d\mathcal{E}/d\Omega = 0$. Since $\mathcal{E}$ is only known as a PN series in Ω, the location of the ISCO depends on the PN order [29].

TABLE X: ISCO data using the 2PN Taylor expansion of the energy. The ISCO time is measured relative to the peak of the $l = m = 2$ waveform: $\Delta t_{\rm ISCO} \equiv (t_{\rm peak} - t_{\rm ISCO})/M$.

q	run	$M\Omega_{\rm ISCO}$	$\Delta t_{\rm ISCO}/M$	$E_{\rm ISCO}/M$	$J_{\rm ISCO}/M^2$	$E_{\rm ISCO}M/J_{\rm ISCO}$	$10^4 P_{x\,,\rm ISCO}/M$	$10^4 P_{y\,,\rm ISCO}/M$	$10^4 P_{\rm ISCO}/M$
1.0	D7	0.137	19.6	0.0256	0.1243	0.206	0	0	0
1.5	D7	0.136	19.2	0.0232	0.1181	0.196	-2.29	-0.40	2.32
2.0	D7	0.136	18.6	0.0192	0.0994	0.193	-3.79	-0.07	3.79
2.5	D7	0.134	18.2	0.0156	0.0853	0.183	-4.53	-0.33	4.54
3.0	D7	0.134	17.9	0.0129	0.0727	0.177	-4.83	-0.60	4.86
3.5	D7	0.133	17.9	0.0108	0.0619	0.174	-4.73	-1.24	4.89
4.0	D7	0.132	17.6	0.0092	0.0524	0.176	-4.48	-1.75	4.81
2.0	D8	0.136	18.8	0.0197	0.1068	0.184	-3.65	-0.00	3.65
3.0	D8	0.134	17.9	0.0130	0.0551	0.236	-4.63	-0.40	4.65

In Tables X and XI we list the orbital frequency at the ISCO $M\Omega_{\rm ISCO}$ computed by including terms in the energy function up to 2PN and 3PN, respectively. Notice that 3PN corrections *lower* the ISCO frequency for all mass ratios,

TABLE XI: ISCO data using the 3PN Taylor expansion of the energy. The ISCO time is measured relative to the peak of the $l = m = 2$ waveform: $\Delta t_{\rm ISCO} \equiv (t_{\rm peak} - t_{\rm ISCO})/M$.

q	run	$M\Omega_{\rm ISCO}$	$\Delta t_{\rm ISCO}/M$	$E_{\rm ISCO}/M$	$J_{\rm ISCO}/M^2$	$E_{\rm ISCO}M/J_{\rm ISCO}$	$10^4 P_{x\,,\rm ISCO}/M$	$10^4 P_{y\,,\rm ISCO}/M$	$10^4 P_{\rm ISCO}/M$
1.0	D7	0.129	22.1	0.0266	0.1231	0.216	0	0	0
1.5	D7	0.126	22.8	0.0245	0.1165	0.210	-1.74	-1.08	2.05
2.0	D7	0.120	23.8	0.0208	0.0985	0.211	-2.86	-1.37	3.17
2.5	D7	0.116	24.9	0.0172	0.0850	0.202	-3.11	-1.97	3.68
3.0	D7	0.112	26.5	0.0146	0.0737	0.198	-3.05	-2.46	3.92
3.5	D7	0.109	27.5	0.0123	0.0645	0.191	-2.70	-2.78	3.88
4.0	D7	0.107	28.1	0.0106	0.0568	0.187	-2.28	-3.07	3.82
2.0	D8	0.120	23.6	0.0210	0.0940	0.223	+2.75	+1.26	3.02
3.0	D8	0.112	25.8	0.0146	0.0872	0.167	-3.10	-1.86	3.62

the reduction being larger for larger mass ratios[11]. We also list the time location of the ISCO (relative to the peak in the amplitude of the $l = m = 2$ mode). We identified this time location as the instant when the ISCO frequency equals the orbital frequency from our simulations, as estimated from the gravitational wave emission of the dominant multipolar component $l = m = 2$ (see Section III B): $M\Omega_{\rm ISCO} = M\omega_{D2}$. The 3PN ISCO "absolute" location in terms of the total simulation time is also shown in Table II, and it should be compared with the CAH formation estimates in the same Table. As $q \to 1$ the CAH formation time is very close to the 3PN ISCO time. For large mass ratios, when one of the holes is very small, the difference is larger, as expected on physical grounds.

Tables X and XI also list the energy, angular momentum and linear momentum emitted after the ISCO, with the ISCO location estimated by PN methods. While the energy emitted is a robust quantity, with very weak dependence on the PN order, angular and linear momenta are very sensitive to a variation of the PN order from 2PN to 3PN (i.e., they are very sensitive to small variations in the starting time of the integration). The reason for this behavior is apparent from an inspection of Figs. 13 and 15. While the energy flux is a smooth function, even in the strong-field region, the angular momentum flux is a strongly oscillating function of time.

The functional dependence of energy and angular momentum on mass ratio q can be inferred by combining the multipolar decomposition of the PN expansion (Appendix A) with Eq. (3.24). We find that good fits to the total angular momentum, energy, and multipolar energy distribution in the dominant modes for times $t_0 > t^{\rm 3PN}_{\rm ISCO}$ are:

$$J_{\rm ISCO}/M^2\big|_{t>t_0} = j_{\rm tot}\frac{q^2}{(1+q)^4}\,, \tag{B1}$$

$$E_{\rm ISCO}/M|_{t>t_0} = \epsilon_{\rm tot}\frac{q^2}{(1+q)^4}\,, \qquad E_{\rm ISCO\,,2}/M|_{t>t_0} = \epsilon_2\frac{q^2}{(1+q)^4}\,, \qquad E_{\rm ISCO\,,3}/M|_{t>t_0} = \epsilon_3\frac{q^2(q-1)^2}{(1+q)^6}\,. \tag{B2}$$

with the fitting coefficients listed in Table XII.

TABLE XII: Fitting coefficients for the energy and angular momentum emitted after the ISCO and EMOP times.

t_0	$j_{\rm tot}$	$\epsilon_{\rm tot}$	ϵ_2	ϵ_3
3PN ISCO	2.029	0.421	0.397	0.168
EMOP	1.173	0.295	0.271	0.104

In the same Table, for comparison, we also list the corresponding coefficients for $t_0 > t_{\rm EMOP}$. The ringdown and plunge phase are strongly related with each other, and the numbers are roughly proportional. According to the EMOP criterion ringdown always starts after the ISCO. Therefore the post-EMOP radiation of energy, angular and linear momentum is always smaller than the corresponding radiation after the ISCO.

The PN expansion breaks down after the ISCO. An estimate of the linear momentum emitted *after* the ISCO, within PN theory, was obtained in [18] by integrating the PN linear momentum flux along a plunge geodesic of the

[11] For comparison, the ISCO for point particles is at $r_0 = 6M$, or equivalently at an orbital frequency of $M\Omega = 6^{-3/2} \simeq 0.068$. Corrections to this point particle limit were worked out by Clark and Eardley [43], yielding a simple analytical estimate for large but finite mass ratios: $r_0/M = 6q/(1+q)\,, M\Omega = r_0^{-3/2}$. For $q = 4$ this yields $M\Omega \simeq 0.095$, not too far from the 3PN estimate of 0.107.

Schwarzschild metric. In [18], the integration is performed all the way from the ISCO ($r \simeq 6M$) to the Schwarzschild horizon ($r \simeq 2M$). The energy and angular momentum radiated after the ISCO can be computed using the same method, and they were kindly provided to us by Clifford Will [44].

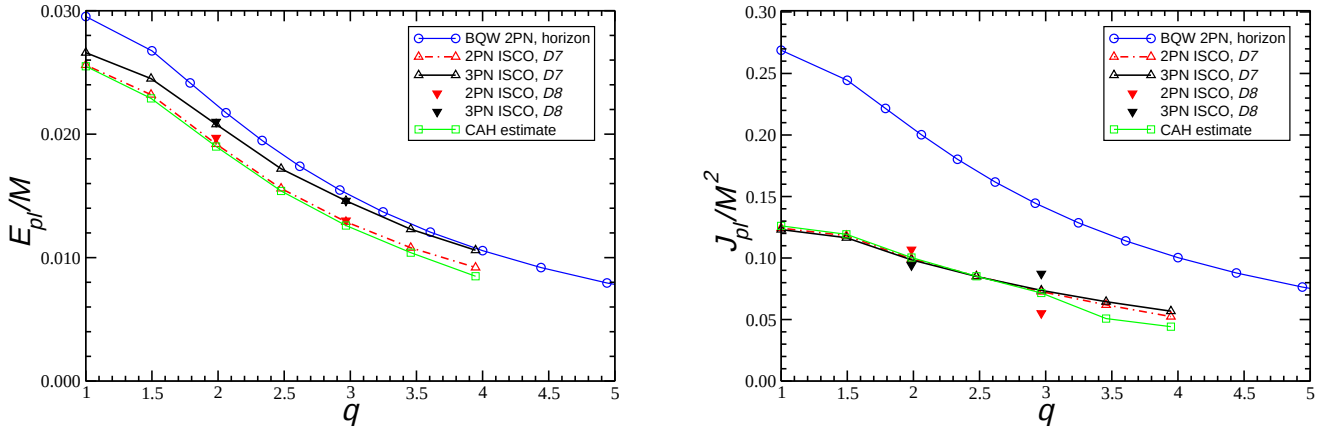

FIG. 24: Energy and angular momentum radiated in the plunge using the 2PN and 3PN definitions of the ISCO are compared against the simple estimate by Blanchet *et al.* [18] (BQW in the legend). All estimates were computed using the D7 runs (except for the inverse triangles, which refer to D8 runs).

Results of a 2PN estimate of the energy and angular momentum radiated after the ISCO are shown in Fig. 24 for different mass ratios, along with different estimates of the corresponding quantities from our numerical simulations. In particular, we show numerical estimates of the energy and angular momentum radiated after the 2PN and 3PN ISCO, and after the CAH formation, as functions of the mass ratio. To check the robustness of our results against initial conditions we also considered two runs starting at larger initial separations (namely, D8 simulations with $q = 2.0$ and $q = 3.0$).

Some comments are in order. The radiated *energy* from the simple PN estimate is in surprisingly good agreement with numerical results, the agreement getting better as we increase the PN order used to estimate the ISCO location. The agreement is particularly good when we consider radiation emitted after the 3PN estimate of the ISCO and relatively large mass ratios. The agreement in the radiated angular momenta is much worse. This seems to be a general feature when comparing PN estimates against numerical simulations. For example, Fig. 2 and 3 in [24] show that the eccentricity required to match PN predictions for a binary's angular momentum against numerical calculations in quasiequilibrium is significantly larger than the eccentricity required to match the corresponding energies. In the present case, the disagreement is partially affected by the strongly oscillating functional dependence of the angular momentum flux (see eg. Fig. 15). This is confirmed by the fact that a relatively small change in the initial separation (using D8 runs instead of D7 runs) produces a significant change in the numerical estimate of the angular momentum radiated after plunge. Given the large uncertainties associated with both numerical and analytical estimates, we cannot draw reliable conclusions from the observed disagreement.

It may be tempting to attribute the observed differences in the angular momentum to the fact that the PN estimates of [18] neglect the ringdown phase. We can naively try to correct for this effect by integrating the energy and angular momentum fluxes from the ISCO *up to the CAH only*. However, this will result in serious disagreement for both the energy and angular momentum radiated: they turn out to be extremely small, especially for mass ratio $q \to 1$ (in this limit the CAH formation time and the ISCO are very close, see Table II). Thus, ringdown alone cannot explain the disagreement. A more detailed analysis, possibly combining the PN approach and the close-limit approximation, is necessary.

An interesting possibility is that the agreement between PN estimates and numerical results could improve if the PN integration is truncated at the *light ring*, instead of integrating all the way to the horizon (as originally done in [18]). The physical argument for truncating at the light ring is that most of the radiation emitted after $r \simeq 3M$ would be filtered by the potential barrier surrounding the black hole, and that this potential barrier (for Schwarzschild black holes) has a peak at the light ring [20]. Fig. 25 shows that truncating at the light ring sensibly improves the estimate of the *linear momentum* radiated after plunge, correspondingly improving the estimate of the total kick velocity. Given

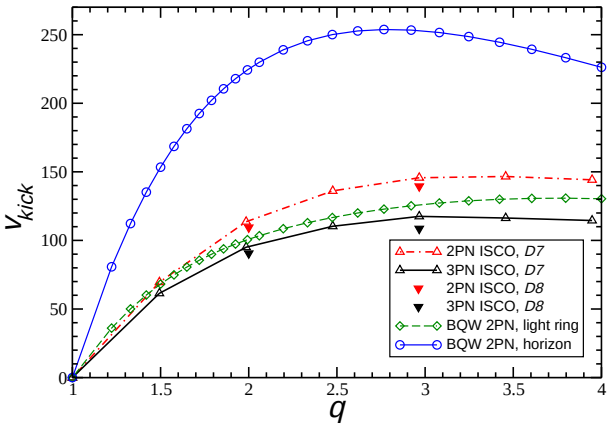

FIG. 25: The kick velocity accumulated after plunge using the 2PN and 3PN definitions of the ISCO is compared against the corresponding estimates by Blanchet *et al.* [18] (BQW in the legend). In the two PN estimates the integration is truncated at the horizon or at the light ring, respectively.

the uncertainties involved in the extrapolation, this may be little more than a coincidence. In any case this problem is worth investigation, given the potential astrophysical relevance of recoil velocities.

APPENDIX C: MULTIPOLAR DISTRIBUTION OF RADIATION FOR EXTREME MASS RATIOS

This Appendix contains a survey of the main results for the energy, angular momentum and linear momentum radiated by particles falling into (rotating or non-rotating) black holes. The purpose of this Appendix is to provide a quick reference for the extreme-mass ratio limit of numerical relativity simulations, to be compared with the present (and future) numerical relativity calculations of binaries with arbitrary mass ratio and spin.

1. The energy radiated by plunging particles: non-rotating black holes

The first investigations of particles plunging into black holes began with Zerilli [45], who laid down the perturbation formalism to analyze gravitational radiation from a point-like particle with mass m_p around a Schwarzschild black hole with mass $M \gg m_p$. His analysis was completed by Davis, Ruffini, Press and Price [46] (hereafter referred to as DRPP), who numerically computed the gravitational radiation generated when a small particle at rest falls from infinity into a Schwarzschild black hole. DRPP found that the total energy emitted in the process (in geometrized units) is given by

$$\Delta E_{\rm tot} = 0.0104 \frac{m_p^2}{M} \,. \tag{C1}$$

Detweiler and Szedenits [47] and Oohara and Nakamura [48] generalized DRPP's results to particles plunging into a Schwarzschild black hole with non-zero orbital angular momentum. In the perturbation framework under consideration, the particle's trajectory as it plunges down the hole, with zero velocity at infinity, is described by

$$\theta \;=\; \pi/2 \,, \quad \frac{dt}{d\tau} = \frac{1}{1-2M/r} \,, \quad \frac{d\phi}{d\tau} = \frac{L_z}{r^2} \,, \tag{C2}$$

$$\frac{dr}{d\tau} \;=\; \pm\Big[1-(1-2M/r)\left(1+\frac{L_z^2}{r^2}\right)\Big]^{1/2} \,. \tag{C3}$$

The particle has an orbital angular momentum $J_p = m_p L_z$. When $L_z = 0$ the particle falls straight into the black hole. For L_z between zero and $4M$, the particle spirals a finite number of times around the hole before crossing the

event horizon. For $L_z = 4M$, the particle spirals an infinite number of times around the marginally bound circular orbit at $r = 4M$. For $L_z > 4M$ the particle never enters the black hole, so we discard this case.

TABLE XIII: Energy radiated in each of the three lowest multipoles for a particle with mass m_p, with angular momentum $m_p L_z$ falling from infinity into a Schwarzschild black hole (from [48]). We show the percentage radiated in each mode relative to the total energy radiated (as extrapolated from the data, which typically yields an error of less than 5%). We also show the number $N = |\Delta\phi|/(2\pi)$ of "laps" the particle performs before plunging. The coefficients a and b are defined in the text. The numbers in this Table can be compared with the numerical values in [46] for $L_z = 0$ and non-rotating black holes: $\Delta E_2 = 9.09 \times 10^{-3} m_p^2/M\,, \Delta E_3 = 1.09 \times 10^{-3} m_p^2/M\,, \Delta E_4 = 1.48 \times 10^{-4} m_p^2/M$.

L_z/M	a	b	N	$\Delta E_{\rm tot}$	ΔE_2	%	ΔE_3	%	ΔE_4	%
0	0.44	2	0	0.010	9.1×10^{-3}	88	1.1×10^{-3}	10	1.5×10^{-4}	1.4
1	0.21	1.5	0.15	0.013	1×10^{-2}	78	2.3×10^{-3}	18	5×10^{-4}	4
2	0.22	1.1	0.32	0.036	2.4×10^{-2}	67	8.1×10^{-3}	22	2.7×10^{-3}	7.5
3	0.36	0.86	0.55	0.112	6.4×10^{-2}	57	2.7×10^{-2}	24	1.2×10^{-2}	10.7
3.5	0.53	0.76	0.75	0.218	1.2×10^{-1}	55	5.4×10^{-2}	25	2.5×10^{-2}	11.5
3.9	1.0	0.71	1.15	0.485	2.4×10^{-1}	49	1.2×10^{-1}	25	5.8×10^{-2}	11.9

In Table XIII we show results from [48] for the total energy radiated in the first three multipoles ($l = 2,\ 3,\ 4$) as a function of L_z. From the Table it is apparent that the total energy output grows with L_z, and so does the energy in each multipole l. The *relative* energy output in each mode behaves somewhat differently: as L_z grows, the percentile energy going into $l = 2$ decreases. The opposite happens for all other modes.

For $L_z = 4M$ the total energy is obviously infinite: the particle spirals an infinite number of times around $r = 4M$ and therefore radiates for an infinite time. The energy radiated as a function of l is well approximated by a simple function: $\Delta E_l \sim a e^{-bl} m_p^2/M$, where the coefficients $a,\ b$ (which are functions of L_z) are listed in Table XIII. The total energy radiated is well approximated by $\Delta E_{\rm tot} \sim a e^{-2b}(1 - e^{-b})^{-1} m_p^2/M$ [48]. Remarkably, the relative contribution of the $l = 3$ mode is always larger than 10%, and that of the $l = 4$ mode is always larger than 1%. As usual the $l = 2$ mode dominates, with a relative contribution always larger than $\sim 50\%$.

Also shown in Table XIII is the number of spirals the particle completes before entering the horizon. This number is useful for two reasons. The first reason is that, if the particle falls with angular momentum very close to the marginal value $4M$, it will complete many revolutions and radiate a huge amount of radiation. In this case the perturbation expansion would no longer be valid, and therefore we must make sure that N is not much larger than one. The second reason is that N gives us an estimate of how much of the output energy is due to the actual, almost radial plunge motion (see eg. Fig. 5), and how much of it comes from the particle circling around the black hole.

2. The energy radiated by plunging particles: rotating black holes

The standard formalism for small perturbations of Kerr black holes was formulated by Teukolsky [49]. The equations decouple and separate, reducing to two coupled ordinary differential equations with a source term. In the case of gravitational waves emitted by particles plunging into the hole the source term diverges at the boundaries, so this is not the most convenient formalism (but see [47] for a way to get around these difficulties). Using the alternative formalism developed by Sasaki and Nakamura [50], a series of papers by Nakamura and co-workers (see eg. [48, 51, 52, 53] and references therein) examined the gravitational radiation emitted by point particles moving in the vicinities of a Kerr black hole.

TABLE XIV: Energy radiated in each of the three lowest multipoles for a particle with zero angular momentum falling from infinity into a Kerr black hole, as a function of $j \equiv J/M^2$. Taken from Fig. 3 in [52].

j	$\Delta E_{\rm tot}$	ΔE_2	%	ΔE_3	%	ΔE_4	%
0.0	1.0×10^{-2}	9.1×10^{-3}	88	1.1×10^{-3}	10	1.5×10^{-4}	1.4
0.7	1.8×10^{-2}	1.5×10^{-2}	83	2.2×10^{-3}	12	3.9×10^{-4}	2.2
0.85	2.3×10^{-2}	1.9×10^{-2}	83	3.4×10^{-3}	15	7.3×10^{-4}	3.2
0.99	4.7×10^{-2}	3.3×10^{-2}	70	9.6×10^{-3}	20	2.7×10^{-3}	5.7

The results for the total energy, as well as the energy radiated in each mode, are summarized in Tables XIV and XV. Starting with particles falling from infinity with zero orbital angular momentum, Table XIV shows a familiar pattern. The total energy increases with increasing j. For near-extremal black holes ($j = 0.99$) the total energy

TABLE XV: Energy radiated in each of the three lowest multipoles for a particle with angular momentum $m_p L_z$ falling from infinity into a Kerr black hole with $j = 0.85$. Taken from Fig. 5 in [51].

L_z/M	$\Delta E_{\rm tot}$	N	ΔE_2	%	ΔE_3	%	ΔE_4	%
2.6	1.2	0.97	5.0×10^{-1}	42	3.0×10^{-1}	25	1.8×10^{-1}	15
1.3	1.0×10^{-1}	0.2	6.5×10^{-2}	61	2.5×10^{-2}	23	9.0×10^{-3}	8.4
0.65	4.8×10^{-2}	0.06	3.5×10^{-2}	73	8.7×10^{-3}	18	2.5×10^{-3}	5.2
0.0	2.3×10^{-2}	0.05	1.9×10^{-2}	81	3.4×10^{-3}	15	7.3×10^{-4}	3.2
-0.8	9.1×10^{-3}	0.17	8.0×10^{-3}	88	9.0×10^{-4}	10	1.3×10^{-4}	1.4
-2.25	1.4×10^{-2}	0.38	1.2×10^{-2}	81	1.8×10^{-3}	12	3.5×10^{-4}	2.3
-4.5	7.7×10^{-2}	1.02	5.5×10^{-2}	71	1.3×10^{-2}	17	5.0×10^{-3}	6.4

radiated is almost five times the Schwarzschild value. Again, the total energy going into each multipole l increases. As previously pointed out, the relative contribution of each mode increases with j for $l > 2$, but it decreases for $l = 2$. The $l = 3$ mode always contributes more than 10% of the total energy, and the $l = 4$ mode always contributes more than 1%.

Table XV shows results for a $j = 0.85$ black hole, for several values of orbital angular momentum L_z. The total energy varies by two orders of magnitude between $L_z = 2.6$ and $L_z = -0.8$. The energy emitted is larger than 10% for $l = 3$, and larger than 1% for $l = 4$. We also list the number of spirals before plunge. This number is always smaller than unity, so the results can in principle be interpreted as a plunging motion and applied to the merger phase.

Not shown here is the contribution of different m's to the total energy. For large black hole rotation and large positive values of L_z most of the energy goes into $l = m$ modes. Negative-m modes emit a negligible amount of radiation in this regime. For negative L_z the situation is different: all modes seem to be excited to comparable amplitudes. See [51] for more details.

3. Linear and angular momentum radiated by plunging particles

Computing the linear momentum carried by gravitational waves is of great astrophysical importance. Coalescing binary black hole systems may abound in galactic disks and in the centers of galactic nuclei. Due to the emission of gravitational radiation the final black hole receives a "kick," i.e., it acquires a non-zero recoil velocity because of momentum conservation. Depending on the momentum emitted, the recoil velocity may be large enough to release black holes from the host galaxy. If so, gravitational radiation effects will have considerable observable consequences for astrophysics and cosmology, such as the depletion of black holes from host galaxies, the disruption of active galactic core energetics, and the ejection of black holes and stellar material into the intergalactic medium. In the following we briefly review some perturbative calculations of the recoil velocity.

a. Linear momentum

In a Schwarzschild background, the linear momentum carried by gravitational waves in the collision of a point particle with zero angular momentum with a black hole is $|\Delta P| = 8.73\times10^{-4} m_p^2/M$ [53]. This leads to a recoil velocity $v \sim 2.63(10 m_p/M)^2$ km/s. For the general case of a particle plunging with non-zero angular momentum L_z, the linear momentum carried by gravitational waves is well approximated by

$$|\Delta P| = 9\times10^{-6}\left(4L_z^2+5L_z+10\right)^2 m_p^2/M\,, \quad 0<L_z<3.4\,, \tag{C4}$$

$$= 4.5\times10^{-2} m_p^2/M\,, \quad 3.4<L_z<4\,. \tag{C5}$$

This leads to a recoil velocity of

$$v \sim 2.7\left(\frac{2}{5}L_z^2+\frac{1}{2}L_z+1\right)^2 (10m_p/M)^2 \text{ km/s}\,, \quad 0<L_z<3.4\,, \tag{C6}$$

$$\sim 130\,(10m_p/M)^2 \text{ km/s}\,, \quad 3.4<L_z<4\,. \tag{C7}$$

These results are not very sensitive to the rotation of the black hole (see eg. Fig. 6 in [51]). A hint to extrapolate these results to mass ratios close to unity comes from the Newtonian result: replace μ/M by $f(q)$, where

$$f(q) = q^2\frac{q-1}{(q+1)^5}\,. \tag{C8}$$

The function $f(q)$ has two extrema at

$$q = \frac{3-\sqrt{5}}{2} \sim 0.38\,, \quad f\left(\frac{3-\sqrt{5}}{2}\right) = -\frac{1}{25\sqrt{5}} \equiv f_{\rm min}(q)\,, \tag{C9}$$

$$q = \left(\frac{3-\sqrt{5}}{2}\right)^{-1} \sim 2.62\,, \quad f\left(\frac{3+\sqrt{5}}{2}\right) = \frac{1}{25\sqrt{5}} \equiv f_{\rm max}(q)\,. \tag{C10}$$

We then get

$$v \sim 4.8\left(\frac{2}{5}L_z^2 + \frac{1}{2}L_z + 1\right)^2 \frac{f(M_1/M_2)}{f_{\rm max}(M_1/M_2)}\ {\rm km/s}\,, \quad 0 < L_z < 3.4\,, \tag{C11}$$

$$\sim 232\frac{f(q)}{f_{\rm max}(q)}\ {\rm km/s}\,, \quad 3.4 < L_z < 4\,. \tag{C12}$$

b. Angular momentum

Radiation of angular momentum demands either a non-zero orbital angular momentum of the particle, or a non-zero angular momentum of the black hole. For Schwarzschild black holes, Oohara and Nakamura [48] found that the ratio $\Delta J/\Delta E_{\rm tot}$ is independent of L_z, even though both of these quantities diverge in the limit $L_z \to 4$. They found

$$|\Delta J| = \frac{\Delta E_{\rm tot}}{0.15}\,, \quad \text{for} \quad |L_z| \gtrsim 1\,. \tag{C13}$$

For rotating black holes, the angular momentum radiated depends on the relative sign between the rotation of the black hole and L_z. We denote by x the ratio of angular momentum to energy radiated:

$$x(j, L_z) = \frac{\Delta J}{\Delta E_{\rm tot}}\,. \tag{C14}$$

This quantity is listed in Table XVI (after Table I in [51]) for some values of L_z and j.

TABLE XVI: The factor $x \equiv \Delta J/\Delta E_{\rm tot}$ for some values of L_z and j (from Table I in [51]).

j=0		j=0.7		j=0.85		j=0.99	
L_z	x	L_z	x	L_z	x	L_z	x
−4	0.15	−4.4	0.03	−4.5	0.04	−4.7	0.07
−3	0.15	−3.3	0.04	−3.375	0.05	−3.5	0.13
−1	0.15	−2.2	0.04	−2.25	0.06	−2.35	0.15
1	0.15	1.5	0.19	1.3	0.21	1	0.30
2	0.15	2.25	0.20	1.95	0.22	1.5	0.30
3	0.15	3.0	0.22	2.6	0.24	2	0.34

4. Perturbation theory as a guide to numerical results for comparable mass ratios

One of the most prominent features borne out of binary black hole simulations seems to be the absence of strong non-linearities: the potential barrier close to the black hole horizon acts as a very effective cloak, filtering out many non-linear features of the dynamics [54]. For this reason results from perturbation theory (i.e., $q \gg 1$) can usually be extrapolated to the equal mass ratio case, yielding very good agreement with full blown numerical simulations. To quote Smarr, "the agreement is so remarkable that something deep must be at work" [55]. This was also found to be the case for the head-on collision of two black holes. The perturbation theory result $\Delta E_{\rm tot} = 0.0104(M_1^2/M_2)$, with $M_1 \ll M_2$ [46] can be compared to the full numerical result for $q = 1$: $\Delta E_{\rm tot} \approx 0.0013M = 0.001 \times 8\eta^2/(M/2) = 0.0104 \times \eta^2/(M/2)$ (see Refs. [54]). Simple scaling arguments applied to perturbative results work surprisingly well.

On this basis, a natural conjecture is that particles plunging with large but sub-critical orbital angular momentum should describe reasonably well the final stages of a binary black hole inspiral [47]. Indeed, some of the results

discussed in the main text suggest that the merger of two equal mass black holes can be described by extrapolating results from perturbation theory. For instance, the final spin of the black hole can be predicted by using the small mass ratio approximation: see Eq. (3.20) and the related discussion.

For inspiralling binaries evolving through quasi-circular orbits, the plunge ("merger") happens when the smaller body crosses the ISCO, even though this notion is not well defined for comparable-mass bodies. We argue that the merger phase should be reasonably well described by a particle plunging with an orbital angular momentum L_z near the marginal value $4M$. In this case the trajectory resembles that of a particle going through the merger phase: a quasi-circular orbit followed by a plunge. It is important to specify how "close" L_z should be to the marginal value. We look for orbits that complete barely less than one lap before plunging. This guarantees that the energy output is due only to a plunge trajectory; it also guarantees that the orbit was quasi-circular before the plunge. We therefore argue that, as seen from the Table, $L_z \simeq 3.9$ is a near-optimal value. An obvious objection is that the ISCO for point particles is not at $4M$, but rather at $6M$. Fortunately, for more massive bodies an approximate ISCO can be defined, and it is usually closer to $4M$. We can thus try to extend these perturbative results to understand the merger phase.

Extrapolating the point particle results presented in the previous subsections we get, for non-rotating holes:

$$\frac{\Delta E}{M} = 0.485\frac{q^2}{(1+q)^4}\,, \qquad \frac{M\Delta E}{\Delta J} = 0.15\,, \qquad v_{\rm recoil} = 232\frac{f(q)}{f(q)_{\rm max}}\,{\rm km}\cdot{\rm s}^{-1}\,. \tag{C15}$$

For instance, the value $0.485q^2/(1+q)^4$ for the energy is found extrapolating the last row in Table XIII by the substitution $m_p^2/M^2 \to q^2/(1+q)^4$. From fits of the corresponding numerical quantities at the 3PN ISCO (which should work as a good reference point, for lack of a better guess) are:

$$\frac{\Delta E_{\rm ISCO}}{M} = 0.421\frac{q^2}{(1+q)^4}\,, \qquad \frac{M\Delta E_{\rm ISCO}}{\Delta J_{\rm ISCO}} = 0.19\,, \qquad v_{\rm recoil}^{\rm ISCO} = 120\frac{f(q)}{f(q)_{\rm max}}\,{\rm km}\cdot{\rm s}^{-1}\,, \tag{C16}$$

The two sets of values are reasonably consistent. The largest disagreement refers to the linear momentum radiated, and therefore to the recoil velocity of the final hole.

APPENDIX D: POLARIZATION OF THE WAVEFORMS

Getting information about the polarization content of a waveform is simple in the presence of a monochromatic wave. In more general settings, making statements about the polarization state is easier in Fourier space. Methods to compute the polarization content of a waveform solely from a time-domain analysis were presented in [56]. Here we shall adapt these techniques for the case at hand.

From the (real) polarization components $h_+(t)\,, h_\times(t)$[12] we can define the so-called *analytic signal* $H_+\,, H_\times$ in the following way:

$$H_+ \equiv h_+(t) + i\mathcal{H}_+(t)\,, \tag{D1}$$
$$H_\times \equiv h_\times(t) + i\mathcal{H}_\times(t)\,. \tag{D2}$$

The imaginary part of the analytic signal is the Hilbert transform $\mathcal{H}(t)$ of the signal $h(t)$, defined as

$$\mathcal{H}(t) = \frac{1}{\pi}\int_{-\infty}^{+\infty}\frac{h(\tau)}{t-\tau}d\tau\,, \tag{D3}$$

where the integral is taken as the Cauchy principal value. For reference we note that the Hilbert transform of $\sin t$ is $-\cos t$ and the transform of $\cos t$ is $\sin t$.

From the analytic signal we define a covariance matrix $\mathbf{C}$ as

$$\mathbf{C} = \begin{pmatrix} H_+H_+^* & H_+H_\times^* \\ H_\times H_+^* & H_\times H_\times^* \end{pmatrix}\,, \tag{D4}$$

[12] In practice we do not use the gravitational wave amplitudes, but the real and imaginary components of Ψ_4, in order to avoid problems with the integration constants and to sidestep the memory effect discussed in Section II A. This should have no influence on the final results.

where an asterisk stands for complex conjugation. We note that the covariance matrix is Hermitian, and thus its eigenvalues $\lambda_0\,,\lambda_1$ are real and positive. Without loss of generality, we assume $\lambda_0 > \lambda_1$. It can be shown that the normalized eigenvector $\mathbf{v} = (x_0\,, y_0)$ ($|\mathbf{v}| = 1$) associated with λ_0 points in the direction of the largest amount of polarization [56]. One can define an elliptical component of polarization P_E as

$$P_E = \frac{\sqrt{1-X^2}}{X}\,, \tag{D5}$$

where

$$X = \max_{\alpha} \sqrt{\mathrm{Re}[e^{i\alpha}x_0]^2 + \mathrm{Re}[e^{i\alpha}y_0]^2}\,. \tag{D6}$$

The quantity $P_E = 1$ for circular polarization, and $P_E = 0$ for linear polarization. For illustration, consider the waveform $h_+ = \sin t\,, h_\times = \cos t$. This is a good approximation to a typical inspiral waveform at large orbital separation, as viewed from the normal to the orbital plane, and it is obviously circularly polarized. For this waveform we have

$$\mathbf{C} = \begin{pmatrix} 1 & -i \\ i & 1 \end{pmatrix}\,, \tag{D7}$$

and $\mathbf{v} = (-i/\sqrt{2}, 1/\sqrt{2})$. This implies $X = 1/\sqrt{2}$ and $P_E = 1$, as expected. For $h_\times = 0$ (linear polarization) we would have $X = 1$ and $P_E = 0$. Thus P_E is a good indicator of the degree of circular or linear polarization. We can also define a polarization strength as follows:

$$P_S = 1 - \frac{\lambda_1}{\lambda_0}\,. \tag{D8}$$

$P_S = 1$ means that the waveform is entirely linearly polarized or circularly polarized (there is only one polarization component), and $P_S = 0$ means that the two polarization states have comparable magnitude.

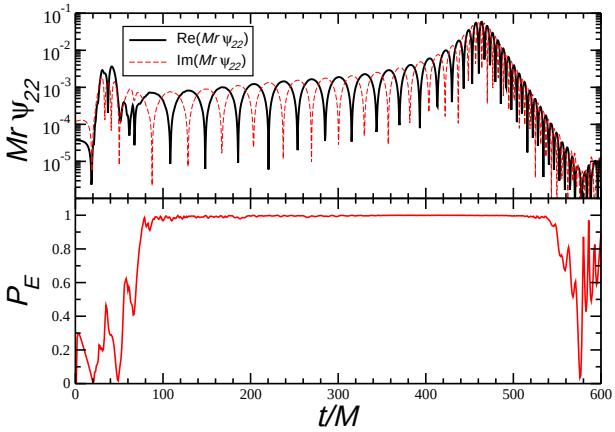

FIG. 26: Top: $|\mathrm{Re}(Mr\,\psi_{22})|$ and $|\mathrm{Im}(Mr\,\psi_{22})|$ for $q = 2.0$, D8 (top). Bottom: the degree of elliptic polarization P_E for the $l = 2$ waveform as viewed from the normal to the orbital plane.

In Fig. 26 we show the result of computing P_E using the dominant ($l = |m| = 2$) component of a binary black hole merger waveform with $q = 2.0$. This plot clearly shows that the polarization is circular for both inspiral and ringdown, with the exception of the unphysical portions of the wave: the initial data burst and the final, noise-dominated part of the ringdown waveform.

[1] A. Buonanno, G. B. Cook and F. Pretorius, arXiv:gr-qc/0610122.
[2] B. Bruegmann, J. A. Gonzalez, M. Hannam, S. Husa, U. Sperhake and W. Tichy, arXiv:gr-qc/0610128.
[3] J. A. Gonzalez, U. Sperhake, B. Bruegmann, M. Hannam and S. Husa, arXiv:gr-qc/0610154.
[4] F. Pretorius, Phys. Rev. Lett. **95**, 121101 (2005) [arXiv:gr-qc/0507014].
[5] J. G. Baker, J. Centrella, D. I. Choi, M. Koppitz and J. van Meter, Phys. Rev. D **73**, 104002 (2006).
[6] M. Campanelli, C. O. Lousto and Y. Zlochower, Phys. Rev. D **73**, 061501 (2006).
[7] F. Herrmann, D. Shoemaker and P. Laguna, arXiv:gr-qc/0601026;
[8] U. Sperhake, arXiv:gr-qc/0606079.
[9] B. Szilagyi, D. Pollney, L. Rezzolla, J. Thornburg and J. Winicour, arXiv:gr-qc/0612150.
[10] H. P. Pfeiffer, D. A. Brown, L. E. Kidder, L. Lindblom, G. Lovelace and M. A. Scheel, arXiv:gr-qc/0702106.
[11] D. Christodoulou, Phys. Rev. Lett. **67**, 1486 (1991); A. G. Wiseman and C. M. Will, Phys. Rev. D **44**, 2945 (1991); K. S. Thorne, Phys. Rev. D **45**, 520 (1992).
[12] L. Blanchet, B. R. Iyer, C. M. Will and A. G. Wiseman, Class. Quant. Grav. **13**, 575 (1996) [arXiv:gr-qc/9602024].
[13] K. G. Arun, L. Blanchet, B. R. Iyer and M. S. S. Qusailah, Phys. Rev. D **66**, 010001 (2002) [Erratum-ibid. **22**, 3115 (2005)].
[14] E. Poisson, Phys. Rev. D **52**, 5719 (1995) [Addendum-ibid. D **55**, 7980 (1997)].
[15] E. Berti, V. Cardoso, J. A. Gonzalez and U. Sperhake, arXiv:gr-qc/0701086.
[16] E. N. Dorband, E. Berti, P. Diener, E. Schnetter and M. Tiglio, Phys. Rev. D **74**, 084028 (2006).
[17] H.-P. Nollert, *Characteristic Oscillations of Black Holes and Neutron Stars: From Mathematical Background to Astrophysical Applications*, unpublished Habilitationsschrift (2000).
[18] L. Blanchet, M. S. S. Qusailah and C. M. Will, Astrophys. J. **635**, 508 (2005).
[19] E. Berti, Class. Quant. Grav. **23**, S785 (2006) [arXiv:astro-ph/0602470].
[20] A. Buonanno and T. Damour, Phys. Rev. D **62**, 064015 (2000).
[21] J. G. Baker, M. Campanelli, C. O. Lousto and R. Takahashi, Phys. Rev. D **65**, 124012 (2002).
[22] M. Koppitz, D. Pollney, C. Reisswig, L. Rezzolla, J. Thornburg, P. Diener and E. Schnetter, arXiv:gr-qc/0701163.
[23] R. J. Gleiser and A. E. Dominguez, Phys. Rev. D **68**, 104018 (2003)
[24] E. Berti, S. Iyer and C. M. Will, Phys. Rev. D **74**, 061503 (2006).
[25] M. A. Miller, Phys. Rev. D **69**, 124013 (2004).
[26] P. C. Peters, Phys. Rev. D **136**, 1224 (1964).
[27] L. Blanchet, T. Damour, G. Esposito-Farese and B. R. Iyer, Phys. Rev. Lett. **93**, 091101 (2004).
[28] E. Poisson, Phys. Rev. D **47**, 1497 (1993); H. Tagoshi and M. Sasaki, Prog. Theor. Phys. **92**, 745 (1994).
[29] A. Buonanno, Y. b. Chen and M. Vallisneri, Phys. Rev. D **67**, 024016 (2003) [Erratum-ibid. D **74**, 029903 (2006)].
[30] D. W. Tufts and R. Kumaresan, Proceedings of the IEEE **70** (9), 975 (1982).
[31] Y. Hua and T. K. Sarkar, IEEE Transaction on Acoustics, Speech and Signal Processing **38** (5), 814 (1990).
[32] K. Levenberg, Quart. Appl. Math. **2**, 164 (1944); D. Marquardt, SIAM J. Appl. Math. **11**, 431 (1963).
[33] E. Berti, V. Cardoso and C. M. Will, Phys. Rev. D **73**, 064030 (2006).
[34] P. Papadopoulos, Phys. Rev. D **65**, 084016 (2002) [arXiv:gr-qc/0104024].
[35] Y. Zlochower, R. Gomez, S. Husa, L. Lehner and J. Winicour, Phys. Rev. D **68**, 084014 (2003).
[36] E. Berti and V. Cardoso, Phys. Rev. D **74**, 104020 (2006).
[37] R. H. Price, Phys. Rev. D **5**, 2419 (1972).
[38] J. G. Baker and M. Campanelli, Phys. Rev. D **62**, 127501 (2000).
[39] E. E. Flanagan and S. A. Hughes, Phys. Rev. D **57**, 4535 (1998).
[40] N. Dorband and M. Tiglio, private communication.
[41] T. Baumgarte, P. Brady, J. D. E. Creighton, L. Lehner, F. Pretorius and R. DeVoe, arXiv:gr-qc/0612100.
[42] K. A. Arnaud *et al.*, arXiv:gr-qc/0701139; K. A. Arnaud *et al.*, arXiv:gr-qc/0701170.
[43] J. P. A. Clark and D. M. Eardley, Astrophys. J. **215**, 311 (1977).
[44] C. M. Will, private communication.
[45] F. J. Zerilli, Phys. Rev. Lett. **24**, 737 (1970); idem, Phys. Rev. D **2**, 2141 (1970).
[46] M. Davis, R. Ruffini, W. H. Press and R. H. Price, Phys. Rev. Lett. **27**, 1466 (1971).
[47] S. L. Detweiler and E. Szedenits, Astrophys. J. **231**, 211 (1979).
[48] K. Oohara and T. Nakamura, Prog. Theor. Phys. **70**, 757 (1983); idem, Phys. Lett. A **94**, 349 (1983).
[49] S. A. Teukolsky, Astrophys. J. **185**, 635 (1973); idem, Phys. Rev. Lett **29**, 1114 (1972).
[50] M. Sasaki and T. Nakamura, Phys. Lett. A **89**, 68 (1982); M. Sasaki and T. Nakamura, Prog. Theor. Phys. **67**, 1788 (1982).
[51] Y. Kojima and T. Nakamura, Prog. Theor. Phys. **71**, 79 (1984).
[52] Y. Kojima and T. Nakamura, Phys. Lett. **A96**, 335 (1983).
[53] T. Nakamura and M. P. Haugan, Astrophys. J. **269**, 292 (1983).
[54] P. Anninos, R. H. Price, J. Pullin, E. Seidel and W-M. Suen, Phys. Rev. D **52**, 4462 (1995).
[55] L. Smarr, Phys. Rev. D **15**, 2069 (1977).
[56] J. E. Vidale, Bull. Seismol. Soc. Am. **76**, 1393 (1986).